

Iron Oxide Based Sensor Development for Gas Sensing

THESIS

Submitted in partial fulfilment
of the requirements for the degree of
DOCTOR OF PHILOSOPHY

by

PODILI SIVASANKARAI AH

ID. No. 2018PHXF0512H

Under the Supervision of

Prof. V. Satya Narayana Murthy

&

Under the Co-supervision of

Dr. P. Nagaraju



BITS Pilani
Pilani | Dubai | Goa | Hyderabad

BIRLA INSTITUTE OF TECHNOLOGY AND SCIENCE, PILANI

2023

BIRLA INSTITUTE OF TECHNOLOGY AND SCIENCE, PILANI

CERTIFICATE

This is to certify that the thesis entitled Iron Oxide Based Sensor Development for Gas Sensing _____ and submitted by Podili Sivasankaraiah ID No 2018PHXF0512H for award of Ph.D. of the Institute embodies original work done by him/her under my supervision.

Signature of the Supervisor:

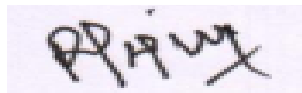


Name in capital letters: Prof. V. SATYA NARAYANA MURTHY

Designation: Professor

Date: 17-02-2024

Signature of the Co-supervisor:



Name in capital letters: Dr. P. NAGARAJU

Designation: Associate Professor

Date: 17-02-2024

Acknowledgments

I remember everyone who helped to successfully complete this work with the utmost gratitude.

First and foremost, adorations and thanks to the God, the Almighty, for His showers of blessings throughout my research work to complete the research successfully.

It gives me great pleasure to thank my research supervisor, Prof. V. Satyanarayana Murthy, for his unwavering support, inspired advice, and persistent encouragement. His advice was really helpful to me while I conducted my research and wrote my thesis.

My profound gratitude goes to my research co-supervisor, Dr. P. Nagaraju Department of Physics, Sreenidhi Institute of Science and Technology, Hyderabad, for all of his help and support as well as for teaching me the ropes. His astute approach, intense curiosity, and encouragement enabled me to finish my research. I have been greatly inspired by his dynamism, vision, genuineness, and motivation. To have worked and studied under his direction was an enormous honor and privilege. I am extremely grateful to him for his friendship, empathy, valuable suggestions and the trust in me.

I owe a debt of gratitude to Professors Dr. P. K. Thiruvikraman, Dr. Kannan Ramaswamy, Dr. K V S Shiva Chaitanya, and Dr. B Harihara Venkataraman Department of Physics, BITS Hyderabad for their excellent advice and insightful ideas during my doctoral studies.

I am very grateful to Sri Ch. Gopal Reddy, Chairman, and Dr. A. Raji Reddy, Director, of the CMR Technical Campus, for allowing me to use the department's resources and facilities. I would like to use this occasion to express my gratitude to Dr. K. Venkateswar Reddy, Head of the Department of H&S, and Dr. A. Srinivasulu Reddy, Principal of CMR Engineering College, for their unwavering encouragement and support throughout my research term.

I wish to express my sincere thanks to Dr. Y. Vijayakumar, Department of Physics, Anurag University, Hyderabad and Dr. D. Gavaskar for their kind help in my research work. I express my profound thanks to Dr. V.R. Reddy, Scientist-F, UGC-DAE, Indore for providing AFM, GIXRD, Raman studies respectively.

I will always be grateful to my fellow scholars, Mr. K. Sathish and Dr. Yuganand, for the enjoyable days we spent together at this department.

I am grateful to all of my teachers from my undergraduate, graduate, and post-graduate years for their support and inspiration in all of my undertakings. I am grateful for the genuine assistance that N. Srinivasula Reddy provided me with while I pursued my higher studies. I would like to mention a number of other research scholars from this university, whose friendship I hope to keep forever and who have always been there to assist me on my journey.

I wish to extend my warmest thanks to my mother P. Ramanamma and brothers Dr. P. Koteswaraiah, Mr. P. Sivarathnam and sister-in-law P. Swaroopa Rani for their unconditional help during my education tenure and during this work.

I can never express how grateful I am to my wife P. Swathi and my two boys, Maha Gnana Thejeswar and Kesava Sai Bhavesh, for their unwavering love and support during my research study.

Lastly, I would want to express my gratitude to everyone who helped me, whether directly or indirectly, to finish my research work.

P. Sivasankaraiah

ABSTRACT

Iron oxides are widely used gas-sensing materials to detect toxic gases. It has grabbed much attention across the globe due to cost-effectiveness in production, simplicity and sensitivity towards different gases. In the current study, I have deposited pure α -Fe₂O₃ thin films using a low-cost, chemical spray pyrolysis technique at various deposition temperatures ranging from 375°C to 425 °C with other optimized deposition conditions. The effect of deposition temperature on morphological, micro structural, optical, and gas-sensing properties are investigated systematically. With increasing substrate temperature, the crystallite size of the films is observed to be decreasing, and the optical band gap increases from 2.8 to 2.88 eV. From the FESEM investigations, the film deposited at 375 °C exhibits the formation of cuboid-shaped nanocrystals with dense surfaces and uniform grain distribution. The AFM studies show that the films have demonstrated smooth surfaces as the substrate temperature increases. At room temperature, gas-sensing properties of iron oxide films have been performed using a static method towards various gases with different concentrations. Response and recovery times of the iron oxide thin films are determined using the transient response curve. The film deposited at a substrate temperature of 375 °C has shown the best sensitivity towards 5 ppm of ammonia with a response and recovery times of 40 s and 56 s, respectively. After optimizing deposition temperature, Al-doped α -Fe₂O₃ thin films were prepared by employing chemical spray pyrolysis with different aluminium concentrations. Subsequently, the films were annealed at 450 °C and the effect of annealing temperature on structural, morphological, optical, chemical and gas sensing properties were investigated. Field emission scanning electron microscopy and X-ray diffraction studies were adapted to examine the morphologies and micro structural properties of the α -Fe₂O₃ based thin films. All the films were polycrystalline in nature with rhombohedral structure, and the (104) plane was confirmed to be the favoured orientation. Deposited thin films were seen to have agglomerated, superimposed sphere-like particles on their surfaces in AFM and FESEM micrographs. Raman spectroscopy analysis and XPS were used to examine the film's symmetry and structural characteristics. The optical band gap of the deposited thin films was determined using the Tauc plot. Pure and Al-doped iron oxide thin film's formaldehyde sensing capability was examined based on aluminium (Al) doping concentration. The results of the experiments showed that the gas-detecting capabilities have been significantly enhanced by the optimal content of Al added to the α -Fe₂O₃ lattice.

Table of Contents

Certificate	i
Acknowledgment	ii
Abstract	iv
Table of content	v
List of tables	viii
List of figures	ix
List of Abbreviations	xii
Chapter-1 Introduction to gas sensors and Literature survey	1-22
1.0 Introduction	1
1.1 Gas sensors	1
1.2 Requirements of gas sensors	2
1.3 Types of gas sensors	2
1.4 Gas sensing mechanism	4
1.5 Parameters of gas sensors.....	7
1.6 Methods to improve gas sensing response	9
1.7 Applications of gas sensor	12
1.8 Literature survey on Fe ₂ O ₃ gas sensors	12
1.9 Gaps in the existing literature.....	21
1.10 Objectives of the current study	22
1.11 Definition of the problem and outline of the thesis	22
Chapter-2 Experimental and Characterization Techniques	23-53
2.0 Introduction	23
2.1 Experimental Techniques.....	24
2.1.1 Thin film deposition Technique	24

2.1.2	Iron oxide as a sensing material	26
2.1.3	Spray pyrolysis Technique (SPT)	28
2.1.4	Advantage and disadvantages of SPT	31
2.1.5	Substrates	32
2.2	Characterization Techniques	33
2.2.1	X-ray diffraction (XRD)	33
2.2.2	Scanning electron microscopy (SEM)	39
2.2.3	Energy-dispersive analysis by X-rays (EDAX)	41
2.2.4	Raman spectroscopy	42
2.2.5	X-ray photoelectron spectroscopy (XPS)	45
2.2.6	Atomic force microscopy (AFM)	47
2.2.7	Ultraviolet–Visible spectroscopy	48
2.2.8	Thickness measurement	52
2.3	Gas sensing system	53
Chapter-3	Synthesis and Characterization of α-Fe₂O₃ thin films for the detection of ammonia gas	55-71
3.0	Introduction	55
3.1	Experimental Techniques	56
3.1.1	Preparation of α -Fe ₂ O ₃ thin films	56
3.1.2	Thickness measurement	58
3.2	Results and discussion	59
3.2.1	X-ray diffraction	59
3.2.2	Field Emission Scanning Electron Microscopy	60
3.2.3	Energy Dispersive by X-ray spectroscopy	61
3.2.3	Atomic force microscope studies	63
3.2.4	X-ray photoelectron spectroscopy studies	64
3.2.5	Optical studies	66

3.3 Gas sensing characterization	67
3.3.1 Response and recovery characteristics	71
3.4 Summary	71
Chapter-4 Synthesis and Characterization of Al-doped α-Fe₂O₃ thin films for formaldehyde gas sensing application	72-99
4.0 Introduction	72
4.1 Experimental Techniques	73
4.1.1 Synthesis of of pure and Al-doped α -Fe ₂ O ₃ thin films.....	73
4.2 Results and discussion	76
4.2.1 X-ray diffraction	76
4.2.2 Field Emission Scanning Electron Microscopy	79
4.2.3 Energy Dispersive by X-ray spectroscopy	81
4.2.4 Atomic force microscope studies	84
4.2.5 Raman spectroscopic studies	85
4.2.6 X-ray photoelectron spectroscopy studies	86
4.2.7 Optical studies	88
4.3 Gas sensing characterization	91
4.3.1 Response and recovery characteristics	92
4.3.2 Formaldehyde gas sensing mechanism	93
4.4 Summary	98
Chapter-5 Summary and conclusions	100-104
5.1 Summary and conclusion	100
5.2 Scope for future work	103
Bibliography	105-121
Publications	122
Biography of the candidate	123
Biography of the supervisor	124
Biography of the co-supervisor	125

List of Tables

Table 2.1: Methods of thin film deposition	26
Table 3.1. Deposition parameters of α -Fe ₂ O ₃ thin films	57
Table 3.2: Thickness of α -Fe ₂ O ₃ thin films	58
Table 3.3: Structural parameters of α -Fe ₂ O ₃ thin films.....	60
Table 3.4: Elemental analysis of α -Fe ₂ O ₃ thin films.....	62
Table 3.5: Surface features and quality of the iron oxide thin films.....	63
Table 3.6: Optical bandgap of α -Fe ₂ O ₃ thin films	67
Table 4.1: Deposition parameters of Al doped α -Fe ₂ O ₃ thin films.....	74
Table 4.2: Structural characteristics of Al-doped α -Fe ₂ O ₃ thin films annealed at 450°C	79
Table 4.3: Elemental composition of Al-doped α -Fe ₂ O ₃ thin films annealed at 450°C	81
Table 5.1: Summarized results concerning the deposition, characterization results and gas responses of α -Fe ₂ O ₃ films	102
Table 5.2: Summarized results concerning characterization results and gas responses of Al doped α -Fe ₂ O ₃ films deposited at 375°C, annealed at 450°C	103

List of figures

Fig. 1.1: Schematic representation of gas sensing mechanism	6
Fig. 1.2: The relationship between sensitivity and the metal oxide's depletion layer depth	11
Fig. 2.1: α -Fe ₂ O ₃ structure	27
Fig. 2.2: γ -Fe ₂ O ₃ structure	27
Fig. 2.3: Schematic representation of spray pyrolysis deposition apparatus	29
Fig. 2.4: Photograph of Spray pyrolysis system used in present work	30
Fig. 2.5: X-ray diffraction method	35
Fig. 2.6: Photograph of X-ray diffractometer	37
Fig. 2.7: FWHM measured in a typical peak of phase in a material XRD pattern	38
Fig. 2.8: Photograph of SEM and EDAX	41
Fig. 2.9: Schematic illustration of a Raman spectrometer	44
Fig. 2.10: Photograph of a Raman spectrometer	44
Fig. 2.11: Schematic illustration of a X-ray Photoelectron Spectroscopy	45
Fig. 2.12: Photograph of X-ray Photoelectron Spectroscopy	46
Fig. 2.13: Photograph of AFM.	48
Fig. 2.14: Photograph of UV-visible spectrophotometer	51
Fig. 2.15: Photograph of the gas sensing system	54
Fig. 3.1: Images of deposited films at various substrate temperatures on a glass substrate	57
Fig. 3.2: X-ray diffractogram of α -Fe ₂ O ₃ thin films prepared at various deposition temperatures	59
Fig. 3.3: FESEM images of α -Fe ₂ O ₃ films sprayed at different deposition temperatures	61
Fig. 3.4: EDX of α -Fe ₂ O ₃ films sprayed at different deposition temperatures	62
Fig. 3.5: 3-dimensional AFM images of α -Fe ₂ O ₃ thin films deposited at different substrate temperatures	63
Fig. 3.6: XPS spectra of Fe 2p core-shell of α -Fe ₂ O ₃ thin films prepared at different deposition temperatures.....	65
Fig. 3.7: XPS spectra of O1s core-shell of α -Fe ₂ O ₃ thin films deposited at different deposition temperatures.....	65

Fig. 3.8: Tauc plots of α -Fe ₂ O ₃ thin films deposited at different substrate temperatures.....	66
Fig. 3.9: Selectivity of α -Fe ₂ O ₃ films deposited various deposition temperatures towards different gases.	68
Fig. 3.10: Repeatability of α -Fe ₂ O ₃ thin film deposited at 375°C	68
Fig. 3.11: Stability of α -Fe ₂ O ₃ thin film prepared at 375°C	69
Fig. 3.12: Variation of response at different concentrations of ammonia towards α -Fe ₂ O ₃ thin film deposited at 375°C	70
Fig. 3.13: Transient response curve of α -Fe ₂ O ₃ thin film prepared at 375°C	70
Fig. 4.1: Cross section view of Al-doped α -Fe ₂ O ₃ thin films annealed at 450 °C	75
Fig. 4.2: X-ray diffraction profile of Al-doped α -Fe ₂ O ₃ thin films deposited at 375 °C	77
Fig. 4.3: XRD spectra of Al-doped α -Fe ₂ O ₃ thin films annealed at 450°C	78
Fig. 4.4: FE-SEM micrographs of Al-doped α -Fe ₂ O ₃ thin films annealed at 450°C	80
Fig. 4.5: Energy dispersive X-ray spectrum of Al-doped α -Fe ₂ O ₃ thin films annealed at 450°C	82
Fig. 4.6: Energy dispersive X-ray spectrum of Al-doped α -Fe ₂ O ₃ thin films annealed at 450°C	83
Fig. 4.7: AFM 3-D pictures of Al-doped α -Fe ₂ O ₃ thin films annealed at 450°C	84
Fig. 4.8: RMS roughness of pure and Al-doped α -Fe ₂ O ₃ thin films annealed at 450°C	85
Fig. 4.9: Raman spectra of Al-doped α -Fe ₂ O ₃ thin films annealed at 450°C	86
Fig. 4.10: Fe 2p spectra of pure and Al-doped α -Fe ₂ O ₃ thin films annealed at 450°C	87
Fig. 4.11: O1s spectra of pure and Al-doped α -Fe ₂ O ₃ thin films annealed at 450°C	87
Fig. 4.12: Al 2p spectra of pure and Al-doped α -Fe ₂ O ₃ thin films annealed at 450°C	88
Fig. 4.13: Tauc plots for Al-doped α -Fe ₂ O ₃ thin films annealed at 450°C	89
Fig. 4.14: Tauc plots for Al-doped α -Fe ₂ O ₃ thin films annealed at 450°C	90
Fig. 4.15: Sensitivity of Al-doped α -Fe ₂ O ₃ thin films annealed at 450°C towards different gasses of 5ppm concentration tested at room temperature	92
Fig. 4.16: Transient response curve of pure and Al-doped α -Fe ₂ O ₃ thin films annealed at 450°C	94
Fig. 4.17: Transient response curve of pure and Al-doped α -Fe ₂ O ₃ thin films annealed at 450°C	95

Fig. 4.18: Stability of Al-doped α -Fe ₂ O ₃ thin films annealed at 450°C	96
Fig. 4.19: Repeatability of 10 wt% Al-doped α -Fe ₂ O ₃ thin film annealed at 450°C and tested at room temperature towards 5ppm formaldehyde gas	96
Fig. 4.20: Sensitivity variation at different concentrations of formaldehyde towards 10 wt% Al-doped α -Fe ₂ O ₃ thin film annealed at 450°C	97
Fig. 4.21: Formaldehyde sensing mechanism of Al-doped α -Fe ₂ O ₃ sensor	98

List of abbreviations

Abbreviation	Expansion
WHO	World Health Organization
MOGS	Metal oxide gas sensor
LOD	Limit of detection
BET	Brunauer–Emmett–Teller
XRD	X-ray Diffraction
SEM	Scanning Electron Microscopy
TEM	Transmission Electron Microscopy
EDX or EDS	Energy Dispersive X-Ray Spectroscopy
XPS	X-ray photoelectron spectroscopy
UV-Vis	Ultra-Violet-Visible
FWHM	Full Width at Half Maximum
AFM	Atomic force microscope
Al	Aluminium
CNT	Carbon nano tube
SP	Spray Pyrolysis
VOC	Volatile organic compounds
ppm	Parts per million

1.0 Introduction

Automation has become increasingly important in the fields of environmental science, industries, medical science, transportation, education, research, agriculture, etc. with the rapid growth of modern science and technology, leading to a more comfortable standard of living for people. Many of us are unable to identify the type or concentration of gas in our atmosphere even though the human nose possesses 400 types of scent receptors that allow us to detect approximately 1 trillion distinct aromas. Millions of people die each year due to diseases caused by breathing in air pollution, including pneumonia, lung cancer, chronic obstructive pulmonary disorders, stroke, and heart disease [WHO 2022]. Sensors are used in various fields, including manufacturing facilities, industries, and homes, to measure the concentration and quality of the air indoors, locate gas leaks, and detect gases generated during residential operations.

Many hazardous, explosive, poisonous, and flammable gases have been used in many locations at the expense of human health and the environment. As there is a significant risk to human lives and property, monitoring and controlling these gases becomes necessary [1]. Researchers have concentrated harder than ever to develop cheap, quick, and extremely sensitive gas sensors to identify dangerous and flammable chemicals and safeguard human life [2].

1.1 Gas sensors

A sensor is an object that detects input of any type from the physical environment and responds to it. There may be numerous inputs, including warmth, light, movement, humidity, pressure, gas, etc. The output is typically a signal translated into a display that humans can read at the sensor location or electronically sent over a network to be read or put through more processing.

Electronic gadgets that detect and distinguish between several gas types are generally defined as gas sensors or gas detectors. They are frequently used to measure gas concentration and to detect hazardous gases, such as H_2S , NH_3 , HCN , $HCHO$, CO , Cl_2 , F_2 etc. or explosive gases like LPG, Nitroglycerin, Acetone Peroxide, TNT, RDX, etc. In factories and manufacturing facilities, gas sensors can spot leaks and detect smoke and CO in residential buildings. Numerous sizes are available for gas sensors (portable and fixed), sensing capabilities, and ranges. These are typically attached to an audible alarm or interface. These are components of embedded systems, such as HAZMATs (which comprise substances such as poisonous chemicals, fuels, nuclear waste products, biological, chemical, and radioactive agents) and

security systems. Gas sensors require more frequent calibration because they are continually reacting with air and other gases.

1.2 Requirements of gas sensors

The modern era has brought many conveniences into our society, but they also have certain negatives, such as air pollution and the release of harmful gases. Gas sensors are required as a result of the ongoing monitoring and regulation of the gases released. As an example, monitoring air pollution, chemical reactions, and combustion engine exhaust are just a few of the diverse sectors and applications where gas sensors are used.

The sensors can also be used in fuel cells, research facilities, industries, and the aerospace industry, among other things. The usage of various gases as raw materials in many industrial sectors has increased in recent years. Control and monitoring of these gases become extremely crucial because of a leakage possesses a significant risk to human and property safety. Currently, numerous methods of gas monitoring systems have been widely using [3-4]:

- For oxygen (O₂), to observe breathing environments and to regulate combustion.
- To prevent unwelcome fires or explosions occurring when combustible gases are in the air. For most gases, the lower explosive limit is up to a few percent; hence, concentrations must be tested up to that level.
- It's important to monitor concentrations near exposure limits for harmful chemicals in the air.

So, to prevent the hazards listed above, we need gas detectors that can continually and effectively monitor these chemicals.

1.3 Types of gas sensors

Based on the sensing element used in gas sensors, they are classified into various types.

- a) Metal Oxide gas sensor
- b) Optical gas sensor
- c) Electrochemical gas sensor
- d) Capacitance based gas sensor
- e) Calorimetric gas sensor
- f) Acoustic based gas sensor

1.3.1 Metal oxide gas sensor (MOGS)

By monitoring the change in metal oxide resistance brought on by the adsorption of gases, MOGS can measure the concentration of several types of gases. The target gases minimize atmospheric oxygen on the MOGS surface, allowing more electrons to enter the metal oxide material's conduction band.

Gas adsorption is essentially a surface-related process. As a result, the MOGS sensitivity can be changed by varying the grain size and surface area of the sensing material's active surface layers. As a result, gas sensing is significantly impacted by particle size reduction. Because they have a significant specific surface area, metal oxide nanoparticles are excellent materials for creating chemical gas sensors. Compared to materials with coarse micro-grained structures, their surface area to volume ratio is significantly higher.

$$\frac{\text{Surface area}}{\text{Volume}} = \frac{4\pi r^2}{\frac{4}{3}\pi r^3} = \frac{3}{r} \quad (1.1)$$

where r is the radius of the spherical metal oxide nanoparticles,

Hence, the ratio of a nanoparticles surface area to volume will rise when its radius is reduced. As a result, the oxide and gaseous media form a wide interface. Consequently, a sensor made of small nano materials is more sensitive than one made of macro particles for the same chemical composition. Most of the interaction between, a gas and a solid occurs at the surface, and the regulation of the metal oxides' characteristics depends heavily on interfaces.

Many metal oxides such as Cr_2O_3 , Mn_2O_3 , Co_3O_4 , NiO , CuO , SrO , In_2O_3 , WO_3 , TiO_2 , V_2O_5 , Fe_2O_3 , GeO_2 , Nb_2O_5 , MoO_3 , Ta_2O_5 , La_2O_3 , CeO_2 , Nd_2O_3 , ZnO are suitable for detecting combustible, reducing, and oxidizing gases by conductivity measurements [1]. Metal oxide gas sensors have an advantage over polymers and other gas sensors in that their sensitivity is not affected by temperature. Although the polymer has excellent sensitivity, it isn't easy to reverse and requires sophisticated processing [2, 3].

1.3.2 Optical gas sensors

These kinds of sensors pick up optical signals, and their output response varies in direct proportion to the radiation they receive. The phenomena employed for radiant sensors are photoconductivity and photovoltaic effects. The conductivity of a film or pellet changes as specific radiations impact it. The intensity of the radiation is used to calibrate the change in conductance.

1.3.3 Electrochemical gas sensor

Electrochemical sensors interact with the target gas and generate an electrical signal corresponding to the target gas concentration. The sensor, which consists of two electrodes (a working electrode and a counter electrode), works by permitting charged molecules to flow through a thin film of electrolyte.

1.3.4 Capacitance-based gas sensor

A capacitive sensor is an electronic gadget that can detect solid or liquid targets without physical contact. Gas capacitance sensors assess variations in capacitance brought on by changes in the dielectric constant.

1.3.5 Thermal conductivity gas sensor

The thermal conductivity sensor detects variations in the column eluent's thermal conductivity and contrasts them with a reference flow of carrier gas. This thermal conductivity gas analyzer determines the gas concentration by using the difference in thermal conductivities between two gas components.

1.3.6 Acoustic-based gas sensor

The structures of acoustic gas sensor devices include a sensing layer that is intended to adsorb target gas molecules. Their functioning principle is based on fluctuations in the resonant frequency and acoustic wave propagation characteristics imposed by their sensor layer mass. Due to their naturally compact shape, low power requirement, and potential for high sensitivity, micro machined acoustic gas sensors are a suitable technology in chemical sensing applications.

1.4 Gas sensing mechanism

The gas sensing mechanism in metal oxides like TiO_2 , ZnO , WO_3 etc described below:

- a) Diffusion of reactants to the active region
- b) Adsorption of reactants onto the active region
- c) Surface reaction
- d) Desorption of products from the active region
- e) Diffusion of products away from the active region.

Reactant diffusion into the active zone is influenced by the measurements and the environment's ambient temperature. The measured gas molecules stick to the detecting surface once diffusing

into the active layer. This procedure is known as adsorption. There are three types of adsorption: Physisorption, chemisorption and ionosorption.

1.4.1 Physisorption

A weak kind of adsorption known as physisorption is typically characterized by dipole-dipole interaction between the adsorbate and the surface. The geometrical and electrical structures of the particle and the surface remain unchanged in the event of physisorption. A weak interaction (Van der Waals forces) exists between the adsorbate and the surface. At comparatively low temperatures, physical adsorption and desorption take place.

1.4.2 Chemisorption

In contrast to physisorption, which is substantially weaker than chemisorption, It is characterized by a strong contact between adsorbate molecules and the surface. The surface composition is altered because of the intense interaction with the adsorbents during chemisorptions. Chemisorptions can happen at the atomic or molecular level. The latter one moves forward by causing the molecules on the surface to split apart. The oxidation or reduction states of the adsorbate molecules are modified via chemisorptions on semiconductors. As a chemical bond is formed, chemisorptions also alter the electronic structure of the adsorbate and the surface of the electrons are caught in the adsorption complex or transported from the adsorption complexes into the conduction band of semiconductors. Changes in conductivity can be used to measure the equivalent changes in free charge concentration.

1.4.3 Ionosorption

Ionosorption is a specific kind of chemisorption that occurs when the adsorbate works as a surface state to capture an electron or a hole. Ionosorption occurs when an electron is pulled out of the bulk (conduction band) of atoms or molecules during adsorption process. Ionosorption can therefore be thought of as delocalized chemisorption. The charge transfers between molecules and surfaces highly influence the chemical reactivity of the molecules and their electrical and geometrical shapes.

1.4.4 Sensing mechanism in MOGS

According to Kalpana kumara et al.[1] and Andrea Ponzoni et al. [4], oxygen is absorbed on the material's grain surfaces when a gas sensor is exposed to air. Extrinsic surface acceptor states (O_2^- , O^{2-} , and O^-) are produced as a result of the chemisorption of oxygen from the gas phase, immobilizing the conduction band electrons from the metal oxide's near-surface region.

As a result of the adsorbed oxygen from air under ambient circumstances, a depletion layer is produced at the material interface (Fig. 1a). The thickness of the depletion layer (W) is

$$W = \sqrt{\frac{\epsilon_r \epsilon_0 V_s}{qn}} \quad (1)$$

Where

ϵ_r is the relative permittivity of the metal oxide,

ϵ_0 is the permittivity of vacuum,

V_s is the band bending,

q is the electron charge,

n is the charge carrier density

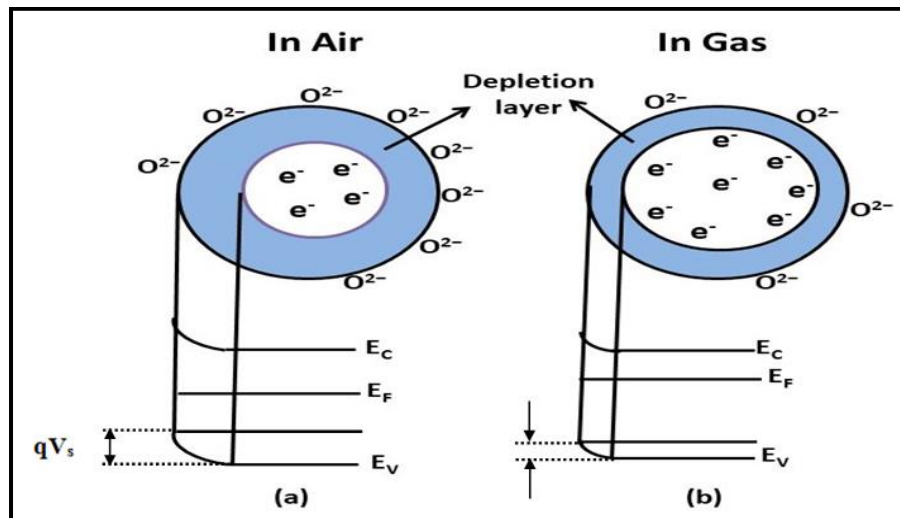


Fig. 1.1: Schematic representation of gas sensing mechanism in metal oxide-based sensors (a) in the presence of atmospheric oxygen and (b) in the presence of reducing gas.

In the presence of reducing or oxidizing gases, the density of charge carriers in the nanostructure's vicinity may alter. The reducing gases will extract the surface-bound oxygen atoms that act as donors for the metal oxide (Fig. 1b). The production of extra surface-acceptor states by oxidizing gases, however, will result in the immobilization of more conduction-band electrons from the vicinity of the surface. The conductivity of a material increases when the gas concentration is reduced; it decreases when the gas concentration is increased. The barrier height (qV_s) created at the grain boundaries for the one-dimensional geometry is determined by the density of surface states (N_s) regulated by oxidation or reduction reactions., as represented in

$$qV_s = \frac{q^2 N_s^2}{2\epsilon_r \epsilon_0 n} \quad (2)$$

The functioning principle of the gas sensor is thus based on how the conductivity changes when the barrier height changes.

1.5 Parameters of gas sensors

The important parameters of a gas sensor are

- Sensitivity
- Selectivity
- Stability
- Response time
- Recovery time
- Detection limit
- Operating temperature

1.5.1 Sensitivity

This feature of the device allows detecting changes in the sensing material's physical and/or chemical properties when exposed to gas. The ratio of the sensing element's resistance in the target gas to its resistance in air is the standard definition of sensitivity. The operating temperature, porosity, thickness, and crystallite size all significantly impact the sensitivity. Working with the greatest sensing material in each circumstance and getting it to the perfect detecting temperature to enhance it will be extremely intriguing. According to several papers [5-7], using nanostructure materials will increase the surface area in front of gas. Adjusting metal oxide particle size will be one of the key requirements for raising the sensor's sensitivity because sensing responses largely take place on the surface of the sensor layer. It is well known that sensitivity S is defined as [2].

$$S = \frac{R_a - R_g}{R_g} \approx \frac{R_a}{R_g} \text{ if } R_a \gg R_g \quad (3)$$

$$S = \frac{R_g - R_a}{R_a} \approx \frac{R_g}{R_a} \text{ if } R_g \gg R_a \quad (4)$$

where, R_a is the resistance in air and R_g is the resistance in the presence of test gas at a given temperature.

1.5.2 Selectivity

This characteristic relates to a sensor's ability to distinguish between gas mixtures. Gas identification heavily relies on selectivity. A "fingerprinting" technique often depends on the target gas signal's distinctive signature. Yet, sensor responses to gases are frequently extremely similar. For instance, the creation of a household gas detector that can distinguish between species is hampered by the substantial cross-sensitivity of gases like ethanol, carbon monoxide, ammonia and methane [8-9]. Increasing the selectivity of gas sensors involves adjusting the working temperature of the sensor, adding additives, and using selective gas filters in series with gas sampling. When each gas has a distinct T_{crit} (critical temperature/optimum temperature with maximal sensor response), different working temperatures enable the modulation of sensitivity towards that gas, enabling the sensor to generate distinct signals for two gases at a chosen temperature. The shape of the film and the sensor design can both greatly impact selectivity [10]. It will be simpler to discriminate between reactive and poorly reactive gases if electrodes are positioned further inside the bulk of the sensing material. This will allow reactive molecules to be filtered by the sensing material close to the sensor's surface. A different technique involves the use of catalysts, which typically lower a gas sensor's operating temperature for a particular gas species and make it possible to differentiate the target gas from other gases due to differences in sensitivity. In other words, inclusion of catalysts can raise the sensitivity of target gases to generate a distinct signal.

1.5.3 Stability

It is a property that considers the repeatability of the device measurements across time. The sensor's success will be constrained if the sensor performance is not shown to be repeatable and stable over extended testing. According to researchers [11-12], stability issues can be related to three main causes.

- The first is that a surface-conductive sensor may become contaminated on its surface.
- Second, mismatched thermal expansion coefficients and/or interfacial interactions at the metal electrode/ceramic interface might cause changes in the sensor's properties (such intergranular connectivity).
- Third, the morphology of the film may alter over time due to the sensor's relatively high working temperatures, which may result in additive migration.

To avoid non-repeatability effects after repeated use, the sensor materials are exposed to a thermal pre-treatment that would minimize subsequent material instabilities. Samples are continuously heated at 200–4000 °C and put through high calcinations temperatures (400–10,000 °C for 1–8 hours) to prevent instability during their working life. Most frequently, breakdown products, including carbon, CO₂ and water, cover the sensor element, gradually losing sensitivity at working temperature.

1.5.4 Response Time

When the sensor is exposed to a full scale gas concentration, the response time is the time it takes for resistance to reach a specified percentage (often 90%) of its ultimate value. Time response is particularly influenced by sensor properties such as crystallite size, additives, electrode shape, electrode position, diffusion rates. A good sensor has a low response time value.

1.5.5 Recovery Time

This is the time that elapses when the sensor is exposed to a full-scale gas concentration before being placed in clean air, at which point the sensor resistance falls to 10% of the saturation value. A good sensor should be able to be used again quickly after recuperation.

1.5.6 Limit of detection (LOD)

The LOD of a gas sensor refers to the least concentration of the target gas that can be accurately differentiated from the absence of the same gas, and it establishes the gas sensor's application domain.

1.5.7 Operating temperature

Any sensor should have a stated working temperature. It depends on the synthesis of the metal oxide and the gas that needs to be detected. It is crucial to specify a parameter in terms of a single gas. The sensor's sensitivity is maximized at a precisely set temperature.

1.6 Methods to improve gas sensing response

a) Doping and catalysts

The presence of dopant and catalysts is a significant element that influence the detecting property of metal-oxide gas sensors [13–14]. In the deposition stage, dopant is added to the metal oxide to modify the material's electrical characteristics. In polycrystalline materials, dopant elements frequently segregate along the grain boundaries and prevent grain development during subsequent annealing. Ionic and electronic defects are produced by dopant electrically. These defect processes affect where the fermi energy level is located, which is believed to affect how

sensitive the metal-oxides are to gases. Catalyzes are substances that quicken a specific chemical process, are often finely disseminated over the surface of the metal oxide. A catalyst must be put on the film's surface of metal-oxide gas sensors to speed up the reaction and hence boost sensitivity. A catalyst is a substance that speeds up a chemical reaction without changing itself. Although the reaction's free energy is unaffected, the activation energy is reduced. In the area of gas sensors, using catalysts is undoubtedly highly successful. In addition, materials used for gas sensing are frequently selected from the oxides used in the catalysis field. Moreover, dispersions of tiny catalyzed particles on the metal-oxide surface boost a specific reduction or oxidation reaction and can lower the sensor's operating temperature, improve the kinetics of the reaction, and increase the sensitivity to a particular gas.

b) Grain size effects

The micro structure of polycrystalline elements is a fundamental component that influences how semiconducting gas sensors sense their environment. Each metal oxide crystallite in the element has an electron depleted surface that extends into the air L times deeper than its surface, where L is a function of the Debye length and the chemisorption strength. The element's gas sensitivity to the reducing gas will alter with D if the crystallite's diameter D is comparable to $2L$ since the entire crystallite is electron-depleted.

The crystallites in the gas sensing elements are connected to their neighbor's crystallites by grain boundary contacts or by necks. In the case of grain boundary contacts, the electrons should be able to traverse a potential barrier, the height of which varies with the surrounding atmosphere. In this instance, the grain size does not affect the gas sensitivity. Electrons travel through the channel that pierces each neck during conduction through necks. The majority of the electron conduction in the sensing element for $D \gg 2L$ (grain boundary control) occurs through grain boundary contacts. The primary method of conductivity modification for $D \geq 2L$ is neck control. For $D \leq 2L$, the electrical resistance of the grains controls sensitivity (grain control) more so than the total resistance of the sensor. The fraction of atoms at the grain boundary increases because the smaller grains produce more surface area. High densities of defects, including as vacancies and dangling bonds, are present at the grain boundaries, and these defects may have a significant impact on the material's ability to transport electrons [17–18].

c) Thickness dependence

Thin and thick film sensing layers have different microstructures and densities, which can lead to slightly different transducer functions [27]. The layer thickness significantly influences the degree of sensitivity of the layers. The sensitivity of the metal oxide sensor is directly influenced by the size of the oxygen-induced depletion layer at the film surface with the bulk metal oxide thickness, as shown in Fig. 1.2.

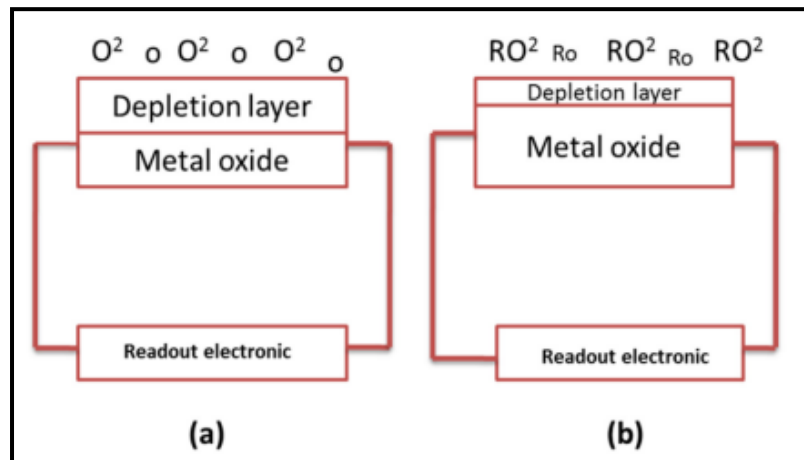


Fig. 1.2: The relationship between sensitivity and the metal oxide's depletion layer depth. (a) The surface of the detecting film absorbs oxygen from air, increasing the film's resistance. (b) When exposed to a reducing gas, the depletion area shrinks, lowering the film's resistance.

A greater sensitivity is often expected when the depletion width and film thickness are equal. Fig. 1.2 (a) shows the depletion area in the natural environment, while Figure 1.2 (b) shows how the depletion depth decreased due to exposure to the reducing gas. When the depletion depth is about equal to the thickness of the sensing film, the resistance will be strong and help to improve the sensitivity.

d) Temperature modulation

One of the crucial factors is the temperature of the sensor's surface. The temperature also affects the dynamic characteristics of sensors, such as response time and recovery, because adsorption and desorption are temperature-dependent processes. At various temperatures, distinct static characteristics are produced through interactions such as thermodynamic surface coverage, co-adsorption, and chemical degradation. On the other hand, the physical characteristics of semiconductor sensor materials, such as the charge carrier concentration, Debye length, work

function are influenced by temperature. The temperature range where the material can catalytically reduce or oxidize the target gas, while also altering the electrical characteristics of the sensor material is suitable for a successful sensor response. For a specific reducing agent, it is discovered that the temperature and rate reaction peak simultaneously with the sensitivity peaks. The rate at which the complete oxidation process proceeds increases with temperature, leading to diffusion restrictions in the concentration of the reducing agent at the surface and a drop in concentration toward zero [19]. On the other hand, when the temperature is too low, the reaction rate is too slow, making it impossible to obtain a high sensitivity.

1.7 Applications of gas sensor

Devices that detect gas are essential for use in several of contexts, such as household life, business, the military, and healthcare [20, 21]. These tools are used to identify the kind and quantity of gases. They are used in

- the process control sector
- testing your breath for alcohol
- detection of hazardous gases in mines fire detection
- boiler control
- environmental monitoring and
- home safety

1.8 Literature survey on Fe₂O₃ gas sensors

The sensing capacity of a gas sensor varies depending on the materials; as a result, research is being done to determine the best material to use. Metal oxides, conducting polymers, carbon nanotubes, and other materials are studied for gas sensing in this process [22, 23]. Among these sensing materials, metal oxides viz., Cr₂O₃, Mn₂O₃, Co₃O₄, NiO, CuO, SrO, In₂O₃, WO₃, TiO₂, V₂O₅, GeO₂, Nb₂O₅, MoO₃, Ta₂O₅, La₂O₃, CeO₂, Nd₂O₃ have been extensively investigated in the past few decades, because of their high sensitivity, and low cost [2, 24]. However, it has challenges of operating at high-temperature range (250-500 °C) [2], and low selectivity has been their limitations. The advantage of metal oxides over other materials is their sensitivity would not degrade as a function of temperature [25].

In the case of metal oxide-based gas sensors, it has been noted that factors such as film thickness, particle size, porosity, operation temperature, doping, affect the sensitivity of the gas sensor [26]. According to research, the sensitivity of the gas sensor improves with decreasing

particle size, particularly with particle size equal to $2L_D$ (Debye length, in the range of 10 nm), and increasing the porosity of the gas sensing oxide material by adding a small amount of noble metal nanoparticles like Au, Ag, Pt, Pd, Rh, Ru, etc. In the past, platinum-based nanoparticles have been employed to boost the sensitivity of gas sensors. Due to the high cost of platinum, new Fe-based oxide nano materials have been created for low-cost gas sensors [27].

The ability to use iron-based metal oxide materials to development of new gas sensors has been investigated by researchers in the survey of metal oxide gas sensors, and is mentioned below.

V. Haridas et al.[28] produced α -Fe₂O₃ nanoparticles on top of graphene sheets via hydrothermal synthesis. At a temperature of 250 °C, the nano composite's XPS examination showed that significant contacts between acidic α -Fe₂O₃ and highly conducting graphene led to a high reaction toward basic NH₃ gas. Additionally, the nano composite's structure and graphene's less flaw-prone nature were revealed by these interactions.

A porous α -Fe₂O₃ hollow sphere array-based ultrasensitive triethylamine (TEA) gas sensor with a particular response has been described by H. Wang et al.[29]. The sensor showed a strong response (75.8) towards 10 ppm TEA with a fast response time (2s) and can detect TEA as low as 50 ppb at a low working temperature (160 °C). When the working temperature exceeded a threshold (>120 °C), this specific reaction to TEA gas was repeated. Furthermore, it was discovered that the instantaneous attenuated reaction was strongly connected to certain gases, irrespective of humidity and gas concentration.

By using a hydrothermal technique and a subsequent annealing procedure, HOU Lin et al.[30] effectively synthesized γ -Fe₂O₃ microspheres made up of nanoparticles. Particularly at working temperatures as low as room temperature, synthesized γ -Fe₂O₃ microspheres displayed high sensitivity for the detection of ethanol gas. According to the results of the gas sensing, at the ideal operating temperature (200 °C), the limit of detection (LOD) for γ -Fe₂O₃ microspheres for 1000 ppm ethanol gas was around 0.026 ppm. However, the γ -Fe₂O₃ microspheres demonstrated remarkable selectivity over other gas species, great stability, and a robust response to ethanol gas concentrations ranging from 1 to 1000 ppm at ambient temperature.

Z. Cao et al.[31], used Raman and XRD to investigate the gas-sensing capabilities of the Fe-based metal-organic gel-derived α -Fe₂O₃ sensing material. The changes in the surface oxygen vacancy of α -Fe₂O₃ caused by thermally induced lattice expansion and the active mode

of α -Fe₂O₃ as a gas-sensing material can be seen in the observed Raman scattering signals during acetone gas sensing. The α -Fe₂O₃ gas sensor showed excellent gas-sensing capabilities with a high response value of 27, rapid response/recovery time was 1 s/80 s for 100 ppm acetone gas, and broad response range was 5 - 900 ppm at 183 °C.

A.K. Basu et al.[32] developed α -Fe₂O₃ nanoparticles embedded in layered rGO (Graphene oxide) sheets and showed them to be a viable material for the temperature-independent, sensitive detection of CO gas. Compared to pure α -Fe₂O₃, the nano composite rGO α -Fe₂O₃ demonstrated better CO gas sensing properties. The extraordinarily high surface area was 19.047 m²/gm rGO α -Fe₂O₃, the low response was 21 s at 10 ppm, and fast recovery durations were 8 s at 10 ppm of rGO sheets all contributed to their improved sensitivity. The substance exhibited strong selectivity for CO gas and p-type semiconducting behaviour at normal temperatures.

According to N. Zahmouli et al. [33], Gd-doped γ -Fe₂O₃ nano powders with varying Gd concentrations (1, 3 and 5 at.%) were made using the method of sol-gel and then dried in supercritical ethanol. Scanning and transmission electron microscopy, X-ray diffraction, and BET analysis were used to study the structural and morphological characteristics of the synthesized materials. Furthermore, optical studies were made using photoluminescence and UV-visible analysis. The Gd-doped γ -Fe₂O₃ nano powders' pores size, BET surface area, optical band gap, electrical conductivity, and photoluminescence were all significantly impacted and were shown to be composition-dependent. Gd-doped samples showed improved gas-sensing characteristics towards acetone, 3 at. % Gd-doped maghemite based gas sensor exhibited the higher response of 31.2 toward 20 ppm of acetone, which was 30 times larger than of pure γ -Fe₂O₃.

Y. Huang et al.[34] described the production of porous α -Fe₂O₃ nanoparticles by simply annealing β -FeOOH precursor produced by a straightforward hydrothermal method. Transmission electron microscopy (TEM), scanning electron microscopy (SEM), and X-ray diffraction (XRD) were used to characterize the product's structures and morphologies. The results showed that the generated porous α -Fe₂O₃ contained multiple pores with sizes ranging from 2 nm to 10 nm, which were dispersed irregularly over the particle surface and had an average crystallite size of 34 nm. The gas-sensing capabilities of the porous α -Fe₂O₃

nanoparticle-based sensor were studied; the greatest sensitivity was 38.4 for 100 ppm H₂S at ambient temperature, with a 50 ppb detection limit.

Using FeOOH nano rods as a precursor, J. Hong et al. [35] established a hydrothermal method for the controlled production of hexagonal bipyramid α -Fe₂O₃ microcrystal. According to the SEM, TEM and BET analyses HB α -Fe₂O₃ MCs exhibited a flawless hexagonal bi-pyramid structure with a specific surface area of 78.2 m²g⁻¹. Because of their structural advantages, HB α -Fe₂O₃ MCs functioned as a gas sensor and demonstrated remarkable sensor response, selectivity, and response/recovery times towards ethanol gas, with response times of 2 seconds and recovery times of 23 seconds for 900 ppm ethanol at 320 °C.

α -Fe₂O₃ nanoparticles on graphene were created by S. Liang et al. [36] as a gas sensor material. According to the XRD and TEM data, α -Fe₂O₃ nanoparticles of varied sizes and shapes are used to embellish graphene sheets. The examination of sensors for the detection of ethanol yielded data that effectively boosted the gas-sensing capabilities of α -Fe₂O₃ when operated at various temperatures. Pure α -Fe₂O₃, α -Fe₂O₃ -G (0.01), α -Fe₂O₃ -G (0.02), and α -Fe₂O₃ -G (0.03) had maximal response values of 10, 21, 30, and 12, respectively, to 1000 ppm ethanol at 280 °C. The α -Fe₂O₃ -G (0.02) nano composite exhibited a higher response value than each of its components (pure α -Fe₂O₃). However, the reaction value drastically dropped to 12 when graphene content approached 3%.

According to S.T. Navale et al. [37] Nano structured Fe₂O₃ thin film sensor was created on a glass substrate, using the sol-gel spin coating process. SEM, FESEM, and XRD analyses of the morphology and crystal structure of Fe₂O₃ nanoparticles revealed the production of hexagonal Fe₂O₃, with a particle diameter of 40 nm. By using AFM to measure the roughness of the film surface, it was determined that the nano structured morphology was appropriate for use in gas sensing applications. The gas sensing measurements at 200 °C demonstrated the selectivity of Fe₂O₃ films for NO₂ gas, with a maximum response of 17.12% at 200 ppm and 59.44% stability. It was also discovered that as the NO₂ concentration rose from 10 to 200, the response time decreased from 20 to 12 seconds while the recovery time increased from 101 to 188 seconds.

Polypyrrole (PPy)/ α -Fe₂O₃ nanocomposites have been created by S.T. Navale et al. [38] using the sol-gel process. The presence of α -Fe₂O₃ nanoparticles in the PPy matrix has been confirmed using a various techniques, including X-ray diffraction, Fourier transform infrared

spectroscopy, and field emission scanning electron microscopy. The PPy/ α -Fe₂O₃ nanocomposites (50%) with the best reaction (54%) and stability (85%) to 100 ppm NO₂ at room temperature were all PPy/ α -Fe₂O₃. It was assumed that the synergetic impact of PPy and α -Fe₂O₃ or the effect of p-n hetero junctions was the gas-sensing mechanism of PPy/ α -Fe₂O₃ materials to NO₂. The PPy/ α -Fe₂O₃ hybrid sensor had better features than pure PPy or pure α -Fe₂O₃, including more stability, higher gas sensitivity than PPy at ambient temperature, and lower operating temperature than α -Fe₂O₃.

S. Si et al.[39] reported approach of solution phase controlled hydrolysis was used to create Fe₂O₃/ZnO core/shell nano rods, which were then characterized using XRD and TEM methods. The Fe₂O₃/ZnO gas sensor displayed a high response, good stability, and a short response/recovery time in the sensing of low concentrations of various combustible gases, with the maximum response to ethanol and acetone being observed at 200 C, according to BET results that showed the surface area of these core/shell nano rods were higher than that of bulk ZnO sensor materials. Less than 20 seconds passed between the response and recovery, and after 4 months, there was a modest decline in responsiveness.

To demonstrate the α -Fe₂O₃ micro cubes' gas sensing abilities, P. Sun et al.[40] developed them using a hydrothermal method at varying Cu weight percentages for 12 hours at 160 °C. The X-ray diffraction results showed that due to the inclusion of Cu, the lattice constants of added samples were marginally lesser than those of the pure sample. At the working temperature of 225 °C, it was discovered that the sensor based on Cu-doped α -Fe₂O₃ (3.0 wt%) had a response time of 19s for 100 ppm ethanol, which was about 3 times greater than that of the pure α -Fe₂O₃ nanostructures with response and recovery times of 4s and 34s.

The gas sensitivity of α -Fe₂O₃ nanoparticles in the shapes of nano rods, nano tubes, and nano cubes that are produced by a hydrothermal method and calcinations has been examined by Tao et al. [41]. The characteristics of the nanotubes improved gas sensitivity. The nano tube sensor responded to acetone, ethanol, formaldehyde, and ammonia at 75, 26, 6.8, 1.7 to 200 ppm, respectively, at 270 °C and 30-45% relative humidity, demonstrating good selectivity.

As the next-generation materials for gas sensing, the relevance of Fe₂O₃ micro- and nanoscale materials has been highlighted by Long et al. [42]. In order to improve the iron oxide-based materials' sensitivity to gases, they have briefly addressed the significant modifications and additions made to their structures. They also asserted that Fe₂O₃ particles with a size range

of roughly 10 μm could differentiate between different gases at low concentrations and were especially sensitive to different alcohols, with a sensitivity of nearly 90% for ethanol. They proposed that Fe_2O_3 and Fe_3O_4 -based oxide nanoparticles may be used to make high-quality, reasonably priced gas sensors.

The methane (CH_4) gas sensing capabilities of Fe_3BO_6 nanoplates and nanobars have been examined by Kalpana Kumari et al.[43] as a function of annealing temperature (microwave annealing for 15 minutes at 823 K and 1023 K). The 1023 K annealed sample's temperature-dependent sensitivity to CH_4 (1000 ppm) shows a maximum value of 43% at a working temperature of 525 K. When the CH_4 gas concentration is adjusted from 50 to 1000 ppm, they discovered that sensitivity varies from 9% to 39%, and the sensor exhibits a quick reaction (1 min) and a decent recovery time (1.6 min) when compared to other oxide materials.

Alex Punnoose created a magnetic hydrogen sensor at the nanoscale [44]. In the presence of hydrogen gas flow (at a concentration of 1–10% and a temperature of 575 K), they found that the saturation magnetization and remanence of nanoscale hematite increased by one to two orders of magnitude. This suggests that the practical utility of the magnetic hydrogen sensor based on hematite material for hydrogen production, storage, and transportation.

Using the spray pyrolysis method, R. B. Ayed et al.[45] produced iron oxide (Fe_2O_3) thin films on glass substrate by adjusting the substrate temperature (T_s) from 300 to 450°C. It was investigated how T_s affected the physical characteristics of Fe_2O_3 layers. The highest Hall mobility of $62 \text{ cm}^2 \cdot \text{V}^{-1} \cdot \text{s}^{-1}$ and film crystallinity were both reported at 400 °C. The band gap ranges from 2.07 to 2.16 eV for direct transition and from 1.67 to 2 eV for indirect transition. The gas sensing data shows that $\alpha\text{-Fe}_2\text{O}_3$ has good sensitivity and stability at 400 °C working temperature.

By using the sol-gel process, J. Patil et al.[46] created a spinal-type nano crystalline MgFe_2O_4 gas sensor. Due to sintering at two different temperatures (973 K and 1173 K), the material has discrete morphologies and exhibits excellent gas-sensing characteristics for acetone throughout a broad working temperature range (575–675 K). It was also noted that the sensors had a quick response and recovery, showing tremendous promise for future industrial uses as gas sensors.

CuFe_2O_4 magnetic gas sensor was created by D. Matatagui et al.[47] by spin coating CuFe_2O_4 nanoparticles onto YIG film. They examined various organic volatile substances at 50,

75, 100, 150, 200, 250, and 300 ppm, including dimethyl formamide, isopropanol, ethanol, benzene, toluene, and xylene. All of these were detected with great sensitivity, quick response times, and good reproducibility using the sensor, which operates at room temperature.

R. B. Ayed et al. [48] looked at the physical and gas-sensing properties of pure and Al: Fe₂O₃ thin films made by spray pyrolysis. According to the XRD investigation, all layers crystallized in a rhombohedral form, with (104) serving as the layers' preferred orientation. Al: Fe₂O₃ (6 and 8 at.%) was shown to be very transparent through optical examinations. Additionally, the band gap values in the 1.98 to 2.17 eV range were discovered. The 8% Al: Fe₂O₃ thin films in the Hall Effect measurements showed the lowest resistance of $2.68 \times 10^2 \Omega\text{-cm}$, indicating an n-type conductivity. The aluminum-doped thin films were also claimed to have identified ethanol sensing at 0.1 and 0.5% concentrations, the sensitivity increasing from 5.19% to 19.93% at an operating temperature of 250°C.

By using a straightforward evaporation process, E. Ranjith Kumar et al.[49] generated nano crystalline Mn-Cu ferrite powders. The effects of the annealing procedure on the samples' structural and magnetic properties were examined. The material-based sensor's sensitivity to LPG gas was exceptionally high. The optimal response to LPG was achieved at 250 °C for 1000 ppm and a reaction and recovery period of 40 s. This sensor material benefits our daily lives and is a cutting-edge, economical material for LPG gas sensor applications.

C. Wang et al.[50] successfully created a highly sensitive and selective acetone gas sensor by developing an n-n hetero junction made of TiO₂ nano rods and α -Fe₂O₃ branches. Studies using X-ray diffraction and scanning electron microscopy showed that TiO₂ nano rod arrays were successfully formed on TiO₂ stems during hydrothermal processes and that α -Fe₂O₃ branches successfully developed on the surface of Al₂O₃ ceramic tubes. These nano rod branches' lengths may be adjusted by varying the proportion of iron precursor. The TiO₂ nano rod sensors' gas detection capabilities under pristine and α -Fe₂O₃ branch decoration were examined. The findings showed that the sensor based on TiO₂/ α -Fe₂O₃ hetero structures evaluated at 225 °C had a greater response of 21.9 towards 100 ppm of acetone gas, which was approximately 9 times higher than the pure TiO₂ nano rods sensor.

One-step hydrothermal synthesis was used by Zhonglin Wu et al. [51] to create α -Fe₂O₃ nano-ellipsoids, which were then tested as extremely sensitive H₂S-sensing materials. The nano-ellipsoids' average long-axis and short-axis diameters are 275 nm and 125 nm, respectively. At

an ideal working temperature of 260 °C, H₂S gas sensors made using α -Fe₂O₃ nano-ellipsoids demonstrated outstanding H₂S sensing capability. The response and recovery durations for H₂S gas at a concentration of 50 ppm were 0.8 s and 2.2 s, respectively. Compared to other often studied gases such as NH₃, CO, NO₂, H₂, CH₂Cl₂, and ethanol, the α -Fe₂O₃ nano-ellipsoid-based sensors also showed remarkable selectivity to H₂S. Additionally, the sensors showed great repeatability, long-term stability, and high response values to various H₂S concentrations with detection limit as low as 100 ppb.

W. Yan et al.[52] used a simple solution method to create flower-like α -FeOOH precursors by employing CO(NH₂)₂ and FeSO₄•7H₂O as raw materials for 6 hours at 80 °C without needing a template or surfactant. The porous flower-like α -Fe₂O₃ superstructures were effectively created after being annealed in the air for two hours at 500 °C. Their morphological feature was described as being self-assembled by porous nano rods with an average length of 0.1-1.0 μ m and diameter of 50-150 nm. Transmission electron microscopy (TEM) images revealed several porous walls with pores as small as 10 nm on the surface. Compared to α -Fe₂O₃ nano particle aggregations, the porous flower-like superstructures reacted to gas faster, with reaction and recovery periods of only 6 to 3 seconds. They also responded to concentrations of ethanol, methanol, and acetone.

Using a low-cost, environmentally friendly hydrothermal technique, B. Zhang et al. [53] synthesized reduced graphene oxide (rGO) and produced rGO/ α -Fe₂O₃ composites with varied rGO concentrations. The α -Fe₂O₃ cubes attached uniformly on both sides of the crumpled and rippled rGO sheets, according to approaches that characterized the chemical composition and morphological essence of the samples as they were created. Additionally, a number of resistive-type gas sensors based on the rGO/ α -Fe₂O₃ composites as-prepared as well as pure α -Fe₂O₃ were made in order to compare their acetone vapor-sensing capabilities. The composite with 1.0 wt% rGO showed an improved gas response, and its response time were reduced to 2s. The reason is attributed to the creation of local p-n hetero junctions when rGO is introduced, which results in the extension of electron depletion layers and a change in charge carrier concentration.

Using molecularly imprinted powders (MIPs), which offer unique recognition sites for methanol, Q. Zhu et al.[54] created an Ag-LaFeO₃-based gas sensor with high responsiveness and selectivity. The investigation into the gas sensing capabilities of MIPs for methanol revealed that the best gas sensing capabilities for methanol vapour are demonstrated by sensors based on

MIPs, namely those with $x = 1:4$ ($x =$ methanol methyl acrylic acid, molar ratio). The sensor's response ($x = 1:4$) to 1 ppm methanol is 41 at the optimal operating temperature of 130 °C, and the response and recovery durations are 40 s and 50 s, respectively.

D. Matataguiet al.[55] have developed magnonic gas sensor by spin coating technique based on magnetic nano particle layers of thickness between 5 μm to 10 μm of $\text{CuFe}_2\text{O}_4/\text{MnFe}_2\text{O}_4/\text{ZnFe}_2\text{O}_4/\text{CoFe}_2\text{O}_4$ and tested with dimethyl formamide (50, 75, 100, 150, 200 and 250 ppm), isopropanol (400, 600, 800, 1000 and 1200 ppm), xylene (75, 100, 125, 150, 175 and 200 ppm) and toluene (300, 600, 800, 1000 and 1200 ppm). Their result revealed that due to the change in the magnetic properties of the layers, magnonic sensors are highly sensitive to toxic gases, fast detection, recovery response, and high reproducibility in detecting gases.

A LPG sensor made of thin films of hematite and carbon nanotubes (CNT) nano composite was reported by B. Chaitongrat et al. [56]. Chemical vapour deposition was used to create the hematite and CNT nano composite. The CNT is a highly conductive material, while the hematite is an n-type MOS. In CNT, the nanostructure is hollow. Each hematite-CNT displayed a p-type response. The performance of the hetero structure and nano composite was n-type. Individual responses took longer to respond than composite responses did. The composite structure, which was 0.25 times the lower explosive limit, also picked up on the LPG of 0.5 vol%. The reducing natures of LPG and oxygen adsorption were used to explain the gas sensing mechanism. Another lanthanum ferrite investigation also revealed LPG sensing activity.

A study using strontium ferrite thin films for an LPG sensor was published by M. Singh et al. [57]. Strontium ferrite ($\text{SrFe}_{12}\text{O}_9$) was prepared using the chemical co-precipitation process. On a glass substrate, the films were created. A recorded minimum crystallite size is 18 nm. The films at room temperature revealed a 7% sensitivity to LPG. Most LPG is composed of propane and butane. The films have a 52.45 $\text{M}\Omega$ resistance to 0.5 vol% LPG.

A Mirzaei et al.[58] demonstrated using of an ethanol sensor made of $\alpha\text{-Fe}_2\text{O}_3$ and Co_3O_4 nano composite. The nano composite was made using the hydrothermal method. The composite demonstrated three times the sensitivity compared to pure iron oxide gas. Composite responded well to 200 ppm of ethanol at 300 °C. The sensitivity was linked to possible interface barrier development. Co_3O_4 's catalytic and increased oxygen adsorption significantly influenced the gas sensing performance. P-type and n-type hetero structures may have significantly influenced the adsorption and desorption of ethanol.

S Saritas et al.[22] has investigated the morphological structure (particle size, pore size, etc.), optical, magnetic and electrical properties of Ni: Fe₂O₃, Mg: Fe₂O₃ and Fe₂O₃ thin film gas sensors grown by Spray pyrolysis. The sensor temperature of 225⁰C was chosen as optimal temperature for the sensor response and the Ni:Fe₂O₃, Mg:Fe₂O₃ and Fe₂O₃ gas sensors response dependence on gas flow rate.

Currently, the technical challenges in controlling micro and nano scale metal oxide systems are uniform size, shape, structure, and composition. For the detection of CO, CO₂, CH₄, O₂, H₂, and C₂H₅OH gases, novel polyhedral metal oxide particles with grain and grain boundaries are proposed [2] to increase the selectivity and sensitivity of gas sensors. More crucially, metal oxides are attractive choices because of their extremely low cost yet extremely high endurance and stability. All the sensor devices using metal oxide-based materials are generally suitably compatible with hybrid microcircuit technology through standard semiconductor technology, such as Si and SiC. The ultimate goal of shaping Fe-based sensors in size and shape allows for finding cheap, new, and efficient materials in gas sensing.

1.9 Gaps in the existing literature

According to the literature review mentioned above, the preparation technique and optimization of the deposition parameters have the biggest impact on the properties of the films. The stabilization of the phase for thin films of iron-based oxide films by chemical means as a function of form, structure, and chemical composition is not actively investigated, despite the fact that iron oxide films have been created using a variety of physical and chemical techniques. Enhancing the sensing mechanism of iron-based oxide films to improve sensor performance is necessary.

1.10 Objectives of the current study

The primary objective of this investigation is to investigate the gas sensing abilities of Fe₂O₃. According to earlier literature, Fe₂O₃ can be employed as a basis material for gas sensing applications. According to reports, Fe₂O₃ can be a promising material for industrial gas sensor applications by being modified, using a nano structured form of the material, and managing the physical structure of the film. The main goals of the current research work are:

- Preparing pure and doped thin films of Fe₂O₃ material using a spray pyrolysis process.

- To examine the thin films' gas-detecting capabilities.
- Using additives to change the physical characteristics of films and investigating how the additives affect gas sensing performance
- Investigating the impact of annealing temperature on gas sensing performance, material phases, and film structure.
- Analytical techniques such as XRD, SEM, EDAX, AFM, Raman spectroscopy, and UV-VIS spectroscopy to characterize the materials thin films.

1.11 Definition of the problem and outline of the thesis

After conducting a thorough and critical review of the literature, it was determined to conduct research on "Studies on gas sensing performance of pure and Al doped Fe₂O₃ thin films".

The current work is organized into five chapters that together provide the overall picture of the work done.

- The first chapter covers a broad introduction to gas sensors as well as a review of relevant literature.
- The experimental methods utilized to synthesize and characterize Fe₂O₃ thin films are covered in the second chapter.
- The methods for preparing and characterizing Fe₂O₃ thin films for ammonia gas sensing are covered in the third chapter.
- The methods for synthesizing and characterizing Al-doped Fe₂O₃ thin films for formaldehyde gas detection are covered in the fourth chapter.
- The thesis's conclusions and the direction for further research are covered in chapter five.

2.0 Introduction

This chapter discusses the fabrication techniques for developing of pure and Al-doped iron oxide thin films. Additionally, several methods are covered for analyzing materials used to investigate the structural, optical, morphological, and elemental characteristics of produced thin films are covered. This chapter also explains the construction of the sensing chamber and the tools used for sensing analysis of the generated sensors.

Numerous preparation methods exist to prepare pure and composite thin films. They can be divided into two groups: (a) physical routes and (b) chemical routes. Vacuum-based methods are one of the physical ways that are frequently used for the creation of thin films. Sputtering, molecular beam epitaxy, e-beam evaporation, pulsed laser deposition, etc. are examples of vacuum-based processes. Methods like drop-casting, dip coating, spray pyrolysis, and sol-gel spin coating are frequently employed to synthesize thin films by the chemical route. The development of pure and doped metal-oxide thin films has been accomplished using spray pyrolysis.

Verification of the work done during the research process is crucial. The caliber of the methods and standards applied during the research determines the caliber of the work produced. In research, confirming the results using appropriate standards and methods is crucial. The following information is necessary for a solid to be properly characterized:

- The solid's form, such as whether it is mono crystalline or polycrystalline, and if so, how many, how big, how distributed, and what kind of crystal structure it has.
- The impurities that are present and whether they are randomly dispersed or concentrated in specific areas; the crystal flaws that are present, including their nature, number, and distribution; and
- The sub lattice properties

Diffraction, structural and microscopic techniques are the three primary subcategories of physical techniques. Heat analysis, magnetic, and physical property measurements also provide useful data. Numerous physical characterization techniques used in the research are covered in this chapter. This section contains information on morphological examinations, elemental analysis, phase analysis, X-ray diffraction (XRD), and scanning electron microscopy (SEM). The

following techniques were used in the current study: atomic force microscopy (AFM), energy dispersive analysis by X-ray (EDAX), transmission electron microscopy (TEM), and UV-visible spectroscopy. A static gas-sensing system is utilized to investigate the gas-sensing properties of synthesized thin film.

2.1 Experimental Techniques

2.1.1 Thin film Deposition Technique

A thin film is an essentially two-dimensional material formed by the condensation of atomic, molecular, and ionic species of matter [59-61]. On a single crystal substrate, thin films are produced by the deposition of individual atoms. While a low-dimensional substance created by thinning a three-dimensional material or by building huge clusters, aggregates, or grains of atomic, molecular, or ionic species is what is typically meant by the term "thin film," it is also possible to define thin films in other ways. Since more than 50 years ago, thin films have been widely used to produce a range of devices, including electrical devices, instrument hard coatings, optical coatings, decorative parts, etc. Even though thin-film technology is a well-established area of materials science, it is constantly evolving to keep up with the demands of the twenty-first century for the development of novel materials like nanostructure materials and/or synthetic super lattices. Thin film technology ancient and modern key material technology is. Several studies [62-64] have assessed thin film components and deposition processes. Many techniques can be used to deposit thin films, including thermal evaporation, chemical breakdown, spin coating, spray pyrolysis, and sputtering. The formation of thin films frequently exhibits the following characteristics.

- The random nucleation procedure, followed by the nucleation and growth stages, is the first step in the producing thin films of any materials using any deposition technique.
- Various deposition variables, including growth temperature, growth rate, the chemistry of the material and the substrate, and their structure, have an impact the nucleation and development stages.
- The deposition conditions at the nucleation stage influence the film's microstructure, the associated defect structure, and the film stress.

- External factors like electron or ion bombardment can significantly modify the nucleation stage.
- The substrate's structure and the deposition circumstances determine the films' orientation and crystal phase.

The deposition conditions impact the film's composition, crystal phase and orientation, thickness, and microstructure, which are all fundamental properties. The peculiar properties observed in thin films but not in bulk materials include quantum size effects, the effects of strain, and the outcome of multilayer features that result in various proximity effects. A lot of study has been done on using thin films in the manufacturing electronic devices [65–67]. One of the inventors of thin film deposition technology, Prof. K. L. Chopra [59], once stated that "the thin film was in the past considered as the fifth state of matter next to plasma since the properties of the reliable materials could not be obtained, and thin films were considered to be different from bulk materials, at present the thin films are considered as the first state of matter.

The choice of various deposition processes depends on a several parameters, including

- The way the film is made
- The kind of substance that will be deposited.
- The kind of substrate to be utilized
- The necessary film thickness
- Applications of the thin film

Thin film synthesis techniques are classified [68] as

- Physical method
- Chemical methods

Physical approaches are expensive and require exact boat temperature control to produce acceptable stoichiometry films. The following benefits are provided by chemical processes over physical methods, which are more affordable and simpler.

1) Deposition does not require vacuum. 2) Any needed element can be added easily. 3) It may benefit extensive industrial applications, and 4) Minimal material loss during deposition. Every technique has pros and cons of its own. One of the more beneficial chemical processes is spray

pyrolysis. Therefore, this study uses spray pyrolysis to create Fe_2O_3 -based thin films for gas sensor applications.

Table 2.1: Methods of thin film deposition

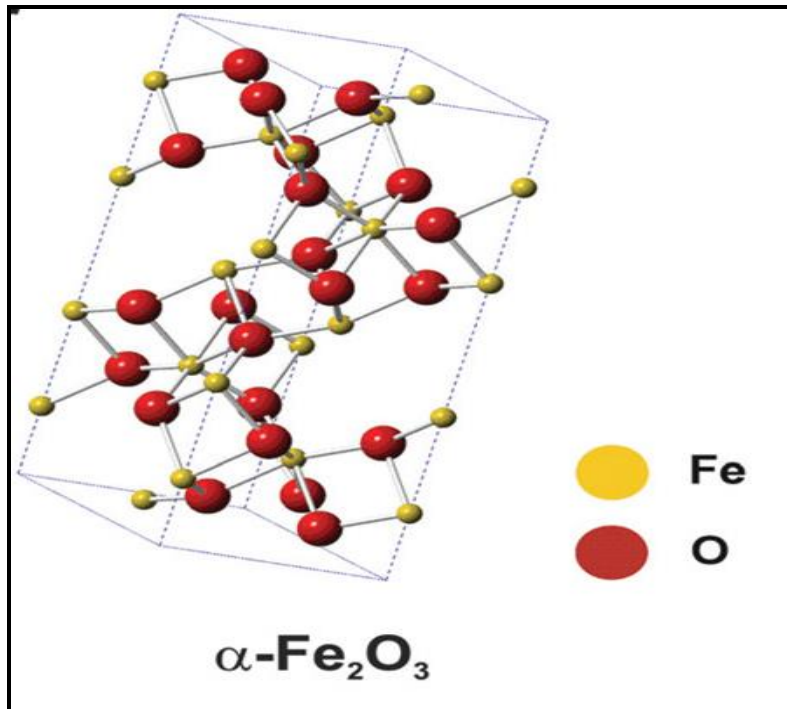
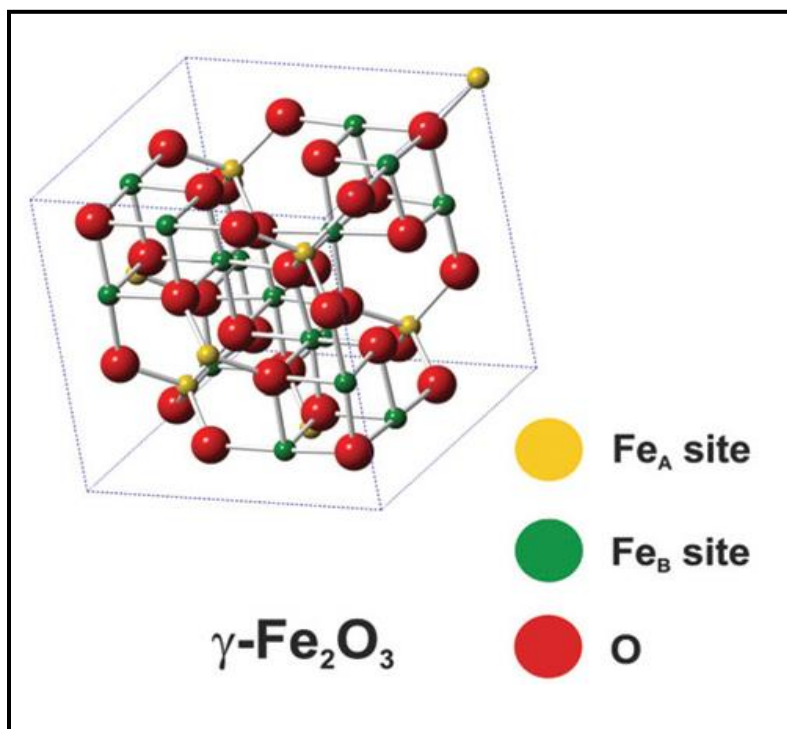
Physical method		Chemical method	
Sputtering	Evaporation	Liquid Phase	Gas Phase
DC Sputtering	Arc Evaporation	Spray Pyrolysis	Atmospheric Pressure Chemical Vapour Deposition
RF Sputtering	Flash Evaporation	Chemical Bath Deposition	Low Pressure Chemical Vapour Deposition
Magnetron Sputtering	Thermal Evaporation	Electro Deposition	Laser Chemical Vapour Deposition
Ion Beam Sputtering	Electron Beam Evaporation	Spin coating	Plasma Enhanced Chemical Vapour Deposition
Reactive Sputtering	Pulsed Laser Deposition	Dip coating	Metal Organic Chemical Vapour Deposition

2.1.2 Iron oxide as a sensing material

According to the latest research results, among all metal oxides, Fe_2O_3 has drawn significant interest in the past decades due to its chemical stability, catalytic behaviour, abundance in nature and wide range of applications in various technical fields. Since gas sensing properties depend on the crystallite shape, size, morphology, etc., the required properties for gas sensing can be obtained in the case of Fe_2O_3 by changing the deposition temperature and doping.

Fe-O system exist in FeO , Fe_3O_4 (magnetite) and Fe_2O_3 polymorphic forms, $\alpha\text{-Fe}_2\text{O}_3$ (hematite) and $\gamma\text{-Fe}_2\text{O}_3$ (maghemite) are the two typical forms of Fe_2O_3 .

Three different forms of defect species oxygen vacancies, Fe^{3+} interstitials, and Fe^{2+} interstitials are present in the defect structure of $\alpha\text{-Fe}_2\text{O}_3$. Semiconducting qualities result from the presence of these flaws. Whereas excess oxygen (into the lattice as O_2) causes an electron deficit (i.e., introduces electronic holes) and produces p-type behavior, loss of oxygen leaves

Fig.2.1: $\alpha\text{-Fe}_2\text{O}_3$ structure (Rhombohedral)Fig.2.2: $\gamma\text{-Fe}_2\text{O}_3$ structure (Cubic/Tetragonal)

behind additional electrons and results in an n-type semiconductor. Therefore, in $\alpha\text{-Fe}_2\text{O}_3$, alterations in gas concentration, dopant selection, and/or operating temperature can induce a shift from n-type to p-type response, or vice versa. Fe_2O_3 is known to be extremely sensitive to organic gasses [28–34]. Fe_2O_3 has been doped with different metal oxides to make it selective for a given gas [46-49].

2.1.3 Spray Pyrolysis (SP) Technique

Alexander Letnyi likely invented the first Pyrolysis method in 1877 [69]. However, Chamberlin and Skarman used the Spray Pyrolysis process for the first time in 1966 to create CdS thin films for solar cell applications [70]. SP technique is a procedure in which tiny droplets of a precursor solution containing the chemical components are formed and sprayed onto a heated substrate. The precursor then thermally decomposes, generating an adhering thin layer of a thermally more stable chemical, and it is a chemical deposition technique widely used to manufacture thin films of transparent conducting oxide (TCO) [70]. The SP technique approach proved a particularly appealing technique for generating thin films of noble metals, metal oxides, spinel oxides, superconducting compounds, and binary and ternary chalcogenides [71-74]. Dense or porous oxide films, ceramic coatings, and powders have all been successfully deposited using this SP method. And also, with the spray pyrolysis method, even stacked films can be produced easily.

The SP technique doesn't need expensive chemicals or substrates. This method is one of the most widely used for a variety of applications due to its simplicity, high productivity, minimal waste production, ease of doping, control over thickness, potential for multilayer deposition, simplicity in preparing thin films of any composition, non-vacuum system of deposition, and low cost. Materials produced with the SP process are used in a variety of products, including solar cells, optoelectronic devices, thermoelectric coolers, antireflective coatings, decorative coatings, gas sensors, and electro chromic devices [75].

The SP technique has become the most used chemical method in recent years due to its ability to create thin films of various conducting and semiconducting materials [76]. It is simple to integrate into any industrial production line because of its capacity to make adherent films with a uniform thickness across a vast area. Systems for mass manufacturing can also be used

successfully with the spray pyrolysis approach. The current study uses the Spray Pyrolysis process to produce pure and doped Fe_2O_3 materials as thin films.

The usual equipment for SP technique includes a spray nozzle, heater, thermocouple, air compressor, substrate, atomizer control system, and reservoir for the precursor solution. The spray pyrolysis setup is shown schematically in Figure 2.3, and the photograph of the system used in this work is shown in Figure 2.4.

Spray nozzle: Through the use of a spray nozzle, a solution can be squeezed into tiny droplets. With filtered carrier gas such as air, which may or may not be engaged in the pyrolytic reaction, the spray nozzle atomizes the chemical solution into a spray of tiny droplets. The carrier gas and the solution are delivered into the spray nozzle at a predetermined constant pressure and flow rate. Different types of nozzles, including air blast, ultrasonic, and electrostatic nozzles, are used to spray solutions.

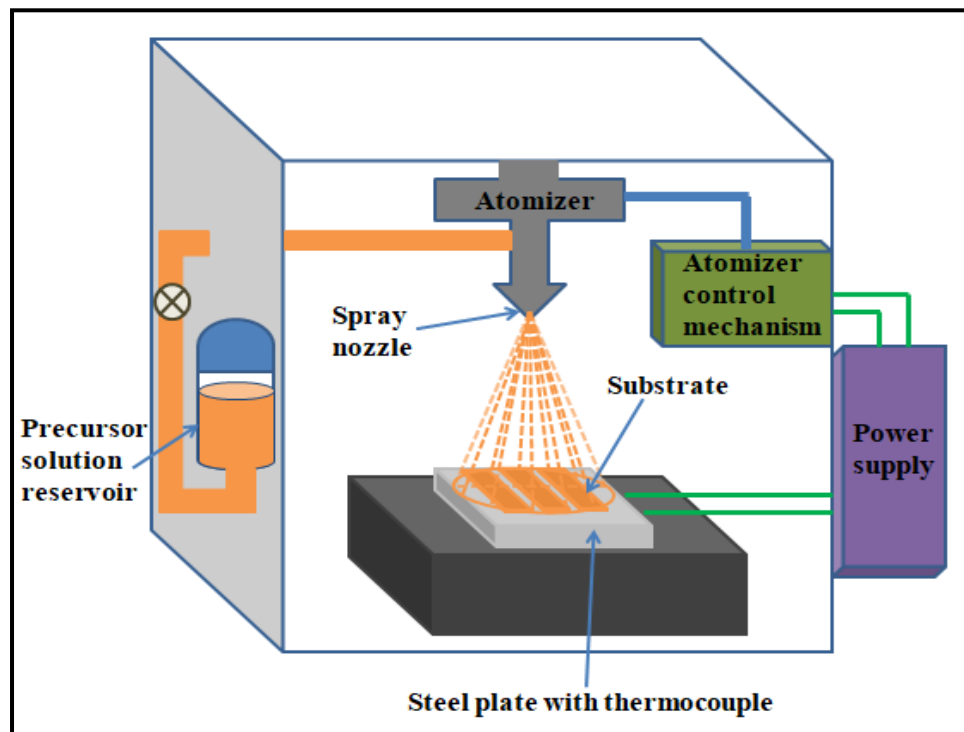


Fig.2.3: Schematic representation of spray pyrolysis deposition apparatus

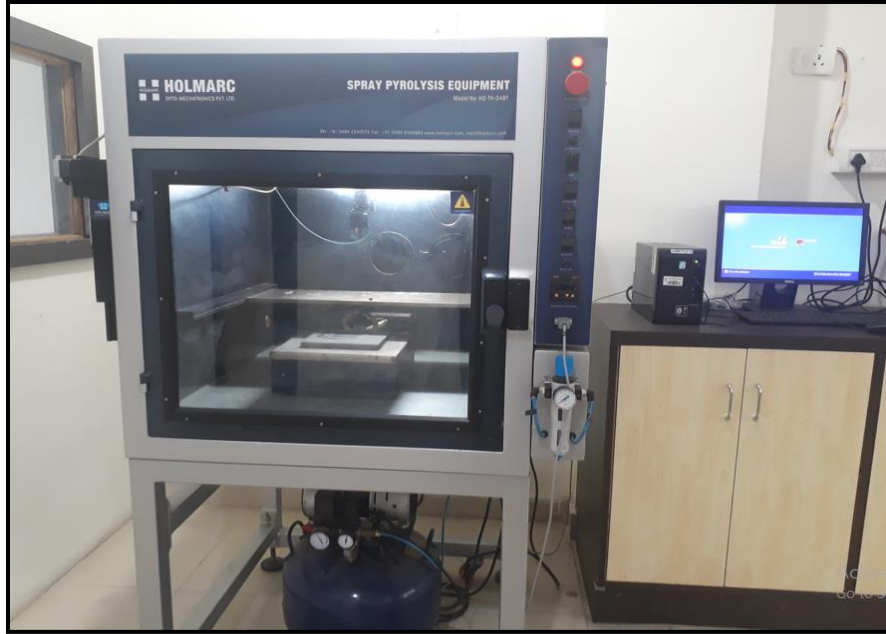


Fig. 2.4: Photograph of Spray pyrolysis system used in present work.

The geometry of the nozzle greatly influences the spray pattern. . In the present investigation, an air blast type of metallic nozzle with an inner diameter of 0.5 mm and a 0.7 mm outer diameter of bore was used.

Solution reservoir: The solution is kept in this tank, which also houses the reaction-inducing additives and the components necessary for the material to be deposited as a liquid.

Substrate: This is the substance on which the film will be applied. Glass substrates of 75 mm by 25 mm by 2 mm are employed in the current experiment.

Air compressor: This machine delivers compressed air into the chamber through a nozzle. The airflow may be changed by utilizing a valve, and an airflow meter can control it.

Spraying chamber: The spraying chamber is made up of fiber and metal, inside this chamber spraying assembly is mounted.

Atomization system: A stepper motor-based microprocessor controller is used in this system to regulate the spray nozzle's motion.

Electric heater: The glass substrate is heated to the desired temperature using the electric heater. It is made possible so that externally maintained controlled levels of various constant temperatures.

Thermocouple system: It is employed to detect temperature changes. In the current study, a thermocouple of the Cr-Al type was utilized.

Temperature gauge: This displays the substrate's temperature.

Exhaust fan: This is employed to eliminate waste products.

Compressor: This device generates the air pressure needed to deliver the precursor solution at the specified flow rate.

2.1.4 Advantages and Disadvantages of Spray Pyrolysis (SP)

Advantages: The following are some of the main benefits of the SP technique in comparison to other techniques: (a) It is one of the simple, low-cost techniques that can be utilized to mass create thin film coatings. (b) For atmospheric large-area depositions, this is a fast coating technique that is available. (c) Process factors, like substrate temperature, solution concentration, doping level, spray rate, and nozzle-substrate distance, that have an impact on thin films' attributes straightforward to change. (d) It is conceivable for growth to occur quickly. (e) Using the SP approach, uniform, firmly adherent, and pin-hole-free coatings can be produced. (f) Vacuum is not required. (g) The SP process can be used to synthesize multi-component alloys. (h) It doesn't demand top-notch substrates or targets. (i) It offers a relatively straightforward way for doping thin films in any ratio by adding any element to the spray solution. (j) By varying the composition of the spray solution as it is being applied, layered films and films with composition gradients throughout their thickness can be made. (k) Deposition can be done between 100 and 500 °C (l) Changing the deposition parameters makes it simple to adjust the thin film's deposition rate and thickness across a wide range. (m) The substrate's material, dimensions, and surface profile are essentially unrestricted. (n) Given that the thin films are uniform, closely spaced, and there are no substrate-related side effects, it is believed that reliable fundamental kinetic data are more likely to be obtained on thin film surfaces with extraordinarily well characterized thin films. (o) It is easy to modify the stoichiometry by varying the concentration

of the components in the spray solution. (p) Doping is simple to accomplish. (q) The spray solution comprises soluble salts of the desired compound's component parts.

Disadvantages: The following are some of the primary drawbacks of the SP technique: (a) Oxidation of sulphides during. (b) Difficult to determine the growth temperature. (c) The spray nozzle may become disorganized over a prolonged processing period. (d) The droplet size and the spray nozzle may affect the quality of thin films. (e) Thin film non-uniformity with increased grain size as a result of unpredictable spray droplet size. (f) Solution wastage or the few atoms deposited compared to those provided.

2.1.5. Substrates

(i) Selection of Substrates: The substrate serves as the foundation on which different thin multi layers are deposited and thin film circuits are constructed. In order to ensure that the qualities of the film are unchanged, the substrate chosen for thin film preparation must not suffer any chemical reaction with the material to be deposited. Therefore, the substrate must meet several criteria, including mechanical strength that enables adequate film adhesion to the substrate and a flat, smooth surface that is not just smooth at room temperature but also has defined and consistent electrical, optical, and other properties. Generally, it is reasonable to state that glass, fused mica, beryllium or beryllium oxide-based ceramics, aluminum nitride, and metals are the most often used substrates for polycrystalline films and would suit all requirements. Teflon and other organic materials with low thermal conductivity are employed in specific circumstances. Recently, interest in solar cells mounted on thin, flexible metallic substrates has grown due to the benefits they provide over bulky, brittle glass-based technologies. Blue-star glass slides (75mm×25mm×2mm) are employed as substrates in the current study to produce thin films of Fe₂O₃.

(ii) Cleaning the Substrates: A substrate needs to be thoroughly cleaned for a coating to be effective and adherent. The nature of the chemicals, the nature of the pollutants, and the level of cleanliness required will all affect the best cleaning method. Contaminants from manufacturing processes, human touch, and airborne dust, lint, and oil particles are among those that are anticipated. Cleaning entails dissolving the adsorption bonds between the pollutants and the

substrates while preserving the integrity of the substrate surface. Chemical reaction, salvation, or mechanical scouring are all options for accomplishing this.

The following process is used to clean the glass substrate, making it possible to deposit films free of flaws.

- The substrates are submerged in a heated chromic acid solution for the first two hours. Followed by a de-ionized water wash. After chemical treatment, the substrate is manually cleaned with a cotton pad and a detergent solution.
- Following a distilled water rinse, the substrates are put in an ultrasonic cleaner and stirred for 30 minutes in a detergent and distilled water solution.
- The substrates are then dried in an oven for roughly an hour at 100°C after pre-cleaning with isopropyl alcohol.

2.2 Characterization Techniques

2.2.1 X-ray diffraction (XRD)

X-ray powder diffraction can be used to identify crystalline and non-molecular compounds. Every crystalline solid has unique properties. X-ray powder pattern that could serve as the object's "fingerprint."

The Diffraction Method : An X-ray powder diffraction pattern is a collection of lines or peaks (each with a unique position or intensity, known as a "d-spacing" or "Bragg angle") on a graph paper. The lines' placements are fundamentally predetermined for a particular material and stand in for characteristics of that substance. Depending on the equipment design and the procedure used to prepare the sample, the intensity may differ from sample to sample. To identify the phase of the prepared sample, the X-ray diffraction pattern has to be compared with the reference pattern in the powder diffraction file (JCPDS file). The diffracted X-ray photons' intensity is measured to find crystal forms. The electromagnetic spectrum's region between gamma and ultraviolet rays is where X-rays, which have a wavelength of about 10^{-10} m exist. X-rays are created when high-energy charged particles, such as electrons accelerated through 30000 V, collide with matter. Collisions delay or stop the electrons; some energy they lose is transformed

into electromagnetic radiation. These processes produce "white radiation," or X-rays, with wavelengths that rise over a specific lower limit.

The lower wavelength limit corresponds to the maximum energy X-rays when the kinetic energy of all encountered particles is converted into X-rays. It can be calculated using the formula $\lambda_{\min} = 12400/V$, where V is the accelerating voltage. Most diffraction examinations use X-rays, which are monochromatic and can be produced in various ways. Once again accelerated through, let's say, 30 kV, an electron beam is let to strike the metal target, which is frequently copper. Some of the copper's 1s (K shell) electrons can be ionized by the incident electrons because of their high energy. A vacant 1s level is instantly filled by an electron in an outer orbital (2p or 3p), and the energy produced during the transition is observable as X-ray radiation. Since the transition energies are fixed, a range of distinct X-rays emerges.

The wavelength of the $K\alpha$ transition for copper is 1.5418 Å for the 2p to 1s transition and 1.3922 Å for the 3p to 1s transition of $K\beta$. The $K\alpha$ radiation that results from the K transition is used in diffraction studies since it occurs much more frequently than the $K\beta$ transition. The transition is a doublet because the 2p electron that makes the $K\alpha$ transition has two potential spin states. Moseley's law gives the relationship between wavelengths and the metal's atomic number Z:

$$F^{\frac{1}{2}} = \left(\frac{c}{\lambda}\right)^{1/2} \alpha Z \dots\dots\dots (2.1)$$

Where F is the $K\alpha$ line's frequency; as a result, the wavelength of the $K\alpha$ line gets shorter with increasing atomic number. The prerequisite for X-ray diffraction is that the crystals must be at least 0.05 mm in diameter. Otherwise, the technique of electron diffraction is employed.

Unit cell parameter determination: X-ray powder diffraction can determine the average crystal size in a thin film sample if the average diameter is less than or equal to 200 nm. Defects and dislocations that can appear in crystalline solids can be recognized using a variety of diffraction effects. The locations of the lines in a powder pattern (D-spacing) are determined by the values of unit cell parameters (a, b, c, α , β , γ). These parameters are established using the single-crystal method. For instance, precise unit cell parameters allow for measuring thermal expansion coefficients and indexing complex thin film patterns. Peak intensities decrease and background

radiation increases due to the thermal motion of atoms, which is present in all matter above absolute zero. High temperatures make this more apparent. Metal thermal expansion is measured by high temperature particle diffraction.

X-ray diffraction and crystal: The characteristic $K\alpha$ radiation, with a wavelength of $\lambda = 1.5418 \text{ \AA}$, released by copper, is the standard X-ray wavelength. Atoms or ions operate as secondary point sources and scatter X-rays when a crystal diffracts them.

Bragg's law: Bragg's diffraction method assumes a crystal comprises layers or planes, much like a partially transparent mirror. Nevertheless, the majority of X-rays are transmitted and reflected by subsequent planes. Some of the X-rays are reflected off surfaces with reflection angles equal to the angles of incidence. The angle of incidence, also known as the Bragg angle, and the perpendicular distance between neighboring plane pairs are linked to the distance AC by

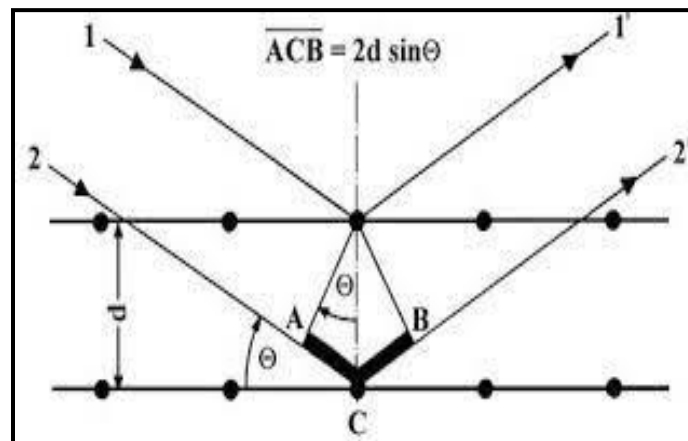


Fig.2.5: X-ray diffraction method

$$AC = CB = d \sin\theta$$

Thus

$$ACB = 2d \sin\theta$$

But

$$ACB = n\lambda$$

Therefore

$$2d \sin\theta = n\lambda \dots\dots\dots (2.2) \quad (\text{Bragg's law})$$

The crystalline phases that are present are identified using the X-ray powder diffraction technique. Demonstrating that the initial reactants have vanished and that undesirable byproducts or intermediates have not been created also demonstrates if the reaction is complete. The

chemical analysis is omitted. Atomic absorption analysis or X-ray fluorescence can analyze the product's chemical composition.

Technical information about the XRD system utilized:

The XRD studies were carried out using an advance X-Ray diffractometer made by Rigaku (ULTIMA-IV). The crystallite size, different phases, and structure of bulk material are all determined using the X-ray powder diffraction technique. In order to determine the different phases and corresponding structure of the material in the sintered powder or pellet, the XRD yields 'd' values. Additionally, XRD is used to determine the particle size. The X-ray diffraction patterns of all the materials were recorded at room temperature (RT), not at working temperature. The following are the X-ray parameters used to characterize sensor material:

Target: Cu, the wavelength of K_{α} line ($\lambda = 1.542 \text{ \AA}$),

Angle: $2\theta = 20^{\circ} - 80^{\circ}$,

Current: 30 mA,

Voltage: 30 kV,

Max rate: 5×10^3 counts/sec,

Slit width: 0.3 mm,

Time constant: 2min.

Using the Bragg law, the lattice's inter-planer spacing, or d, is determined:

$$n\lambda = 2d\sin\theta,$$

where n is the order of diffraction (for the present investigation, $n = 1$) and λ is the wavelength of Cu K_{α} . The standard data (JCPDS data files) are compared to the experimental d values.

The X-ray diffraction technique is an effective method for characterizing the structural characteristics of materials in bulk or thin film. The structural characteristics of the films were examined in the current study utilizing XRD measurements. In Fig. 2.6, an image of an X-ray diffractometer is displayed. The phase composition can be determined using the XRD technique.

In X-ray diffractometry, the slit of an X-ray tube emits characteristic radiations that fall on the films and are picked up by a slit at the counter. In order to satisfy the requirement of parafocusing, the two slits and the specimen are situated at the edge of a circle. The pattern is typical of the crystal structure; it essentially serves as fingerprint by which material can be identified. Comparing the diffraction peaks with the standard JCPDS data, it is feasible to identify unknown chemicals, measure the grain size, and know the effect of temperature on grain size and crystallinity.



Fig. 2.6: Photograph of X-ray diffractometer.

One very important use of XRD when dealing with nanocrystals is to estimate crystal dimensions through the Scherrer's relationship [77]:

$$\text{Crystal diameter } D = \frac{0.9 \lambda}{\beta \cos \theta} \text{----- (2.3)}$$

where λ is the X-ray wavelength (1.5418 Å for CuK α commonly used source), θ is the peak position and β is the peak full width at half maximum (FWHM) in radians is the width of the main peak of the phase measured at the half of the height of the peak as shown in fig.2.7.

The texture coefficient is a quantitative measure used to estimate the preferred orientation of the thin films, It is determined using the following formula [78].

$$\text{Texture coefficient } TC_{(hkl)} = \frac{I_{(hkl)}}{I_{0(hkl)}} \left[\frac{1}{n} \sum_1^n \frac{I_{(hkl)}}{I_{0(hkl)}} \right]^{-1} \text{-----} (2.4)$$

where I and I₀ are experimental and standard (JCPDS) peak intensities.

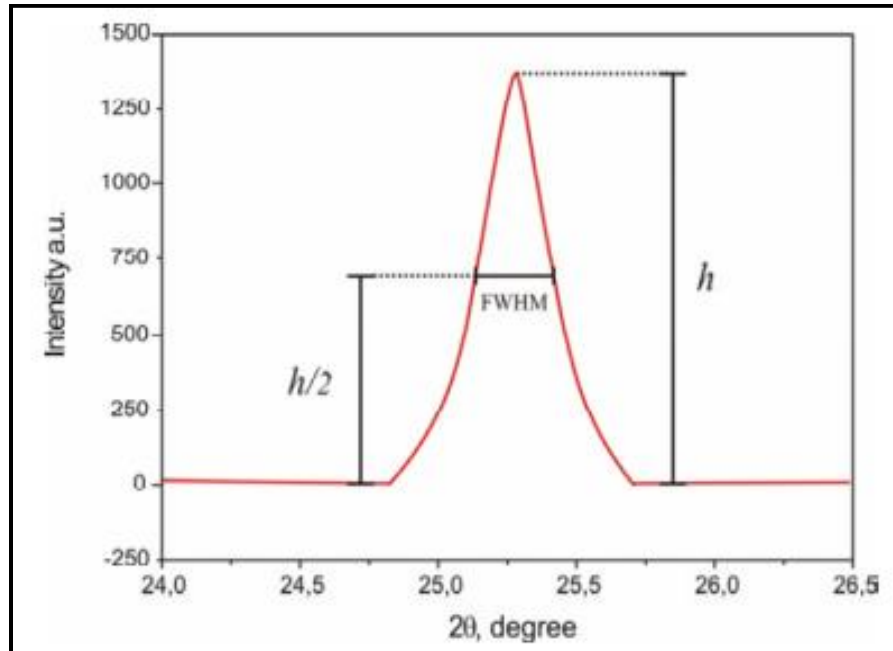


Fig. 2.7: FWHM measured in a typical peak of phase in a material XRD pattern

Deviations from the ideal crystalline lattice cause the film's micro-strain, and it might be produced due to dislocations, vacancies, residual stress, grain boundaries, and other defects in the crystalline material. Micro-strain in the films can be calculated using the Williamson-Hall equation [79].

$$\text{Micro-strain}(\epsilon) = \frac{\beta \cos \theta}{4} \text{-----}(2.5)$$

The dislocation density in the films measures the number of dislocations present in the crystalline material per unit volume. The following relation can be used to calculate the dislocation density in crystalline thin films [80].

$$\text{Dislocation density } (\delta) = \frac{1}{D^2} \text{----- (2.6)}$$

The number of crystallites per unit area can be determined with the below equation [81]. It relies upon structural specifications such as equispaced crystallites and the degree of the agglomeration of the deposited films.

$$\text{Number of crystallites per unit area} = \frac{\text{Thickness of the film}}{(\text{Crystallite size})^3} \text{----- (2.7)}$$

Limitations:

- i) A trace of doping substance cannot be identified.
- ii) Not all characteristic planes can be seen for small amounts of material. A popular program for simplifying the examination of X-ray diffraction patterns is called X Powder. FWHM, d-spacing, and grain size were measured using the X Powder software.

2.2.2 Scanning Electron Microscopy (SEM)

Scanning electron microscopy is a highly adaptable technology that may offer structural details at different magnification ratios. Scanning electron microscopy (SEM) is a helpful supplement to optical microscopy when examining the texture, topography, and surface features of powders or solid objects [82]. Features as small as tens of micrometers can be seen using SEM. Due to their depth of focus, SEM equipment produces unmistakably three-dimensional images. Transmission and reflection electron microscopes are the two varieties. We used a tool for reflection. This sample eliminates the need for special sample preparation methods and does not have a problem with sample thickness. It is frequently necessary to coat the sample with a thin layer of metal in order to prevent the accumulation of charge on its surface, especially if the sample is a bad electric conductor. The main tool for reflection is SEM. It covers the magnification range between the lower resolution limit of optical microscopy ($\sim 1 \mu\text{m}$) and the greatest practical working limit of TEM ($\sim 0.1 \mu\text{m}$). SEM has a much wider application window, from $\sim 10^{-2}$ to $10^2 \mu\text{m}$.

Operation mode: A sample is placed in a microscope and is subjected to high energy electron bombardment, among other procedures, to produce X-rays. The distinctive emission spectra of these X-rays serve as a representation of the elements in the sample. By examining the energy

(ED) or wavelength (wavelength dispersive, WD) of the emitted X-rays, the element that is present can be identified. The focus of an electron gun's beam of electrons in a scanning electron microscope is a small area of the sample's surface that is 50 to 100 Å in diameter. As the sample is being scanned, the beam passes over it again. The sample emits both X-rays and secondary electrons; the former are used for chemical analysis, and the latter are used to create an image of the sample surface displayed on a screen. An issue with SEM equipment is that its lower resolution limit is 100 Å.

Details of SEM and EDAX systems

A scanning electron microscope (SEM) (FEI- Apreo LoVac) and an energy dispersive spectrometer were used to analyze the films' microstructure and chemical composition. Along with the elemental analysis of the chosen region/features and the distribution of the chosen elements, the specimen photograph is also displayed. It is an effective analytical method that provides X-ray distribution pictures, line scans, and point analyses of the trace components of micro-volumes. The Si (Li) detector can detect light elements beginning with Boron (5) owing to its super ultra thin window and 133eV resolution evaluated at MnK, 1000 CPS, and time content 100 μm. The complete sample was first subjected to a SEM scan before the elements were discovered using EDAX (the device above also contains software that may provide the ratio of anticipated elements' compounds).

A representation of the SEM and EDAX is shown in Fig. 2.8. SEM is a surface analysis technique that precisely focuses an electron beam on the sample surface. Since the secondary electrons created by the electron beam heavily depend on the topology of the surface, they are used for image formation. The grain size and distribution may be determined using the SEM images. In addition, SEM can be used to characterize the morphology of the particle, including its shape, porosity, and surface structure. However, a significant disadvantage of SEM is its inability to identify granules smaller than 20 nm due to its poor resolution. The main components of an electron microscope are an electron gun, magneto static lenses that serve as condensers, objectives, and projectors, a fluorescence screen, an optical camera unit, and a built-in high-voltage stabilized power supply.

The SEM device can scan a chosen specimen area using a condensing lens electron beam. An intermediate lens further magnifies the image created by the objective lens before it is finally projected onto a fluorescent screen. The most common models used include emitting, reflecting, adsorptive, transmission, X-ray, cathode luminescence, and beam induced conductivity. In the current investigation, the FEI- Apreo LoVac model was used.

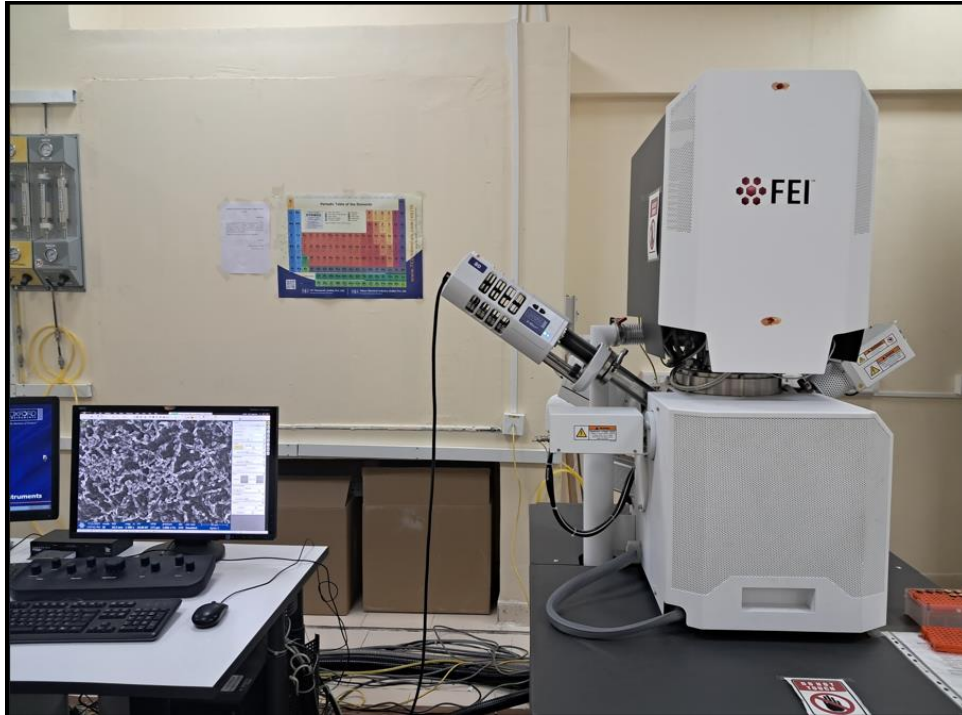


Fig. 2.8: Photograph of SEM and EDAX.

Sample nature : i) Thin film

ii) Powder

Uses: i) Used to analyze surface morphology, grain size, and microstructure.

ii) Comparable magnification resolution.

Limitations: i) The sample's inside cannot be studied.

ii) Researching the microstructure of non conducting materials is challenging.

EDAX, a very useful extra feature of some SEM instruments, provides an elemental analysis of the sample composition.

2.2.3 Energy-Dispersive Analysis by X-rays (EDAX)

Energy-dispersive analysis by X-rays (EDAX) is an analytical technique used for the elemental analysis or chemical characterization of a substance. This element is included with the scanning electron microscope (SEM). It relies on how an X-ray source interacts with the substance being studied. The core premise is that each element has a unique atomic structure that allows for a unique collection of peaks on its X-ray spectrum, which makes it capable of characterizing objects. To cause the emission of characteristic X-rays from the object being examined, a high-energy stream of charged particles, such as electrons or protons, or an X-ray beam is directed into it. When an atom's ground state electrons, sometimes referred to as unexcited electrons, are restricted to particular energy levels known as electron shells, the atom is said to be at rest. An electron in an inner shell may be excited by the incident beam, which would cause it to be ejected from the shell and leave an electron hole in its place. The energy differential between the lower-energy inner shell and the higher-energy outer shell may be released as an X-ray when an electron from the outer, higher-energy shell fills the hole. The quantity and energy of X-rays emitted from a specimen can be measured using an energy-dispersive spectrometer. The elemental composition of the specimen may be determined because the energy of the X-rays is indicative of both the energy difference between the two shells and the atomic structure of the element from which they were released. A lithium-drifting Si-diode held at liquid nitrogen temperature serves as the X-ray detector.

Nature of Sample: i) Thin film

ii) Powder

Uses: i) Elemental analysis

Limitations: i) Light elements can't be precisely measured because they have a low atomic number.

2.2.4 Raman Spectroscopy

Raman spectroscopy is a vibrational spectroscopic method for detecting both organic and inorganic molecules and determining the crystallinity of solids. Raman first described the Raman Effect in 1928 [83], the foundation of Raman spectroscopy. An incident photon emits a phonon (phonon emission), a lower energy photon that gains energy from the lattice. The down conversion-induced frequency shift is known as Stokes-shifted scattering. Anti-stokes-shifted

scattering happens when a photon absorbs a phonon and re-emerges with more energy. The anti-Stokes mode is significantly weaker than the Stokes mode because Stokes-mode scattering occurs more frequently. When using Raman spectroscopy, a beam of light known as the pump is impacts the substance.

The stimulating photon in Raman (inelastic) scattering has less energy as it departs the molecule than when it entered. After the energy is transferred to the molecule, the energy due to inelastic scattering is lost for the vibrations of the molecular bonds.

$$\Delta E = h\nu_{\text{vib}} \text{ ----- (2.8)}$$

where ν_{vib} is the vibrational frequency of the vibrating molecular bond and ΔE is the energy difference. The total energy of the input photon must be conserved. Therefore, the Raman scattered photon has less energy and is longer in wavelength. Monitoring these inelastically scattered photons will provide information regarding the molecule's vibrations, which are nothing more than a Raman spectrum. where

$$E_{\text{Raman}} = h(\nu - \nu_{\text{vib}}) \text{ ----- (2.9)}$$

A photodetector picks up the Raman-shifted wavelengths, and the weakly scattered light or signal is then processed through a double monochromator to remove the Rayleigh-shifted light. A laser lights the material using a standard microscope in the Raman microprobe. In order to prevent specimen breakdown and sample heating, laser power is typically kept below 5mW. The pump must be a bright, monochromatic source to be distinguished from the signal. Weak signals against the strong background of scattered pump radiation make detection challenging. The signal-to-noise ratio is improved if the Raman radiation can be detected at a right angle to the pump beam. The interference brought on by fluorescence, whether from contaminants or the material itself, is a significant drawback of Raman spectroscopy. Raman spectroscopy and Fourier Transform Infrared Spectroscopy (FTIR) are used to solve the fluorescence background issue. The crystal structure is highly sensitive to Raman measurements. For instance, differing

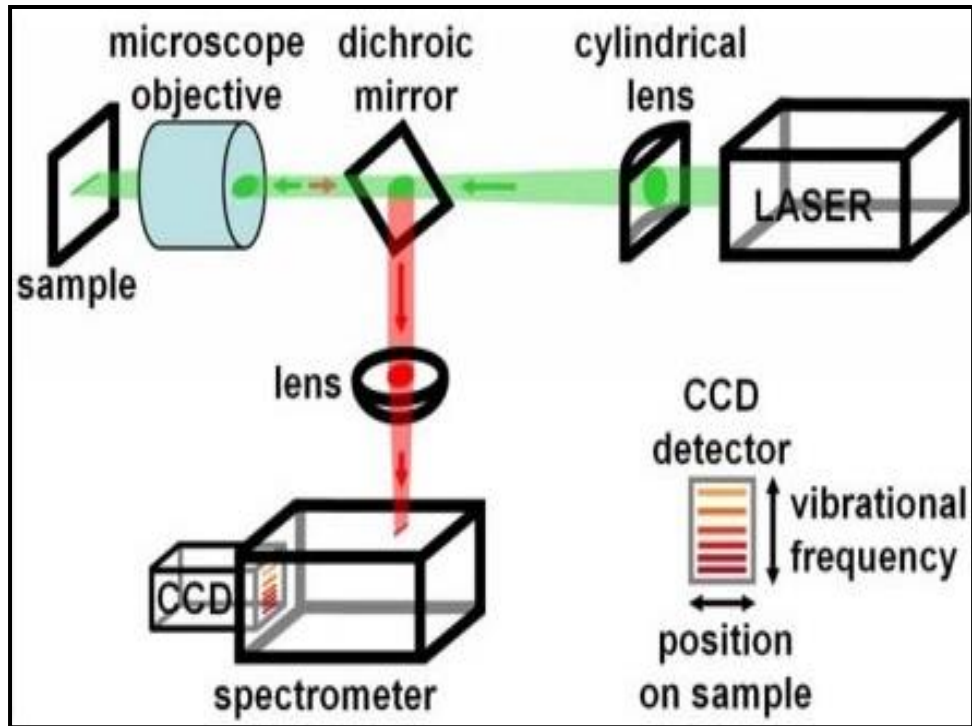


Fig.2.9: Schematic illustration of a Raman spectrometer



Fig.2.10: Photograph of a Raman spectrometer

crystal orientations result in marginally varied Raman shifts. The frequencies are also altered because of the stress and strain on the thin layer.

Renishaw's Raman analysis was carried out in the current study at room temperature. Spectral resolution of 1 cm^{-1} in a Via mini Raman spectrometer operating in the 100 to 1000 cm^{-1} wave number range. A 488 nm argon ion laser was employed as the excitation source. The schematic illustration of a Raman spectrometer is shown in Figure 2.9.

2.2.5 X-ray Photoelectron Spectroscopy (XPS)

In the X-ray photoelectron spectroscopy (XPS) or Electron Spectroscopy for Chemical Analysis (ESCA) process, a sample surface is exposed to X-rays. The elements that make up the surface, its composition, and chemical bonding state are then examined by measuring the kinetic energy of the photoelectrons are emitted from the surface [84]. Generally, an XPS device using Al $K\alpha$ rays may learn about elements a few nm away from the sample surface.

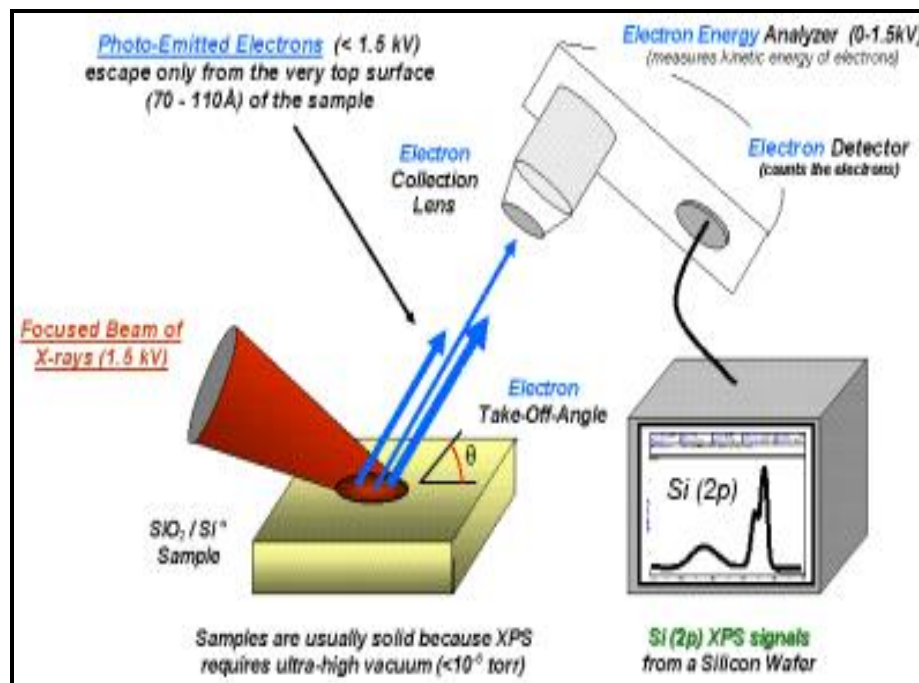


Fig.2.11: Schematic illustration of a X-ray Photoelectron Spectroscopy

Another benefit of XPS is the relative ease with which the state of chemical bonds can be identified because the change in bond energy (chemical shift) brought on by the electron state

surrounding the atoms to be analyzed, such as atomic valence charges and interatomic distances, tends to be greater than the chemical shift observed in atomic emission spectroscopy (AES).

The energy of the X-rays must exceed a threshold energy known as the surface work function in order to excite an electron from its valence orbital to the continuum during irradiation. It was shown that this threshold energy is the energy needed to excite an electron from its valence orbital to the surface atoms. For electrons released from lower orbital, the electron's binding energy must also be overcome, resulting in a further reduction in the kinetic energy of the expelled electron.



Fig.2.12: Photograph of X-ray Photoelectron Spectroscopy

Therefore, the electron's binding energy is equal to the energy of incident X-rays, less the work function, and less the kinetic energy of the expelled electron. The kinetic energy of the ejected photoelectrons is measured by an analyzer in XPS. The measured kinetic energy of an electron is changed into a binding energy for that electron's specific atomic orbital. Because each element has a unique collection of energy levels, each element also has a unique set of binding energies for the electrons in these levels. The following equations describe the binding energy.

$$E_B = h\nu - \phi - E_k \text{ ----- (2.10)}$$

Where E_B =Electron binding energy

h =Planck's constant

ν =Frequency of incident X-rays

ϕ =Surface work function

E_k =Kinetic energy of electron

Minimal variations in the oxidation state and atomic bonding of an element cause small shifts in its core energy levels, which in turn cause small variations in the locations of the corresponding photoelectron peaks. These peak fluctuations, usually in the range of 1 to 5 eV, are detectable by most XPS spectrometers with energy resolutions of 0.1 to 0.2 eV. The XPS photoelectron peaks carry the name of the core level from which the electron was released. The XPS method only looks at a sample's outer 1–10 nm since released photoelectrons lose kinetic energy as they move through a sample. The only photoelectrons with a short enough escape path to reach the detector are those produced in the sample's outermost layers.

2.2.6 Atomic force microscopy (AFM)

The image of the AFM is displayed in Fig. 2.13. In the metal oxide studies, the AFM is being used to address issues with processes and materials. AFM pictures provide exceptional clarity for important information about surface characteristics [85]. Any stiff surface can be examined using the AFM, whether it is in the air or submerged in a liquid. Small or significant discrepancies between smooth surfaces are strikingly displayed. Even single atoms that were previously unseen can be resolved using the AFM. The AFM can analyze a field of view bigger than 125 microns, allowing comparison with other data, such as features visible to the naked eye using a light microscope. Since the AFM's vertical range is more than 5 microns, it can also study rough surfaces. In traditional contact mode AFM, a topographical map of the sample's surface is produced by simply dragging the probe tip across the surface. Using a piezoelectric crystal to oscillate the cantilever assembly at or near its resonance frequency, classic tape mode AFM imaging is performed in free air.

In the current experiment, several areas of the film surface were probed using contact mode AFM using an AFM Nano scope (Model-TNC) digital equipment with a silicon nitride cantilever.

Nature of Sample: i) Thin film

ii) Powder

Uses: i) To obtain information about surface morphology.

ii) To assess the film material's surface roughness.

Limitations: When using AFM in contact mode, it is possible to significantly damage samples or shred surfaces.

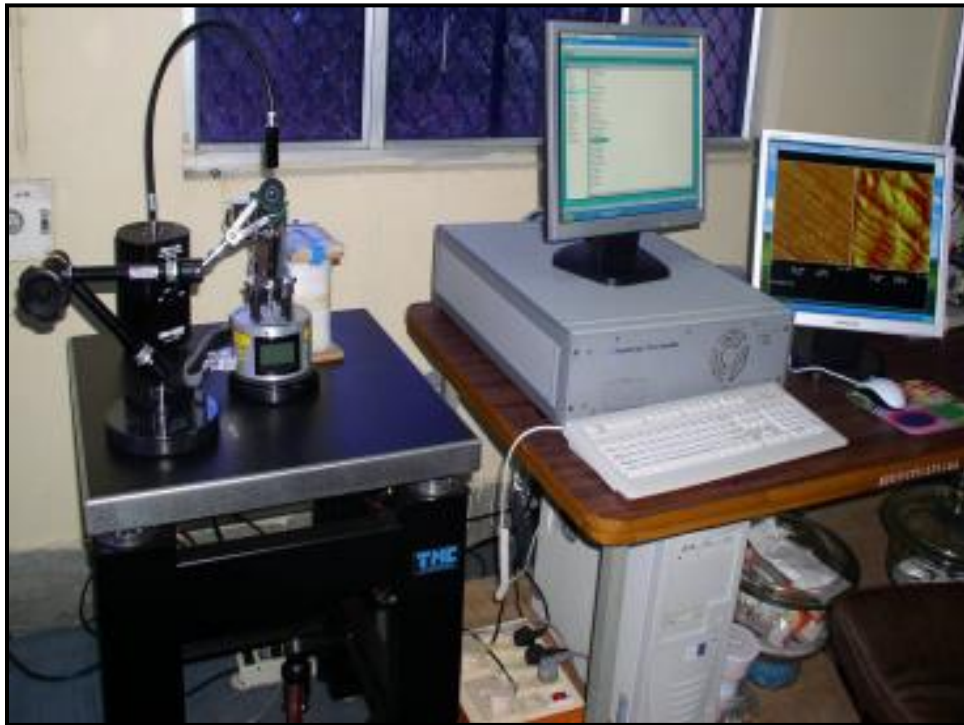


Fig. 2.13: Photograph of AFM.

2.2.7 Ultraviolet–Visible spectroscopy

Absorption spectroscopy or reflectance spectroscopy in the ultraviolet-visible spectral region are referred to as ultraviolet-visible spectroscopy or ultraviolet-visible spectrophotometer (UV-Vis). In other words, it makes use of light that is visible and close by (near-UV and near-infrared (NIR)) in wavelength. The visual absorption or reflectance of the substances involved

directly impacts how those colors are perceived. Molecules go through electronic transitions in this area of the electromagnetic spectrum. Fluorescence spectroscopy deals with transitions from the excited state to the ground state. In contrast, absorption measures transition from the ground state to the excited state, making it a complementary approach to fluorescence spectroscopy.

Principle of Ultraviolet-Visible Absorption

In order to excite their electrons to higher anti-bonding molecular orbital, molecules with π -electrons or non-bonding electrons (n-electrons) can absorb energy from ultraviolet or visible light. The longer the wavelength of light it can absorb, the more easily the electrons can be activated. For the quantitative determination of many analyte, including transition metal ions, highly conjugated organic compounds, and biological macromolecules, UV-Vis spectroscopy is frequently utilized in analytical chemistry. A spectrometer's spectral bandwidth indicates how monochromatic the light is. If this bandwidth is comparable to the range of the absorption properties, the measured extinction coefficient will vary. In reference measurements, the bandwidth of the instrument is typically maintained below the widths of the spectral lines. It may be necessary to test and confirm whether the bandwidth is narrow enough when measuring new material. When the spectral bandwidth is reduced, it will take longer to measure for the same signal-to-noise ratio because less energy will be transferred to the detector.

Ultraviolet-visible spectrophotometer

A UV-Vis spectrophotometer is the device used in ultraviolet-visible spectroscopy. It calculates the amount of light that passes through a sample and contrasts it with the amount of light that comes into contact with the sample. The transmittance, also known as the ratio, is typically given as a percentage (% T). The transmittance is the foundation for the absorbance: Reflectance measurements can also be made using the UV-visible spectrophotometer. Here, a spectrophotometer measures the amount of light reflected from the sample and contrasts it with the amount of light reflected from a reference object (such a white tile). Reflectance, also known as the ratio, is typically given as a percentage (% R).

The basic parts of a spectrophotometer are a light source, a holder for the sample, a diffraction grating in a monochromator or a prism to separate the different wavelengths of light, and a detector. Typically, tungsten filaments (300–2500 nm), deuterium arc lamps (190-400 nm),

xenon arc lamps (160–2,000 nm), or, more recently, light emitting diodes (LED) for visible wavelengths are used to produce the radiation. Charge-coupled devices (CCDs), photomultiplier tubes, photodiodes, or arrays are frequently used as detectors. Scanning monochromators, which filter the light so that only light of a single wavelength reaches the detector at a time, are employed with single photodiode detectors and photomultiplier tubes. The intensity of each wavelength can be determined as a function of wavelength by moving the diffraction grating with the scanning monochromator to "step-through" each wavelength. Fixed monochromators are used by both CCDs and photodiode arrays. These devices may simultaneously gather light from various wavelengths on various pixels or groups of pixels since they are made up of several detectors arranged in one or two-dimensional arrays.

There are two types of spectrophotometers: single-beam and double-beam. In a single-beam instrument, the sample must be taken out to measure all of the light entering the sample cell. Although it was the first design, it is still widely used in research and teaching labs. Before it reaches the sample, the light is divided into two beams in a double-beam instrument. The reference beam is one beam, and the sample beam is the other beam. The ratio of the two beam intensities is displayed, with the reference beam intensity assumed to be 100% transmission. Some double-beam instruments with two detectors (photodiodes) monitor the sample beam and reference beam concurrently. In some devices, a beam chopper blocks one beam at a time while the two beams pass through it. The detector alternates between monitoring the sample and reference beams in tandem with the chopper over time. One or more dark periods may also be a part of the chopper cycle. By subtracting the intensity obtained in the dark prior to taking the ratio, the observed beam intensities in this case can be modified.

The most common types of samples for UV-Vis spectrophotometer are liquids, while it is also possible to determine the absorbance of gases and even solids. Typically, samples are put in a cuvette, which is a clear cell. Cuvettes frequently have an internal width of 1 cm and are typically rectangular in shape. In the Beer-Lambert law, this width is converted into the path length. In some equipment, test tubes can also serve as cuvettes. Radiation must be able to pass over the targeted spectral region regardless of the sample container type. High grade fused silica or quartz glass cuvettes are the most extensively used since they are transparent throughout the UV, visible, and near infrared spectrums. Cuvettes made of glass and plastic are also widely

used, although they are only usable for visible wavelengths because glass and the majority of plastics absorb UV light. A more advanced spectrophotometer can frequently directly generate full absorption spectrum at all relevant wavelengths. In less complex instruments, the absorption is measured one wavelength at a time, and the operator subsequently compiles the results into a spectrum. The extinction coefficient (ϵ) can be calculated as a function of wavelength by eliminating the concentration dependence.

Optical spectroscopy is widely used to verify that thin films have the band gap that the deposited semiconductor predicted. Optical spectroscopy is unquestionably a quick and simple method to determine crystal size because many semiconductor colloids and films have found band gap size correlations. Thin films are often nano crystalline, and the most noticeable effect of very small crystal size is the increasing band gap due to size quantization, absorption (or transmission).

While measuring transmission, spectrophotometers do not measure absorption. Absorbance, A , the standard unit of measurement for absorption, is defined as [86]:



Fig. 2.14: Photograph of UV-visible spectrophotometer.

$$A = \log_{10} I_0/I \text{ ----- (2.11)}$$

where, I is the intensity of the transmitted light and I_0 that of the incident light.

The transmission T is $T = I/I_0$

By translating the transmission into absorbance using these equations, the spectrophotometer measures the transmission and performs an absorption measurement. Using a Jasco (UV-650) spectrophotometer, the optical absorption investigations of the films were performed. In Fig. 2.14, a picture of the UV-spectrophotometer is displayed.

Nature of Sample: i) Thin film

ii) Powder

iii) Liquid

Uses: To find out the material's optical band gap and the type of transition (direct or indirect).

Investigating the transmission.

Limitations: Because it is challenging to examine the microstructure of non-conducting substances, it is assumed that reflectance, R , is zero.

2.2.8 Thickness Measurement

Thin films can be characterized in terms of their structural, morphological, elemental, spectral, optical, photoluminescence, and electrical properties, and it has been shown that these properties rely on thickness [87]. Reproducible characterization is only possible when the thin film thickness is kept constant. The thickness of the sprayed layer depends on several factors, including the volume and concentration of the precursor solution used, the substrate's temperature, the distance between the spray nozzle and the substrate, and others. There are numerous ways to measure thin film thickness, some of which include:

- Profilometry
- Ellipsometry
- Weight Gain method
- Cross-section visualization of the thin film with SEM.

Similar to AFM is a topographical method known as stylus profilometry, which measures the height of a step made by masking during deposition from the substrate surface to the thin film surface. Stylus has a resolution of less than 0.2 microns and measures heights more than 100 Å. The surface is in touch with a sharp point frequently made of diamond and horizontally scanned. Its radius varies between 0.1 μm and 50 μm. The measuring sensor converts this height difference into an electrical signal whenever there is a change in the vertical direction of the scan, which causes the tip to move up or down in height. Profilometry precisely studies the thin film thickness while recording the tip location and height in time or space increments during the scan. The thickness of the thin film was measured in the current work using weight growth and cross section visualization of the thin film.

2.3 Gas sensing system

For testing the sensing capabilities of the sensors, the present study utilized the gas sensing system and a schematic illustration of the experimental setup for gas sensors, as shown in Fig. 2.15. The electrical feeds are connected to the base plate. A sample being tested can be mounted on the base plate, which has a heater fixed to it. A mounted Cr-Al thermocouple is used to measure the operating temperature. An indication of temperature is linked to the thermocouple's output. One of the openings in the gas chamber has a fitted gas inlet valve. A known volume of a test gas is injected into the static system using a gas-injecting syringe to achieve the desired gas concentration. A constant voltage is applied to the sensor, and an electrometer measures the resistance.

Sensing characterization was performed using a static gas sensing technique. A constructed testing chamber with a 10-litre capacity was used to study the sensing characteristics of the samples toward various volatile organic compounds (VOCs). Using a tiny syringe, the chamber was filled with the desired concentration of the target. The operational temperature was adjusted and controlled using a digital thermostat and a tiny heater. A highly conducting silver paste created ohmic electrical contacts on the film. The sensing response was recorded by utilizing an electrometer (6517B, Keithley) to measure the change in electrical resistance with regard to dry air. The airtight chamber (capacity = 10 liters) was filled with ambient air at atmospheric pressure before a pre-calculated volume of the test gas was injected into it to obtain the desired gas concentration inside the test chamber.

Sensitivity (S): The sensitivity of a thin film is measured by how much its resistance changes. It is the difference between the film's resistance in an air environment of air at the chosen operating temperature and the film's resistance after exposure to the target gas. The target gas concentration is determined by static liquid gas distribution technique using the following formula [88].

$$C_{\text{ppm}} = \frac{22.4 \times V1 \times \rho \times \phi}{V2 \times M} \quad \text{----- (2.12)}$$

Where, C_{ppm} is concentration, ρ is density (g/mL), $V1$ is volume (μL), ϕ is volume fraction, M is molecular weight (g/mol) of the target gas and $V2$ is volume of the chamber (L).

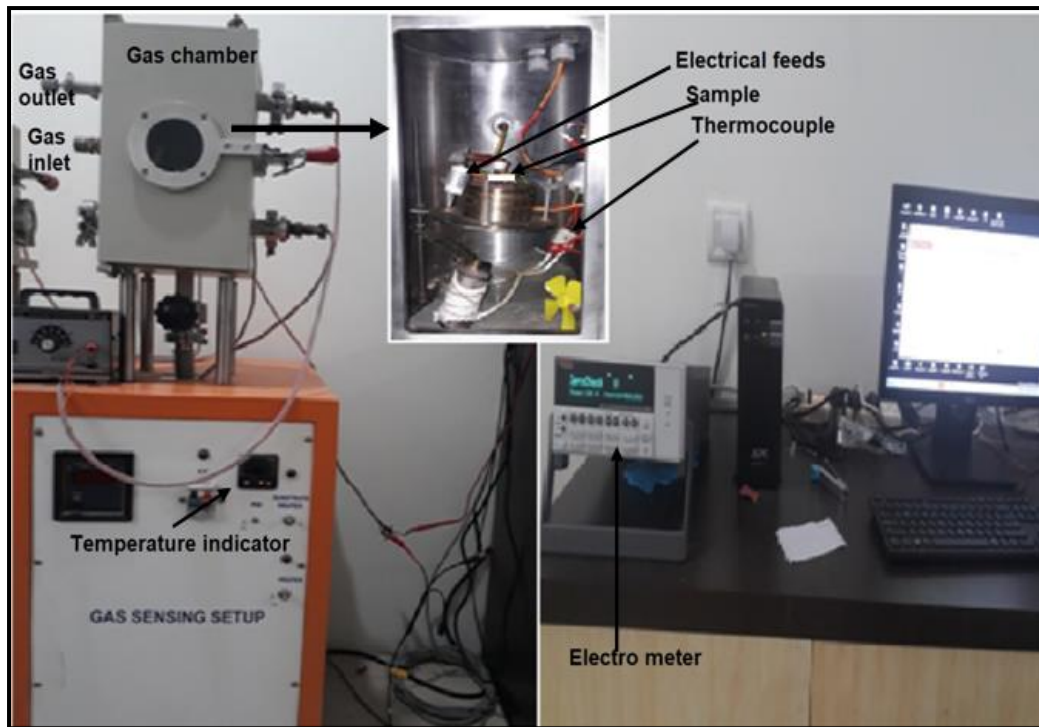


Fig. 2.15: Photograph of the gas sensing system.

The working principle of a gas sensor predominately depends on parameters such as sensitivity, selectivity, and stability. The sensitivity of the sensor element towards reducing gases is measured using the following relation [89].

$$\text{Sensitivity} = \frac{R_a}{R_g} \text{ or } \frac{R_a - R_g}{R_g} \times \% \quad (R_a > R_g) \quad \text{----- (2.13)}$$

3.0 Introduction:

In recent years, several types of gases such as toxic, harmful, explosive and flammable gases have been used in different areas detrimental to health and the environment. It becomes essential to monitor and control these gases as there is a high risk to human lives and property [90]. Across the globe, now researchers put more effort into highly sensitive, fast responsive and low-cost gas sensors to detect harmful and flammable gases that protect society's life [91]. Typically, various materials have been reported for the use in metal oxide gas sensors, such as TiO₂, ZnO, CuO, In₂O₃, SnO₂, Co₃O₄, WO₃, Fe₂O₃, V₂O₅ etc.. Among them, Fe₂O₃ is much more demanding for practical use in gas sensors due to its stability, sensitivity and sensitivity towards various toxic gases [92-98].

NH₃ is an explosive, flammable, colourless transparent liquid. It is extremely toxic, and can severely affect the blood and nervous system of the human body exposure to ammonia vapour leads to dizziness, headache, nausea, blurred vision and even death, depending on the exposure level [99]. Ammonia is widely used in drugs, dyes, organic synthesis, automobiles and industries. As per the recommendations of the OSHA (Occupational Safety and Health Administration), the exposure restriction of ammonia to human beings is 35 ppm for 10 minutes and 25 ppm for 8 hours. Compared to formaldehyde, toluene, ethanol and methanol, ammonia is a less studied compound. There is also a necessity of an ammonia gas sensor to be developed which is to be widely used in poultry, aquaculture and industries [100, 101]. The presently existing ammonia sensors work at high operating temperatures, expensive and maintenance. This motivates us to develop a cost effective ammonia gas sensor which is working at ambient conditions.

Over the last few decades, nano structured metal oxide-based sensors have been attracting much curiosity owing to their excellent sensitivity, fast response towards harmful and exhaust gases in areas such as industrial production, food processing, environmental monitoring, medical diagnosis, domestic safety in addition to their easy design, uncomplicated construction, low power, high compatibility and economical [92-99]. Metal oxide-based gas sensors are meeting the needs of researchers in sensor development, and they are considerably demanding due to the broad range of applications. Due to increasing requirements for efficient and suitable gas sensors with good selectivity, sensitivity, and accuracy, relentless attempts are being made to find appropriate materials.

Iron oxide gas sensors are giving much interest among all-metal oxide-based materials as these materials are fulfilling the requirements of a perfect sensor [92]. Iron (Fe) has many phases with oxides. However, the most used oxides are maghemite (γ -Fe₂O₃), magnetite (Fe₃O₄), and hematite (α -Fe₂O₃) [102,103]. They can be prepared in pure form and mixed form and doped structures as they are available in the crust of the earth. While these oxides have different optical, electrical and chemical properties, they can be changed by adding Ni, Zn, Mg, Mn, Al, Cu, Ca, Pd etc. By doping, these materials it has been proved that the sensor performance may change dramatically [104,105].

The gas sensing efficiency and electric properties of a material depends on its structural and micro structural properties and its method of preparation. Recently several techniques have been reported to deposit iron oxide-based thin films such as spin coating, atomic layer deposition, hydrothermal evaporation, RF/DC sputtering, hydrothermal, chemical vapour deposition, spray pyrolysis. However, spin coating, chemical vapour deposition (CVD) and spray pyrolysis are more flexible and inexpensive. Since spray pyrolysis is one of the simple and cost-effective technique to prepare iron oxide thin films various research groups suggested and reported that the preparation of iron oxide-based thin films by this technique is environmentally safe, and there is no need of high vacuum [106-108].

The present work represents the synthesis of α -Fe₂O₃ thin films utilizing the spray pyrolysis technique to study their structural, optical properties and response of the gas sensor to ammonia gas for different concentrations at an operating temperature of 27°C.

3.1 Experimental techniques

3.1.1 Preparation of α -Fe₂O₃ thin films

In the present work α -Fe₂O₃ thin films were deposited on glass (blue star) substrates with the low cost spray pyrolysis technique at various deposition (substrate) temperatures. The starting material Fe(NO₃)₃ 9H₂O procured from Sigma Aldrich (India) was dissolved in 40 ml deionized water to attain 0.1M. of precursor for the deposition process. Prior to the deposition process the glass substrate is cleaned with liquid soap water and then in an ultrasonic bath for 15 minutes. Finally washed with distilled water and dried in an oven to make moisture free substrates. The solution was sprayed on a pre-heated glass substrate with a rate of flow 1ml/minute for 10 minutes at various deposition temperatures from 375 °C – 425 °C using air as carrier gas.

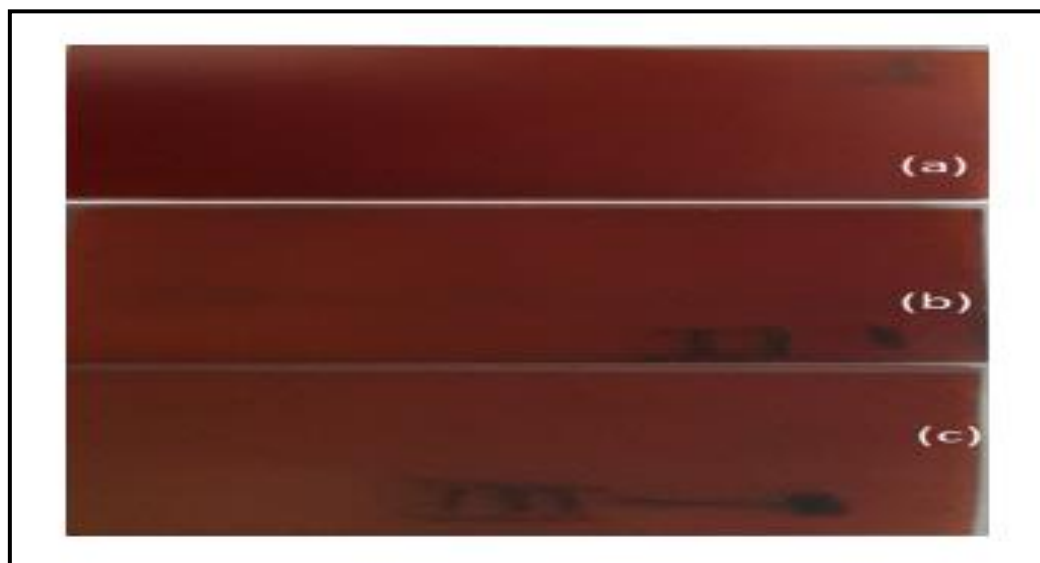


Fig.3.1: Images of deposited $\alpha\text{-Fe}_2\text{O}_3$ films at various substrate temperatures on a glass substrate (a) 375 °C, (b) 400 °C, (c) 425 °C

Table 3.1. Deposition parameters of $\alpha\text{-Fe}_2\text{O}_3$ thin films

Deposition parameter	Values
Nozzle to substrate distance	25cm
Temperature	375°C, 400°C, 425°C
Flow rate	1 ml/min
Spray time	10min
Concentration of solution	0.1M
Volume of solution	40ml
Precursor	$\text{Fe}(\text{NO}_3)_3 \cdot 9\text{H}_2\text{O}$ (Sigma Aldrich, India)
Compressed air pressure	2.94 Bar
Solvent	De-ionized water
Substrate	Glass (Blue star, India)

The images of deposited films are shown in fig.3.1 and the deposition parameters are given in table 3.1.

α -Fe₂O₃ thin films were allowed to cool after the deposition to normal conditions. Characterization of thin films for structural properties was made using Rigaku (ULTIMA-IV) X-ray diffractometer with Cu-K α (0.154nm) as a source of energy in the scan range of 20°-80° with a scan speed of 1°/min. Topographical morphology and elemental information of deposited thin films were determined using a field emission scanning electron microscope attached with a standard EDS system. Atomic force microscopy analyses were carried out using AFM, Bruker in tapping mode with 0.5 Hz frequency. The oxidation states of the Fe₂O₃ thin films were confirmed by X-ray photoelectron spectroscopy (Thermo Fisher Scientific, U.K). The optical properties of the films were studied using a double beam UV-Vis spectrophotometer (Jasco V650) with a single monochromator in the wavelength measurement range of 300nm to 800nm. Gas sensing characterization of deposited films were carried with an indigenous made gas sensing system in static mode with Keithley (6517B) electrometer, which is interfaced with a personal computer.

3.1.2 Thickness measurement

The weight difference approach was used to determine the film's thickness after being created using the spray pyrolysis procedure. Before the film was deposited, the substrate was weighed. The film was dried and sintered after being deposited on the substrate, and its weight was once more measured. The weight difference, material density, and area of the film were utilized to calculate the film's thickness. [109]

$$\text{The thickness of the film, } t = M/(A \times \rho) \dots\dots\dots(3.1)$$

Where M is the difference between the mass of the substrate after and before deposition of the film, A is the area of the film deposited in cm² and ρ is the density of the material deposited in gmcm⁻³. Observed thickness of the films at various temperatures is given in table 3.2.

Table 3.2: Thickness of α -Fe₂O₃ thin films

S.No	Temperature (°C)	Film thickness (nm)
1	375	386
2	400	420
3	425	345

3.2 Results and discussion

3.2.1 X-ray diffraction

X-ray diffraction (XRD) is a reliable technique to investigate the crystalline nature of the iron oxide thin films which were deposited at different substrate temperatures. XRD analysis will provide excellent and sufficient information about the samples if the data is collected continuously at a slow rate of the scan. Fig.3.2. depicts the x-ray diffraction pattern of iron oxide thin films. The XRD pattern has been analyzed by origin lab software, and it showed that all the samples were polycrystalline in nature with rhombohedral structure of $\alpha\text{-Fe}_2\text{O}_3$ (JCPDF Card No. 84-0311) with space group of R-3c, also, the preferred orientation is along (104), which is consistent with the previously reported work [110-112]. The peaks appearing at $2\theta = 24.65, 33.56, 36.1, 39.7, 41.54$ and 54.7 can be attributed to (012), (104), (110), (006), (113) and (116) miller planes corresponding to pure $\alpha\text{-Fe}_2\text{O}_3$ nanoparticles which confirm the polycrystalline character. Texture coefficient is a quantitative measure used to estimate the preferred orientation of the thin films and is calculated using equation (2.4).

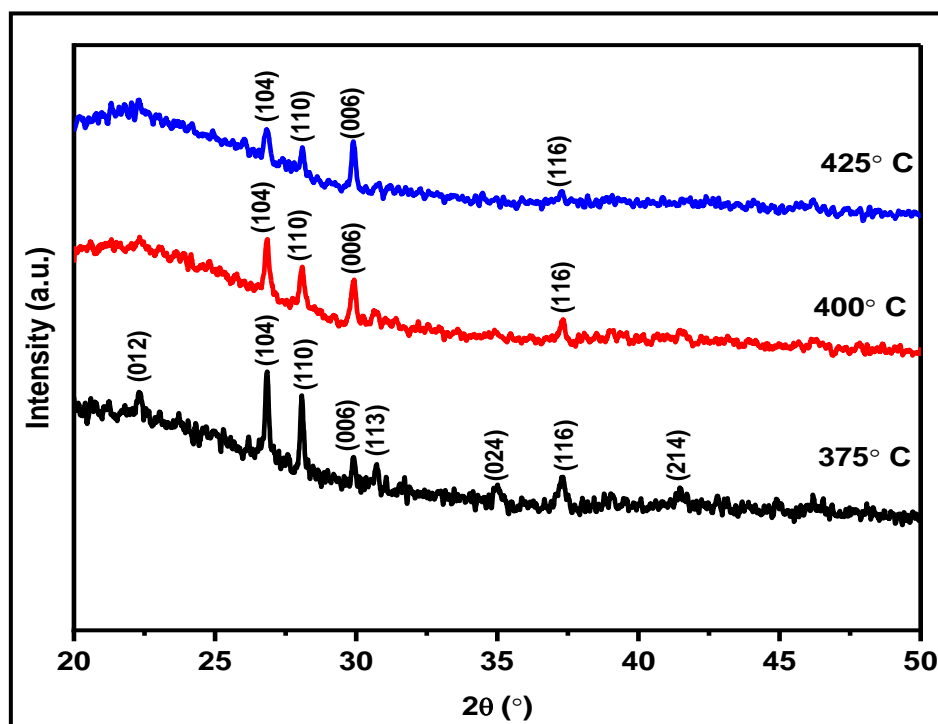


Fig.3.2: X-ray diffractogram of $\alpha\text{-Fe}_2\text{O}_3$ thin films prepared at various deposition temperatures

The preferred orientation of α -Fe₂O₃ thin films prepared at different deposition temperatures, is along the (104) plane. The intensity of the plane (104) is reduced as enhancing deposition temperature. The Crystallite size of the samples is determined using the Scherer's formula.

The micro-strain in the films is caused by deviations from the ideal crystalline lattice, and it might be produced due to dislocations, vacancies, residual stress, grain boundaries, and other defects in the crystalline material. Micro-strain in the films has been determined using the Williamson-Hall equation.

The dislocation density in the films measures the number of dislocations existing in the crystalline material per unit volume. The dislocation density in the crystalline thin films has been determined using the relation (2.6).

The number of crystallites per unit area can be determined with the equation (2.7). It relies upon structural specifications such as equispaced crystallites and the degree of the agglomeration of the deposited films. It is identified that the crystallite number increases as the substrate temperature enhances. The structural parameters of α -Fe₂O₃ thin films are given in table 3.3.

Table 3.3: Structural parameters of α -Fe₂O₃ thin films

S.No	Substrate Temperature (°C)	Texture Coefficient	Crystallite size (nm)	Strain (10 ⁻³)	Dislocation density(line/m ²) (10 ¹⁵)	No. of crystallites per unit area (10 ¹⁶ m ⁻²)
1	375	0.227	33.34	1.08	0.99	1.04
2	400	0.119	27.96	1.29	1.27	2.59
3	425	0.054	14.45	2.50	4.78	8.08

3.2.2 Field Emission Scanning Electron Microscopy

Field emission scanning electron microscopy is a sophisticated technique used to visualize topographical information on surface of the nano structured iron oxide thin films. Fig.3.3. depicts FESEM images of the iron oxide films sprayed at different deposition temperatures. The spherical, cubic and rectangular cuboids shaped nano crystals are visible on the thin iron oxide film deposited at a substrate temperature of 375 °C. The formation of

cuboid-shaped nano crystals might be explained in terms of variation in the growth mechanism caused by the substrate temperature.

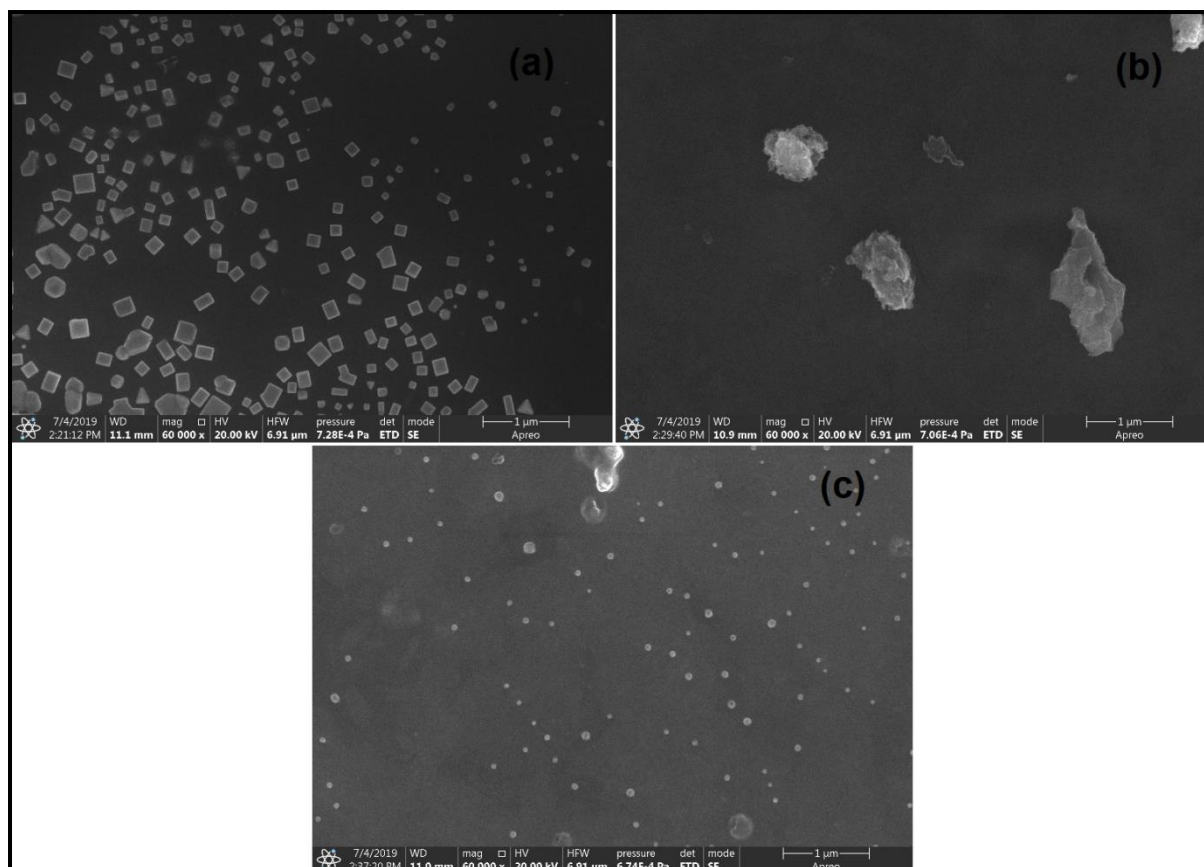


Fig.3.3: FESEM images of $\alpha\text{-Fe}_2\text{O}_3$ films sprayed at different deposition temperatures (a) 375 °C (b) 400 °C (c) 425 °C

The existence of such cuboid-shaped nano crystals in-grained on the thin film surface divided by homogeneously sprayed areas may be very useful for gas sensing applications [113-115]. Whereas the film is deposited at a substrate temperature of 400 °C consisting of agglomerated spherical-shaped crystallites, at this temperature films may have inserted higher stress on the thin film surface and the aggregations of ions take place in different directions. Thus the crystallites were grown in circular shapes and randomly ordered on the film surface.

3.2.3. Energy Dispersive by X-Ray (EDX) spectroscopy

An energy dispersive X-ray (EDX) spectrum of the $\alpha\text{-Fe}_2\text{O}_3$ films is shown in Fig. 3.4. Some features of Fe and O atoms can only be observed in this spectrum.

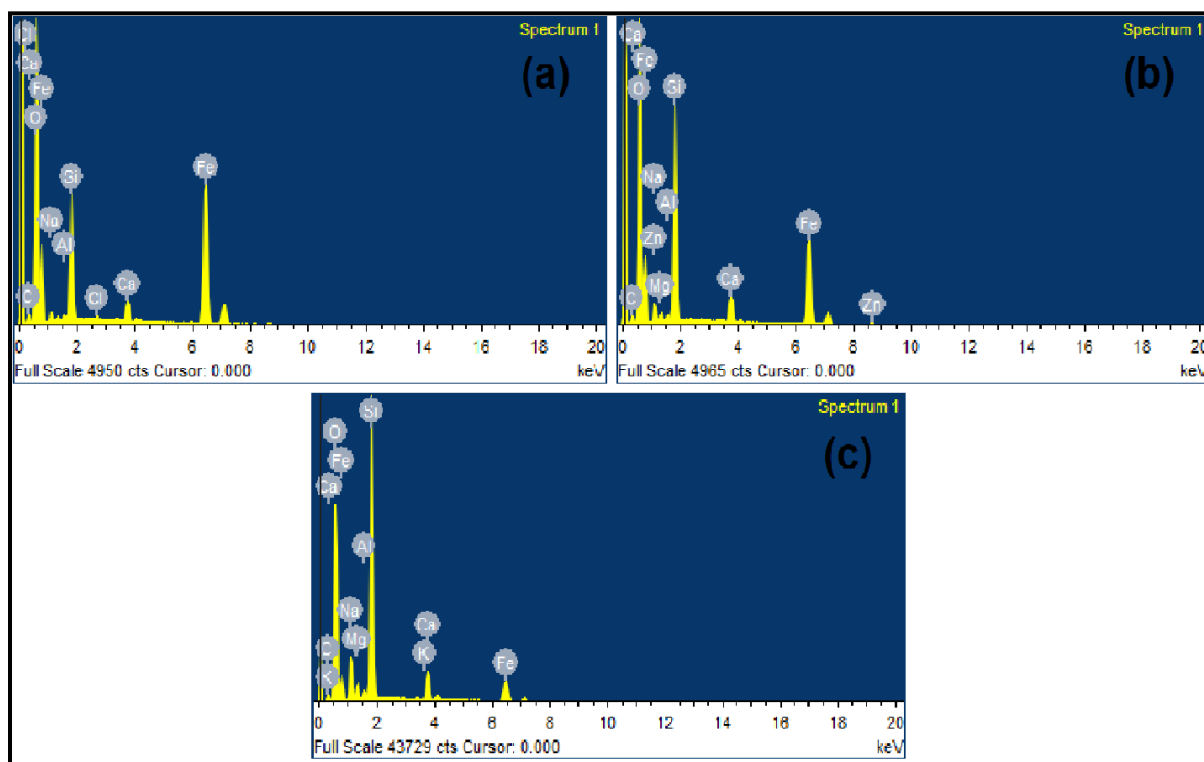


Fig.3.4: EDX of $\alpha\text{-Fe}_2\text{O}_3$ films sprayed at different deposition temperatures (a) 375 °C (b) 400 °C (c) 425 °C

Table 3.4: Elemental analysis of $\alpha\text{-Fe}_2\text{O}_3$ thin films

T(°C)	Element	Weight%	Atomic%
375	O	44.32	64.05
	Fe	38.09	15.77
400	O	50.18	66.52
	Fe	23.67	8.99
425	O	51.03	62.67
	Fe	7.43	2.61

The appearance of unknown peaks in the spectrum is due to the substrate. The presence of Fe and O atoms confirms good stoichiometry of the prepared $\alpha\text{-Fe}_2\text{O}_3$ films. The atomic and weight percentage of the elements in $\alpha\text{-Fe}_2\text{O}_3$ thin films are given in the table 3.4.

3.2.3 Atomic force microscope studies

AFM is an impressive technique of profilometry, utilized to extract topographical and morphology data from iron oxide films [116]. It provides quantitative analysis of the samples' surface properties [117]. It also investigates the microstructure of the deposited films [118,119]. With the help of AFM images, topographical information of films can be articulated in terms of highest and mean heights of the structures, and rms surface roughness[120,121]. AFM also explains films' grain dimension and distribution [122].

Furthermore, AFM figures can be investigated with fractal geometry methods such as power spectral density (PSD) functions to explain different convoluted surface morphologies and their impact on the surface features of the thin film [123]. Fig.3.5 depicts three-dimensional AFM profiles of the iron oxide films sprayed at different deposition temperatures. Surface features and quality of the iron oxide thin films can be examined by various parameters such as roughness, skewness, kurtosis. These parameters have been investigated using Nanoscope E software, and obtained values are tabulated in table3.5.

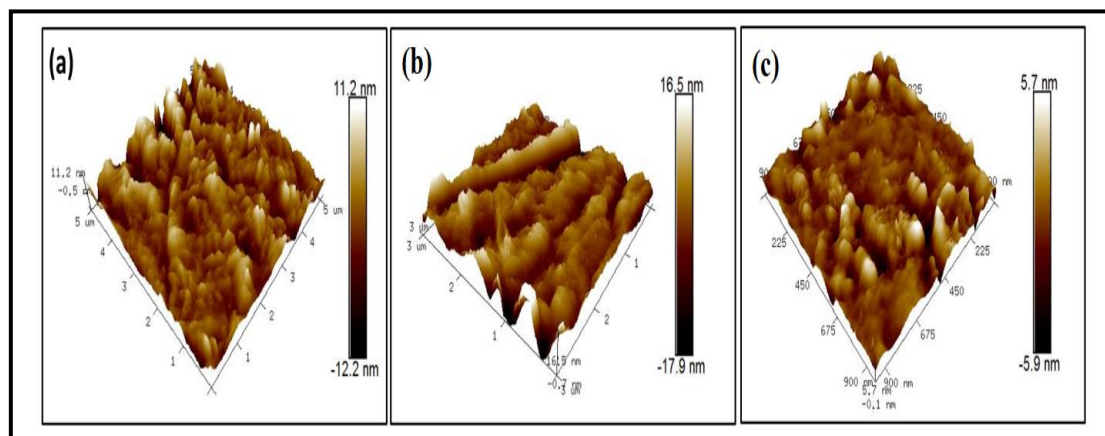


Fig.3.5: 3-dimensional AFM images of α -Fe₂O₃ thin films deposited at different substrate temperatures (a) 375 °C (b) 400 °C (c) 425 °C

Table.3.5: Surface features and quality of the α -Fe₂O₃ thin films

S.No	Substrate temperature °C	Surface area (μm ²)	Roughness (nm)	Skewness	Kurtosis
1	375	0.932	139	-5.17	785
2	400	0.944	104	-1.27	93.2
3	425	0.932	16.2	0.142	3.79

From the table 3.5, it is clear that the roughness of the film is decreased with increasing substrate temperature. The calculated skewness of the films is shown in table 3.5, and the negative skewness is a criterion for a high symmetry of the film surface.

3.2.4 X-ray photoelectron spectroscopy studies

XPS analysis is a flexible tool for the study of surface analysis and also can be utilized for the electronic states of the elements that exist in the sample and can be made at a depth of about 5–10 nm from the surface. Few transition metal chemical states give rise to important intensity components in their 2p spectra due to various splitting producing a contribution that is generally not considered [124]. Fig. 3.6 depicts the binding energies of Fe 2p_{3/2}, and Fe 2p_{1/2} appeared at 710.39 eV and 723.97 eV, respectively, these are the typical peaks related to the Fe³⁺ oxidation state of the hematite α -Fe₂O₃ film [125,126]. The binding energy difference of the Fe 2p_{3/2} binding energy at 710.39 eV and that of the corresponding satellite peak is 7.59 eV, proving the oxidation state of Fe³⁺.

To determine the presence of oxide/hydroxyl species in α -Fe₂O₃ thin film, an O 1s spectrum is measured, and depicted in Fig. 3.7. A high intense and sharp peak can also be seen at the binding energy of 529.5 eV related to the major oxygen lattice contribution and is ascribed to the oxygen existence in the metal ion (Fe⁺³) in α -Fe₂O₃. A slight shift in binding energy towards a lower side is observed at high substrate temperature is due to the bond condition.

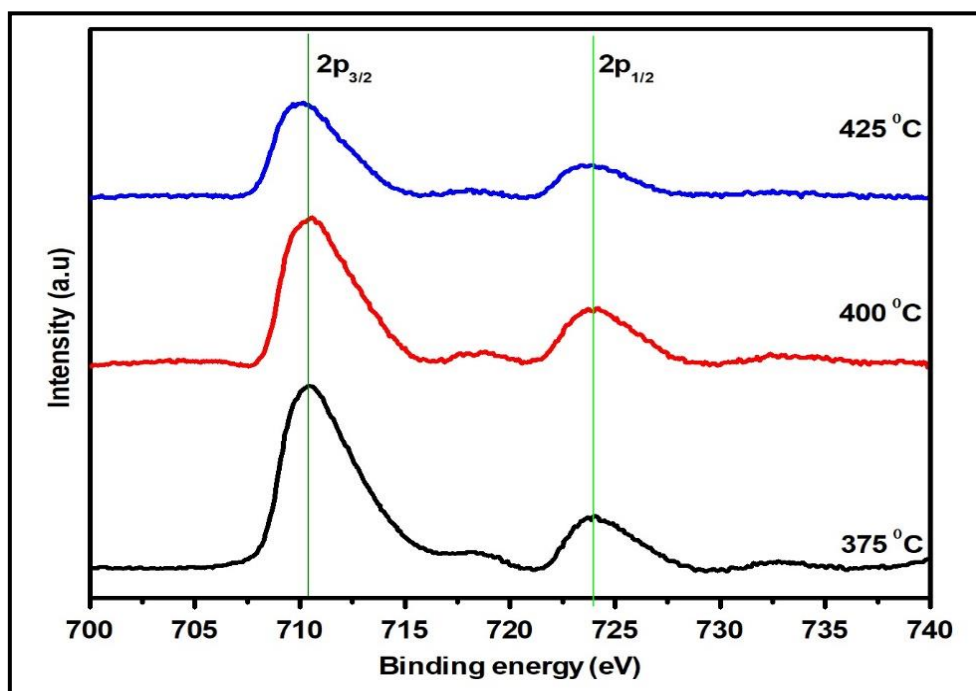


Fig.3.6: XPS spectra of Fe 2p core-shell of $\alpha\text{-Fe}_2\text{O}_3$ thin films prepared at different deposition temperatures

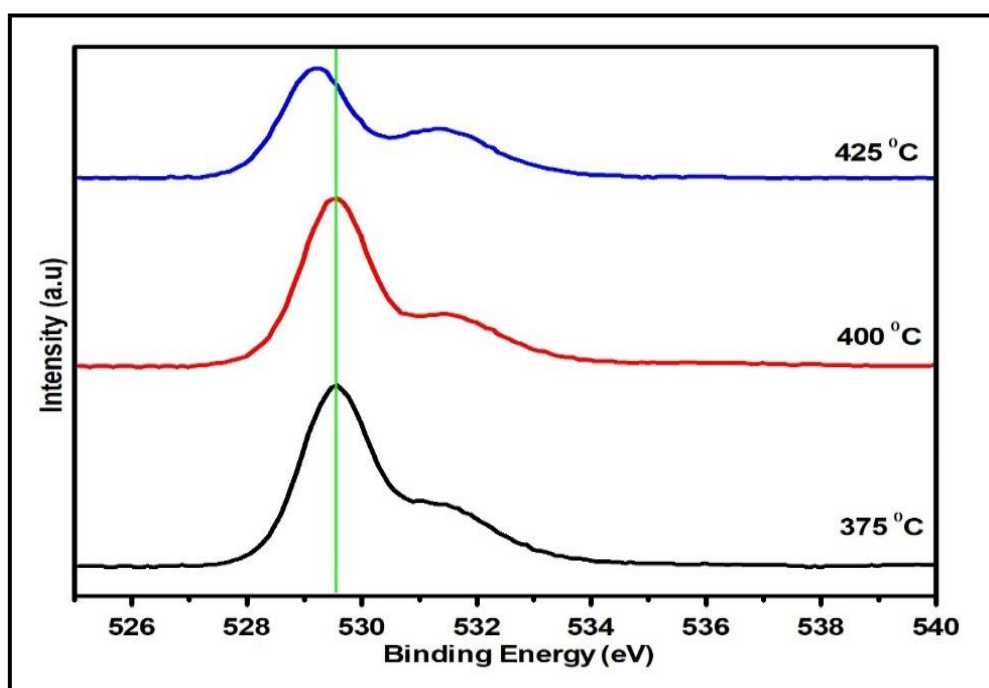


Fig.3.7: XPS spectra of O1s core-shell of $\alpha\text{-Fe}_2\text{O}_3$ thin films deposited at different deposition temperatures

3.2.5 Optical studies

The optical studies of the iron oxide films coated at different deposition temperatures are determined using a UV-Visible spectrophotometer at room temperature. The optical characterization of the thin films can be interpreted in view of the interaction between the incident photon and thin films. The films' absorption coefficient and optical band gap was determined using obtained absorption data. The absorption coefficient of the iron oxide thin films was calculated using the following relation [127].

$$\text{Absorption coefficient } (\alpha) = \frac{A}{t}$$

Where 'A' is the absorbance and 't' is the thickness of the film. The optical band gap of α -Fe₂O₃ film was evaluated by adopting a Tauc plot using direct transition of absorption spectra.

$$(\alpha h\nu)^2 = A (\alpha h\nu - E_g)$$

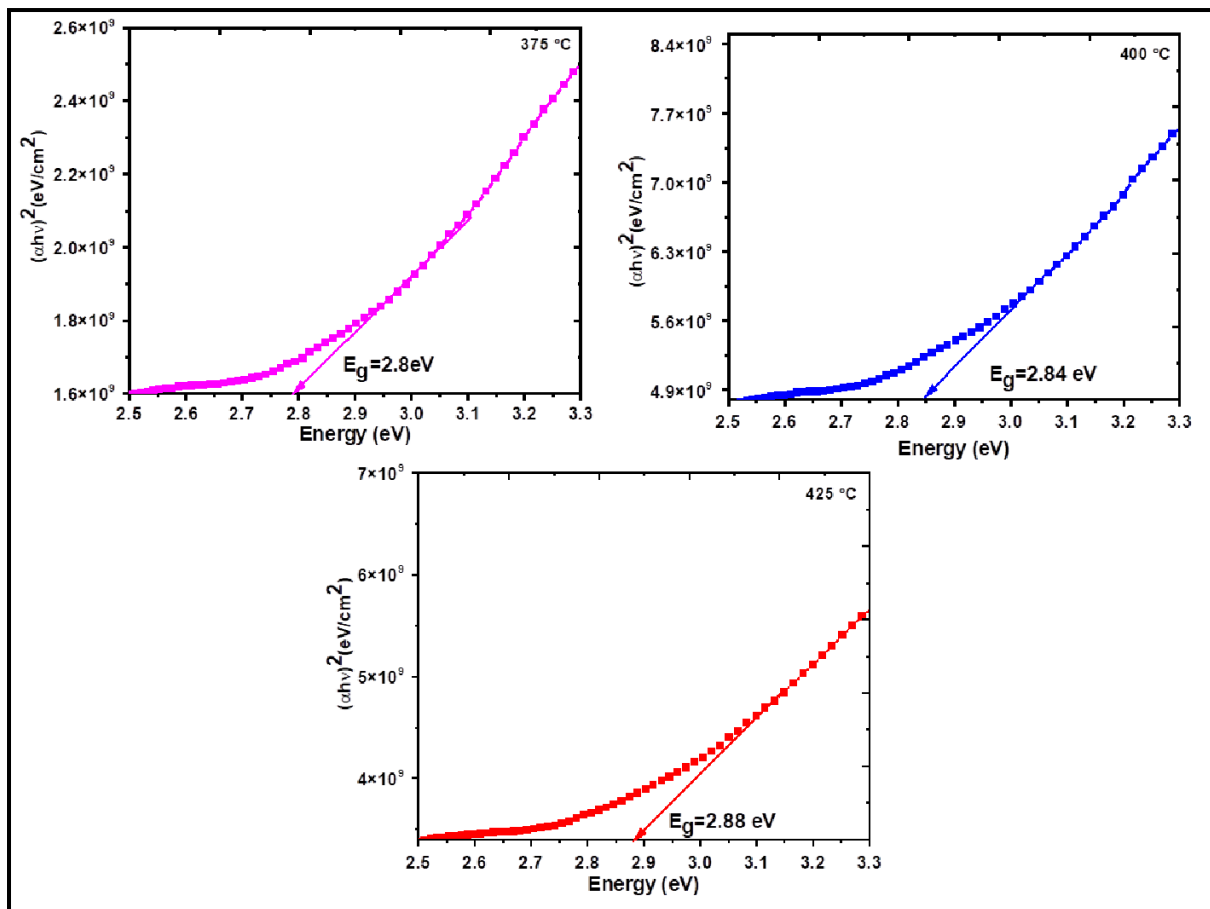


Fig.3.8: Tauc plots of α -Fe₂O₃ thin films deposited at different substrate temperatures

Where 'h' is plank constant, 'v' is the incident photon's frequency, 'E_g' is the band gap of films. The plot of $(\alpha hv)^2$ and incident photon energy is depicted in Fig.3.8. The optical band gap is determined by the extrapolating linear portion of the absorption edge to the horizontal axis. Obtained bandgap values are tabulated in the table3.6.

Table 3.6: Optical band gap of α -Fe₂O₃ thin films

S.No	Substrate temperature (°C)	Optical band gap (eV)
1	375	2.80
2	400	2.84
3	425	2.88

3.3 Gas sensing characterization

To investigate gas sensing properties, on the α -Fe₂O₃ thin film surface, two electrodes are printed with a spacing of 10mm using high purity silver paste and heated at 150°C for two hours to obtain good electrical contacts. For further studies, the fabricated sensor element is kept in the home-made metallic gas sensing chamber. The working phenomenon of a gas sensor predominantly depends on optimising three important parameters such as sensitivity, selectivity, and stability. To attain this, the control of the material utilised, micro-structural, and study of crystallite shapes are needed to design the best sensor response. The sensitivity of the sensor element towards reducing gases is measured using the following relation [128].

$$\text{Response} = \frac{R_a}{R_g}$$

Where R_a is sensor element's resistance in dry air atmosphere and R_g is the sensor element's resistance in the presence of the test gas.

Selectivity or cross-sensitivities is an important property that evaluates its anti-interference ability. Selectivity of the sensor elements towards 5ppm of different reducing gases such as acetone, ammonia, methanol, ethanol, toluene, formaldehyde, and ethyl benzene at a working temperature of 27°C is shown in Fig.3.9. Among all the sensors, the film prepared at a substrate temperature of 375 °C has exhibited the maximum response towards ammonia vapours. Hence this sample might be used for further gas sensing characteristics such as sensitivity (response), stability, repeatability and the transient response.

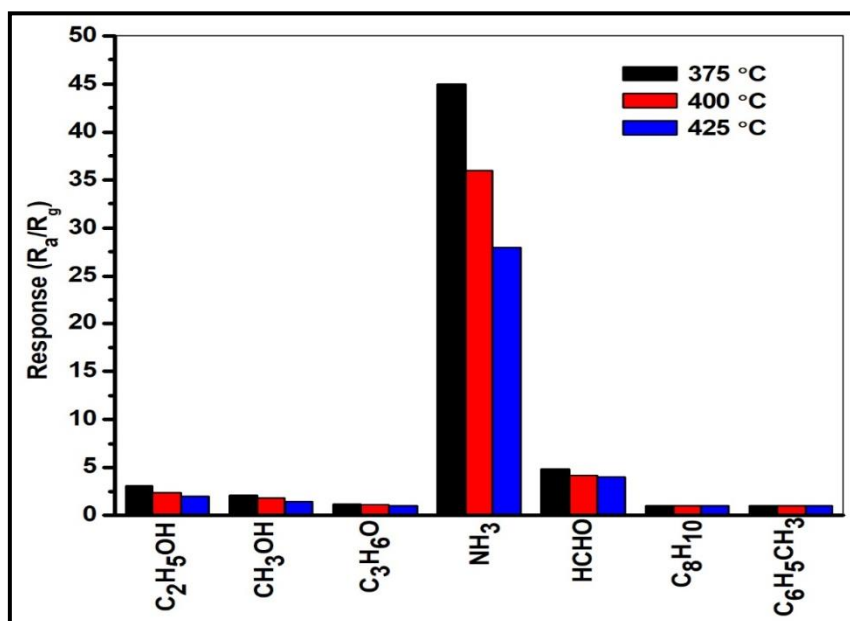


Fig.3.9: Selectivity of $\alpha\text{-Fe}_2\text{O}_3$ films deposited various deposition temperatures towards different gases.

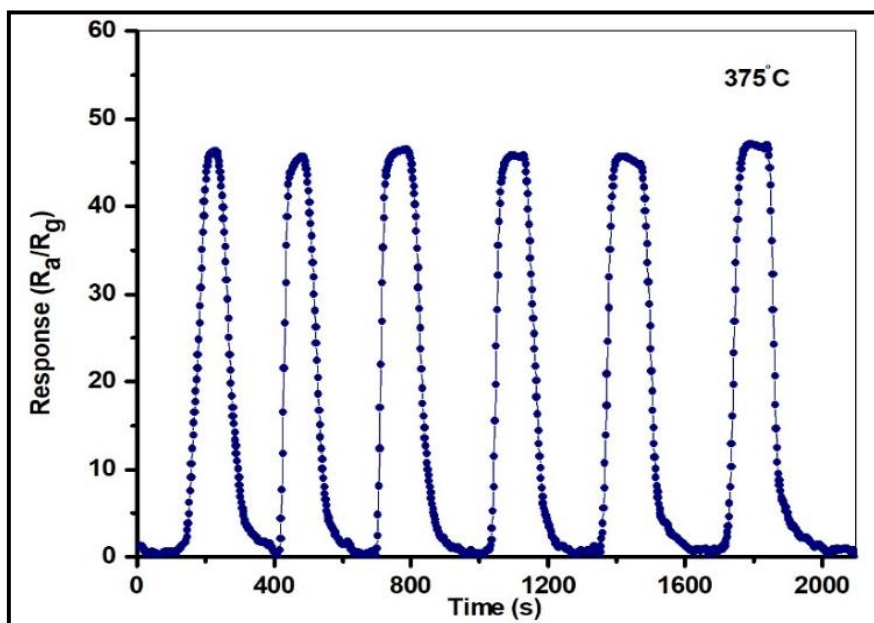


Fig.3.10: Repeatability of $\alpha\text{-Fe}_2\text{O}_3$ thin film deposited at 375°C

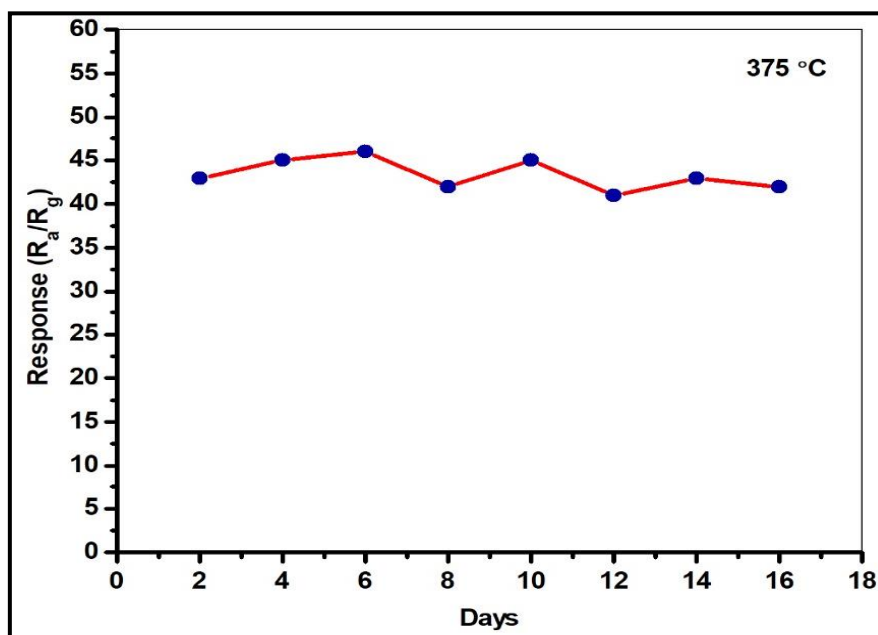


Fig.3.11: Stability of α -Fe₂O₃ thin film prepared at 375°C

The short term repeatability of the sensor element towards 5ppm ammonia vapours during the continuous operation of target gas under identical conditions is shown in Fig.3.10. The sensor element has shown almost the same response in all the cycles of the experiment indicating the repeatability of the sensor element is stable without any visible degradation.

The stability of the sensor will play a significant role in all the practical applications of sensor devices. The film, which is deposited at 375°C, has taken for the repeatability test over a period of 18 days. A negligible variation in response is noticed during these days as shown in Fig.3.11.

One of the most essential factors in gas sensor properties is the low limit of detection (LOD). As per the International Union of Pure and Applied Chemistry (IUPAC), the detection limit can be explained as the least concentration of a gas that the device can detect under its operating principle. The sensor's response with reference to the concentration of the test gas is plotted in Fig. 3.12. From this figure, 5 points are chosen, and then the slope of this curve and the standard deviation are analyzed. Using these parameters in the equation for LOD given in the below expression [129,130], the detection limit determined is about 2.3 ppm. According to the National Institute for Occupation safety, the short time exposure of ammonia by a human is 25ppm for 15 minutes [131-134].

$$\text{LOD} = 3 \times \left(\frac{\text{standard deviation}}{\text{slope}} \right)$$

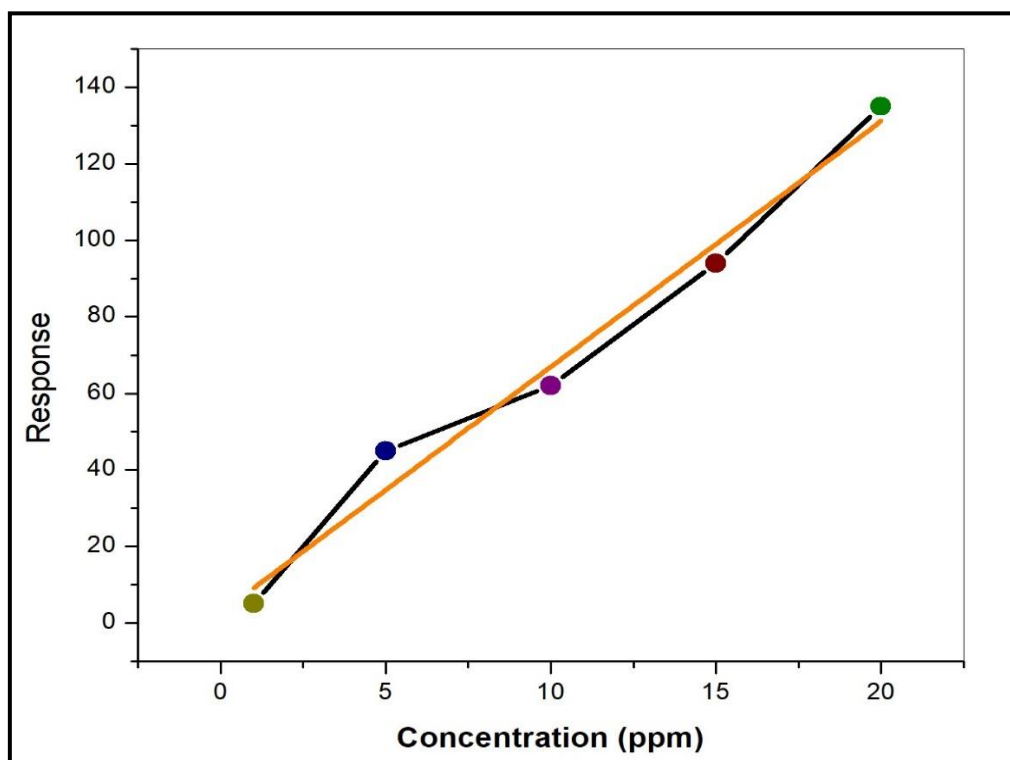


Fig.3.12: Variation of response at different concentrations of ammonia towards Fe_2O_3 thin film deposited at 375°C .

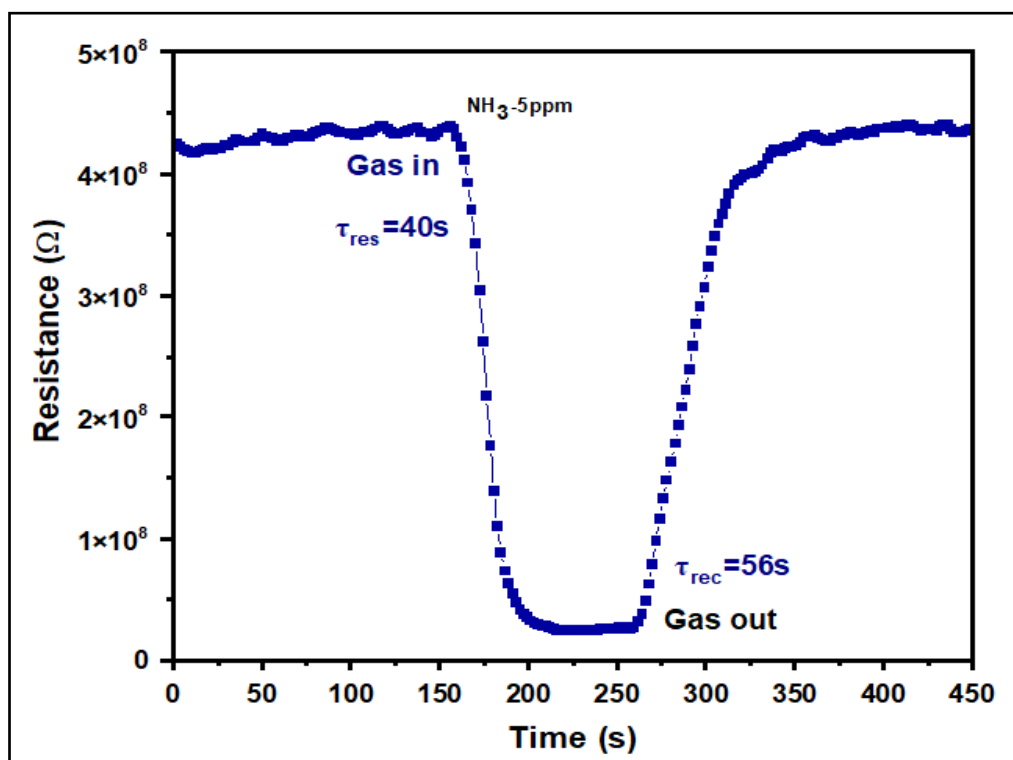


Fig.3.13: Transient response curve of Fe_2O_3 thin film prepared at 375°C

3.3.1 Response and recovery characteristics

Figure 3.13 shows the transient response curve of Fe₂O₃ thin film prepared at a deposition temperature of 375° towards 5 ppm of ammonia at an operating temperature of 27°C. The time needed to reach 90% of the final resistance of the sensor material under the exposure to target gas is called as the response time of the sensor, it is computed as 40s, and the recovery time is interpreted as the time required for the sensor element to revert to its 10% of its saturation state resistance when the target gas is withdrawn from the sensing chamber, it is found as 56s.

3.4 Summary

α -Fe₂O₃ thin films have been successfully deposited using cost-effective spray pyrolysis technique at different substrate temperatures with optimized deposition parameters. X-ray diffraction studies of deposited thin films have shown polycrystalline nature. The morphological investigations reveal that the thin film deposited at a substrate temperature of 375°C has shown homogeneous cuboid-shaped nano crystals, which is a very useful morphology for chemiresistive gas sensing studies. The surface characterization performed using AFM revealed that the substrate temperature greatly influenced the microstructure of the films during the deposition process. The film deposited at 375°C has a much rougher surface than other films. It is well known that the gas sensing properties of the sensor element are enhanced with increasing surface roughness of the film due to the available number of active adsorption sites for oxygen molecules on the sensor surface being improved. The gas sensing results of continual short-term investigations over 18 days using 5 ppm of ammonia have shown a stable response with excellent sensitivity and selectivity. Also, the response and recovery characteristics demonstrated a significant enhancement compared to previous results. These results will be highly beneficial in designing and developing α -Fe₂O₃ thin-film sensors, which are very useful in measuring ammonia levels in pounds in the aqua industry.

Chapter-4 Synthesis and characterization of Al-doped Fe₂O₃ thin films for formaldehyde gas sensing application

4.0 Introduction

The term "volatile organic compounds" (VOCs) refers to substances with a high vapour pressure but limited solubility in water. Formaldehyde, benzene, xylene, toluene, ethylene glycol, tetrachloroethylene, methylene chloride, etc., are the most common VOCs in our daily life. Formaldehyde (HCHO) is widely used as an ingredient in many industrial and consumer products such as cars, computers, rubber items, wood products, adhesives, colors, plastics, electronics, and the production of various organic compounds [135-137]. This substance was classified as "known to cause human cancer" [138] by the U.S. National Toxicology Program in 2016. HCHO is also a potential carcinogen due to its high toxicity, wide distribution, and volatility. It can harm the central nervous system, impair the immune system, and induce blindness, respiratory illnesses, and heart attacks in asthmatics. The World Health Organization (WHO) has limited long-term average formaldehyde exposure to 0.08 ppm per 30 min. However, the National Institute for Occupational Safety and Health (NIOSH) has specified a safe exposure level of 1 ppm [139,140]. Hence it is a big challenge to the researchers to design a simple, affordable, low-concentration detectable and operating at ambient temperature gas sensors in and around workplaces to monitor the level of HCHO in real-time.

Several research groups have optimized metal oxide-based devices for applications such as electronic, magnetic, photonic, medical, catalysis and gas sensors [141–144]. Due to their accessibility, affordability, stability, high sensitivity, compatibility with microelectronic processes, and wide availability, iron oxide-based materials are the most exciting and best option in this competition. Iron oxides have drawn interest in the realm of sensors because of their distinctive properties [145–150]. Iron oxide is an environmentally acceptable, nontoxic substance with good sensitivity and selectivity and is electrochemically stable. Additionally, it is a strong contender for several applications, including photo catalysis, nonlinear optics, and solar cells [151–153].

Due to these concerns, numerous techniques for developing Fe₂O₃ thin films have been reported, which include chemical precipitation [154], electrodeposition [155], sol-gel [156], hydrothermal deposition [157], and chemical spray pyrolysis [158,159]. Among these techniques, spray pyrolysis is unquestionably the most appropriate due to its many benefits, including simplicity, low cost, the ability to control the deposition parameters, flow speed and

Chapter-4 **Synthesis and characterization of Al-doped Fe₂O₃ thin films for formaldehyde gas sensing application**

distance between the substrate and nozzle, and scalability. It has been established that doping significantly altered metal oxides' physical, chemical, and sensor performance. In this regard, G. Neri et al. used the liquid phase deposition method (LPD) to manufacture Ca and Pd-doped Fe₂O₃ thin films-based sensors; they showed that the ethanol sensitivity and selectivity rose for Ca-doped sensor, while decreased for Pd-doped sensor [160]. Mg: Fe₂O₃ was found to have the best response when S. Saritas et al. manufactured spray pyrolysis deposited Fe₂O₃, Mg: Fe₂O₃, and Ni: Fe₂O₃ thin films and tested to NO₂, H₂S, CH₃OH, CH₅OH, and NH₃ gases response towards 200 ppm at 200 °C as an operating temperature [161]. The disadvantage of the reported Fe₂O₃-based HCHO sensors is their operating temperature, which shows good sensitivity at high temperatures. Reports have been published to increase the sensing capability of metal oxides by doping with aluminium. Al addition to α -Fe₂O₃ lattice leads to an increased specific surface area which enables a beneficial influence on gas sensing properties of various gasses [162–164].

In the present work, we studied aluminium (Al) doping into the α -Fe₂O₃ lattice to increase gas sensing capabilities. Al-doped α -Fe₂O₃ (0, 5, 10, and 15 wt%) thin films were prepared using the chemical spray pyrolysis method and subsequently annealed at 450°C, and their gas sensing capabilities were examined. The gas detection capabilities were tested at various HCHO vapour concentrations. The impact of Al doping on the morphological and structural, elemental composition, and optical characteristics of α -Fe₂O₃ thin films was systematically investigated and reported.

4.1 Experimental Techniques

4.1.1 Synthesis of Pure and Al-doped Fe₂O₃ thin films

To prepare iron oxide and Al-doped iron oxide thin films, Fe(NO₃)₃.9H₂O and Al(NO₃)₃.9H₂O were used as starting precursors procured from Sigma Aldrich. Fe(NO₃)₃.9H₂O was dissolved in double-distilled water and stirred using a magnetic stirrer to prepare pure iron oxide thin films. The obtained clear solution was used to prepare iron oxide thin films. Whereas, for the preparation of Al-doped iron oxide, aluminium nitrate (Al(NO₃)₃.9H₂O) was dissolved in double-distilled water and added Fe(NO₃)₃.9H₂O solution in an appropriate proportion. The solution was agitated with a magnetic stirrer at 300 revolutions per minute at room temperature for a few minutes to create a homogeneous solution. The doping concentration ranges from 0 to 15 wt% with a 5 wt% variation. Pure and Al-doped α -Fe₂O₃ thin films were deposited using

Chapter-4 Synthesis and characterization of Al-doped Fe₂O₃ thin films for formaldehyde gas sensing application

Holmarc (HOTH-04BT) spray pyrolysis equipment with optimized deposition parameters as shown in the 3.1 by spraying the prepared solution on pre-heated glass substrates, heated to 375°C. The methodology of the chemical spray pyrolysis process was extensively discussed in chapter-2 [165]. After deposition, thin films were cooled to normal conditions and then annealed for 6 hours at 450°C in the presence of the vacuum. The cross sectional view of the deposited thin films is shown in figure 4.1.

Table.4.1. Deposition parameters of Al doped α -Fe₂O₃ thin films

Deposition parameter	Values
Nozzle to substrate distance	25cm
Temperature	375°C
Flow rate	1ml/min
Spray time	10min
Concentration of solution	0.1M
Volume of solution	40ml
Precursor	Fe(NO ₃) ₃ · 9H ₂ O and Al(NO ₃) ₃ · 9H ₂ O
Compressed air pressure	2.94 Bar
Solvent	De-ionized water
Substrate	Glass (Blue star, India)

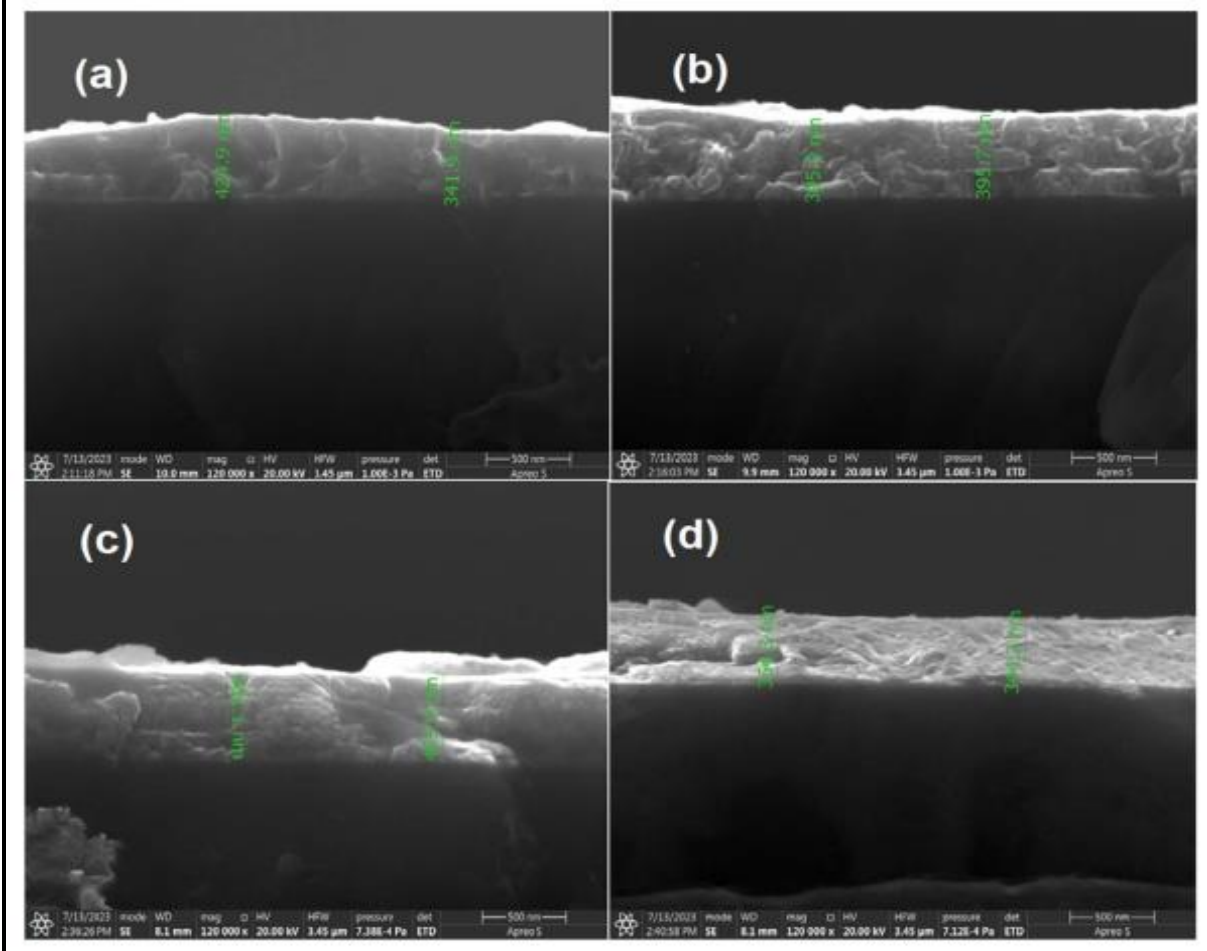


Fig. 4.1: Cross section view of Al-doped $\alpha\text{-Fe}_2\text{O}_3$ thin films annealed at 450 °C (a) Pure (b) 5 wt% Al (c) 10 wt% Al (d) 15 wt% Al

The prepared samples were analyzed for structural properties using X-ray diffraction. Based on the obtained data, we have annealed all the samples at 450°C for 6 hours. These annealed samples were used for further analysis, such as structural, micro structural, and optical properties. The films' crystallinity was studied using the Rigaku (ULTIMA-IV) X-ray diffractometer with the $\text{Cu-K}\alpha$ ($\lambda=0.154$ nm) radiation throughout a continuous diffraction angle (2θ) range of 20° to 80° at a scan speed of 2°/min. High-resolution FE-SEM and AFM (NaioAFM, Nanosurf AG Switzerland, 60-14-080) were utilized to examine the surface morphologies of the annealed films. EDAX was utilized to determine the elemental composition. Using Raman spectroscopy, structural distinctions of the thin films were investigated. XPS was used to validate the oxidation states of the $\alpha\text{-Fe}_2\text{O}_3$ and Al-doped $\alpha\text{-Fe}_2\text{O}_3$ thin films with Thermo Fisher Scientific (U.K.). A UV-Vis-NIR spectrophotometer (Jasco V650) was used to

Chapter-4 Synthesis and characterization of Al-doped Fe₂O₃ thin films for formaldehyde gas sensing application

investigate optical measurements ranging from 250 nm to 1200 nm. An indigenously constructed gas-sensing device was employed to characterize gas-sensing properties utilizing a computer-interfaced Keithley's (6517B) electrometer in static mode.

4.2 Results and discussion

4.2.1 X-ray diffraction

XRD spectrum showed that the pure α -Fe₂O₃ sample was polycrystalline with a favoured direction along (104), in consistent with earlier reports [166–167]. Increasing the Al doping levels to 15%, no preferred phase was found. Figure 4.2 displays the X-ray diffraction pattern of pure and Al-doped Fe₂O₃ films deposited at 375°C with varying Al doping levels. Hence we have attempted to anneal the samples to study the structural, morphological, optical, and gas-sensing properties. Figure 4.3 shows the X-ray diffraction pattern of the sample annealed at 450°C for 6 hours. The formation of rhombohedral α -Fe₂O₃ is indicated by the diffraction peaks corresponding to the (012), (104), (110), (113), (024), (116), (214), (300), and (1010) planes in consistency with JCPDF card No. 84-0311. Increasing Al concentration to 10 wt% led to α -Fe₂O₃ formation with (104) plane as the preferred orientation. The peaks with less intensity were observed at 20.1°, 45.5°, and 67.6°, which correspond to the (110), (042), and (252) Miller planes of the Fe₂O₃ phase, which are in agreement with JCPDF card No. 89-7047. The peaks corresponding to the (012), (113), (024), (116), and (1010) planes of the α -Fe₂O₃ phase disappeared, and the intensity of other peaks was diminished in the case of 15 wt% Al-doped Fe₂O₃ thin films. It might be due to the ionic radius mismatch of iron with aluminium ions. R. Ben Ayed et al. reported similar outcomes [168]. The texture coefficients of the films were calculated using the relation (2.4) to determine the preferential orientation in the annealed thin films. Scherer's formula (2.3) was used to determine the crystallite size along the preferential direction of annealed films.

Since deviations were observed as Al doping, to get predictable knowledge, structural characteristics like dislocation density, micro-strain, and number of crystallites per unit area of the crystalline material were evaluated using the relation (2.6) and the estimated values are shown in Table 4.1.

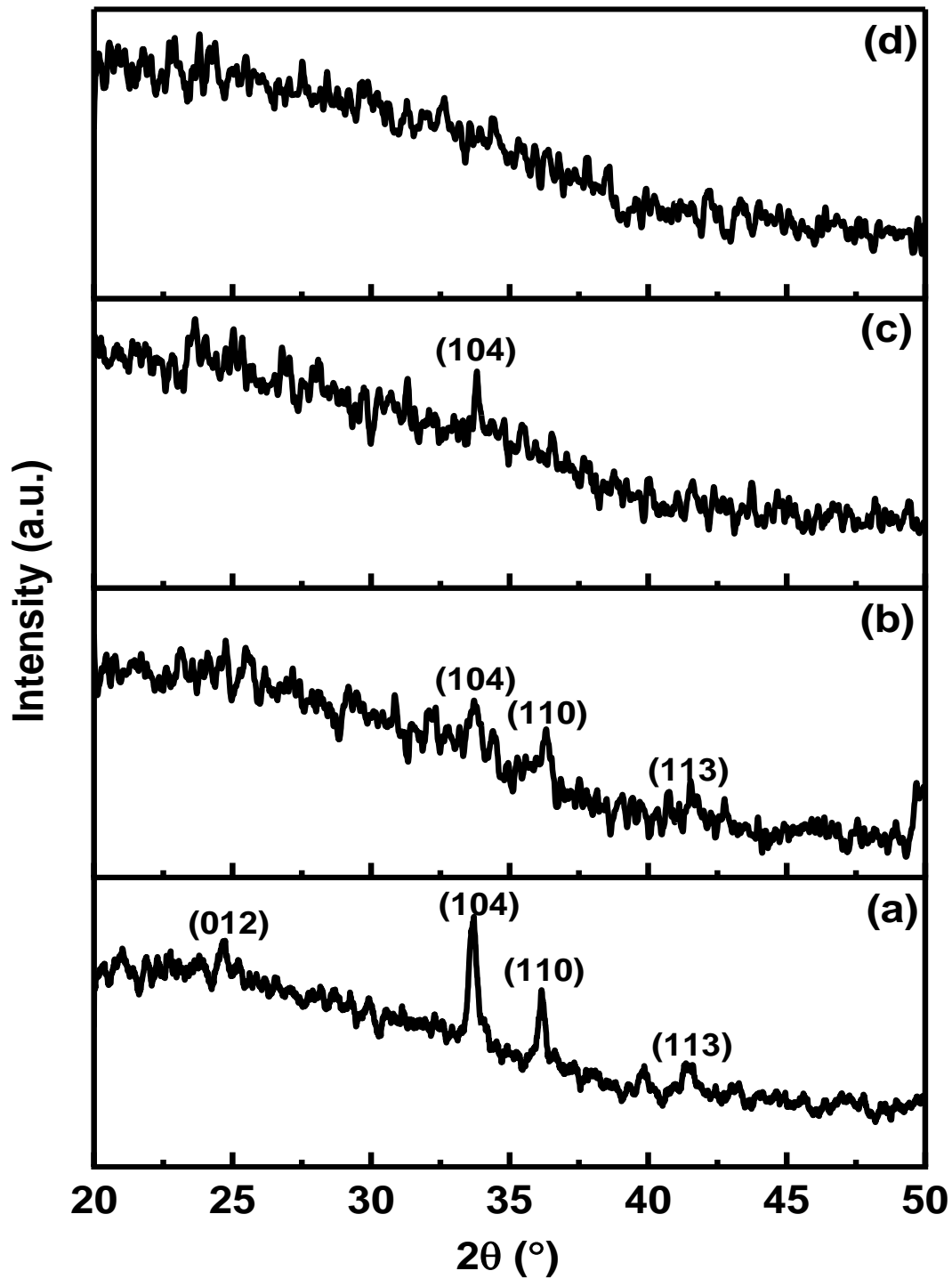


Fig.4.2: X-ray diffraction profile of Al-doped $\alpha\text{-Fe}_2\text{O}_3$ thin films as deposited at 375 $^\circ\text{C}$ (a) pure, (b) 5 wt% Al, (c) 10 wt% Al, and (d) 15 wt% Al.

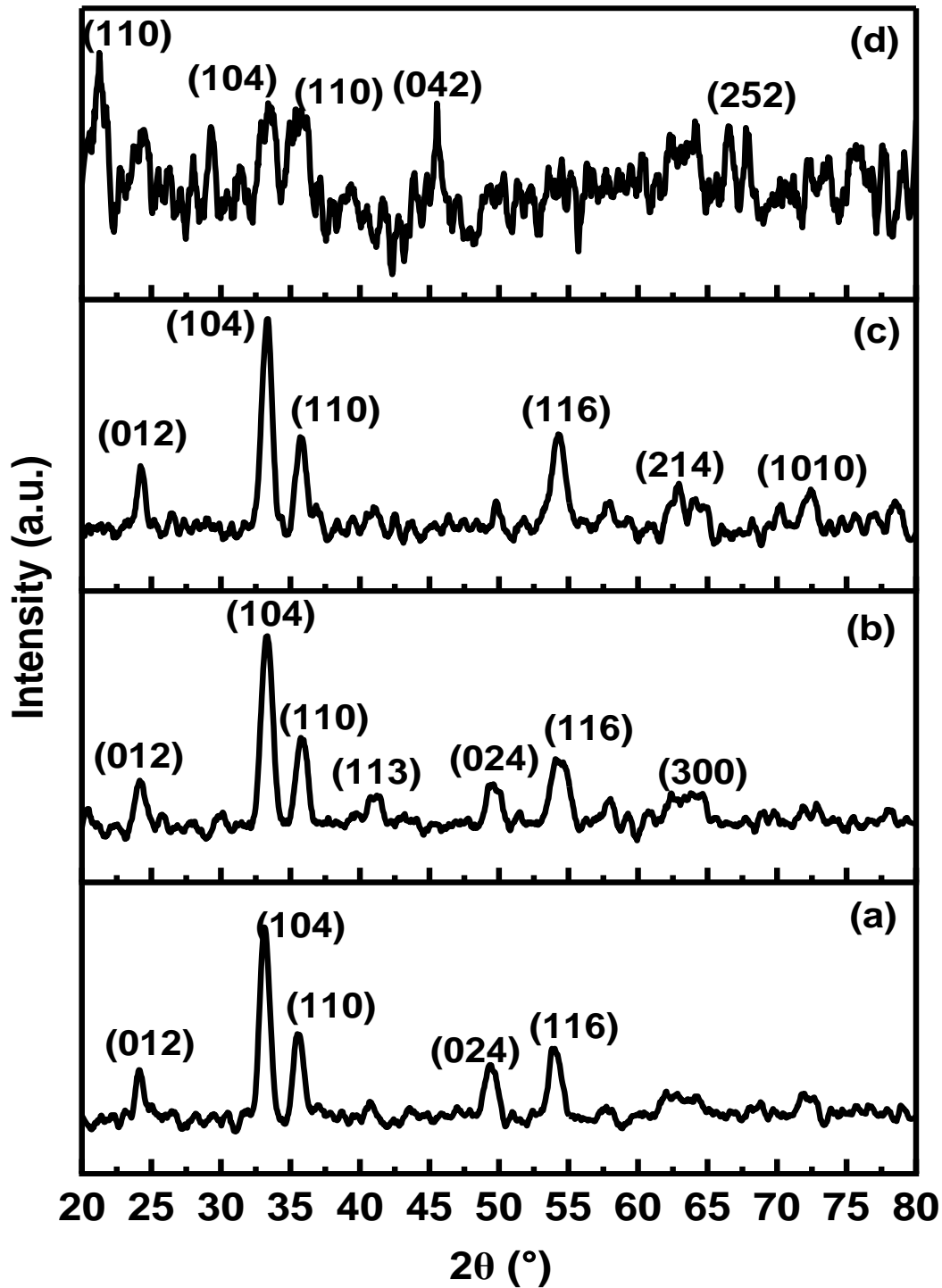


Fig. 4.3: XRD spectra of Al-doped $\alpha\text{-Fe}_2\text{O}_3$ thin films annealed at 450°C (a) pure, (b) 5 wt% Al, (c) 10 wt% Al, and (d) 15 wt% Al.

Chapter-4 Synthesis and characterization of Al-doped Fe₂O₃ thin films for formaldehyde gas sensing application

Using Williamson–Hall equation, the micro strain (ϵ) that occurred in the films was estimated [169]. The degree of crystallization to which the deposited films have aggregated is calculated using the equation (2.7). The number of crystallites per unit area can affect structural criteria like equispaced crystallites.

The estimated crystallites' size varies between 7.34 and 65.1 nm, as shown in Table 4.2. The thin film doped with 10 wt% yields the largest crystallite size of 65.1 nm with the best crystallinity. The partitioning of Al at grain boundaries is the cause of the reduction in crystallite size in the case of the sample with the high dopant concentration [170]. This behaviour is due to dopant ions' propensity to create new nucleation sites, which will cause the nucleation to change from homogeneous to heterogeneous and impair the crystallinity [167]. The typical micro strain and dislocation density values varied in the range of 2.93×10^{-3} to 15.5×10^{-3} and from 0.23×10^{15} to $18.5 \times 10^{15} \text{ m}^{-2}$, respectively. The 10 wt% Al-doped Fe₂O₃ sample has shown the best values for both criteria. These findings demonstrate that Al doping leads to a restoration of α -Fe₂O₃ crystallinity. Otherwise, the crystallinity deteriorates at greater doping levels.

Table 4.2: Structural characteristics of Al-doped α -Fe₂O₃ thin films annealed at 450°C

S.NO	Al concentration (wt%)	Texture coefficient	Crystallite size (nm)	Strain (10^{-3})	Dislocation density (10^{15} line/m^2)	No. of crystallites per unit area (10^{19} m^{-2})
1	0	1.115	11.87	3.73	7.09	0.10
2	5	1.418	10.26	4.05	9.48	0.22
3	10	1.142	65.1	2.93	0.23	0.11
4	15	0.105	7.34	15.5	18.5	30.7

4.3.2. Field Emission Scanning Electron Microscopy

Figure 4.4 displays the morphological observations of the FESEM investigation of Al-doped α -Fe₂O₃ films. The film's morphology demonstrates the existence of grains, confirming that the grown films are polycrystalline. This is pretty consistent with the XRD findings. The surface structure changes significantly when the 'Al' is added to α -Fe₂O₃.

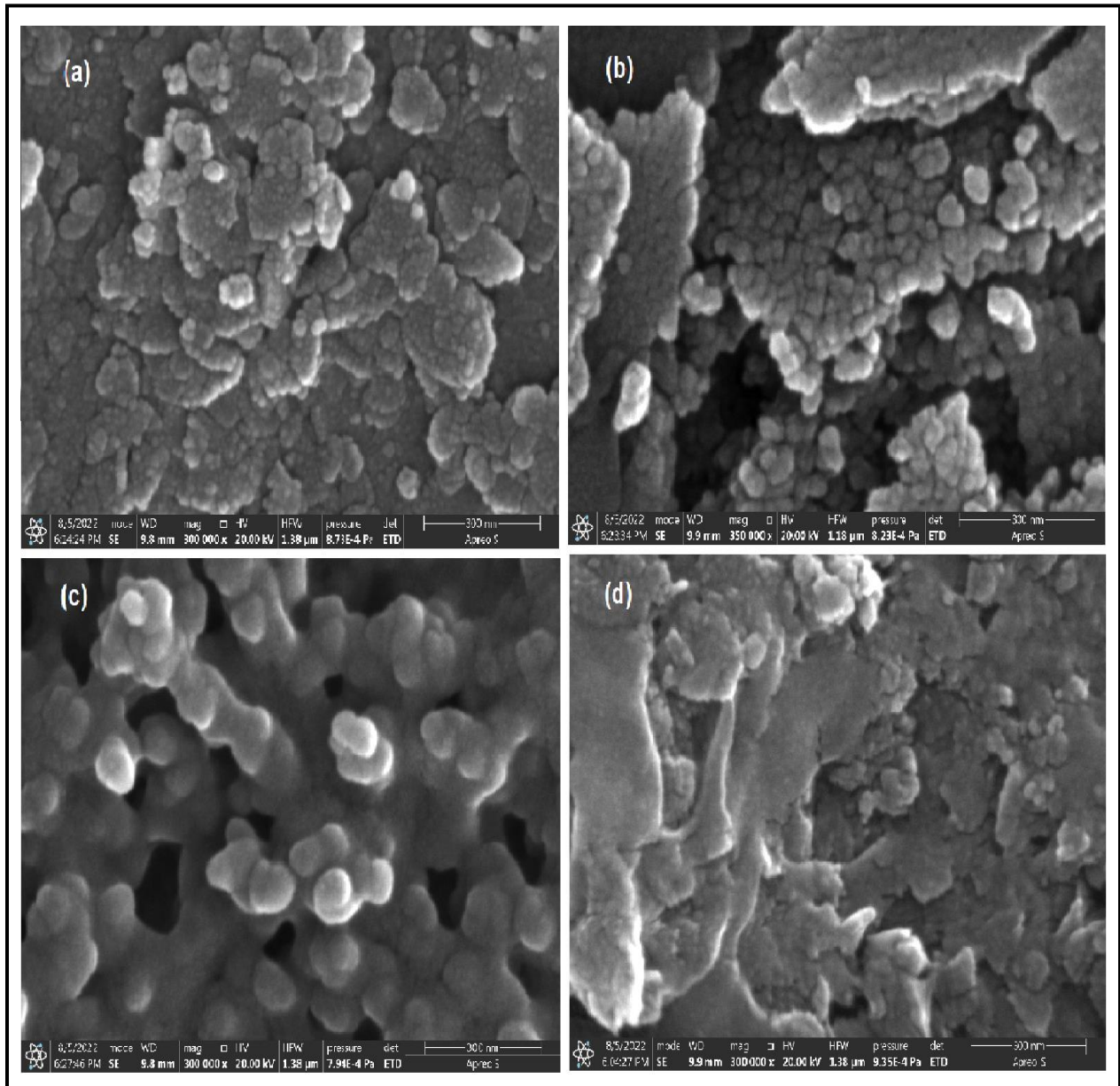


Fig. 4.4: FE-SEM micrographs of Al-doped α - Fe_2O_3 thin films annealed at 450°C a) Pure b) 5 wt% Al c) 10 wt% Al d) 15 wt% Al

Chapter-4 Synthesis and characterization of Al-doped Fe₂O₃ thin films for formaldehyde gas sensing application

Large and medium grain agglomerations are visible in pure and 5wt% Al-doped films (Figure 4.4a and 4.4b). When 10 wt% of aluminium is added, the agglomeration is less pronounced a superimposed sphere-like porous structure can be visible (Figure 4.4c) [171]. Re-agglomeration of crystallites is caused by further doping (15 wt% of Al), and thin films showed accumulation rather than a monodisperse with more compact morphology (Figure 4.4d).

4.2.3. Energy dispersive X-ray spectroscopy

Using the EDX, the chemical composition of Al-doped α -Fe₂O₃ thin films was investigated. Figures 4.5 and 4.6 depicts the EDX spectra of annealed pure, 5, 10, and 15 wt% Al-doped α -Fe₂O₃ thin films, and Table 4.3 lists the elements that contributed to the spectra. It is clear that the iron weight percentage decreases and the oxygen weight percentage marginally rises when the Al concentration is increased. In addition to the peaks ascribed to the glass substrate, this analysis shows numerous peaks corresponding to the predicted elements like Fe, O, and Al, confirming no contaminants in the synthesized films. Adding Al caused a decrease in the [Fe]/[O] elemental ratio, which is explicable by the Fe³⁺ ions being replaced by Al³⁺ ions in the α -Fe₂O₃ lattice. P.D. More et al. [167] reported similar studies on Al-doped Fe₂O₃.

Table 4.3: Elemental composition of Al-doped α -Fe₂O₃ thin films annealed at 450°C

Al%	Atomic (%)				
	Fe	O	Al	[Fe]/[O]	[Al] / [Fe]
0	50.62	27.74	0	182	-
5	43.03	34.65	1.88	124	4.3
10	43.62	33.06	2.36	132	5.4
15	40.72	34.60	3.43	118	8.4

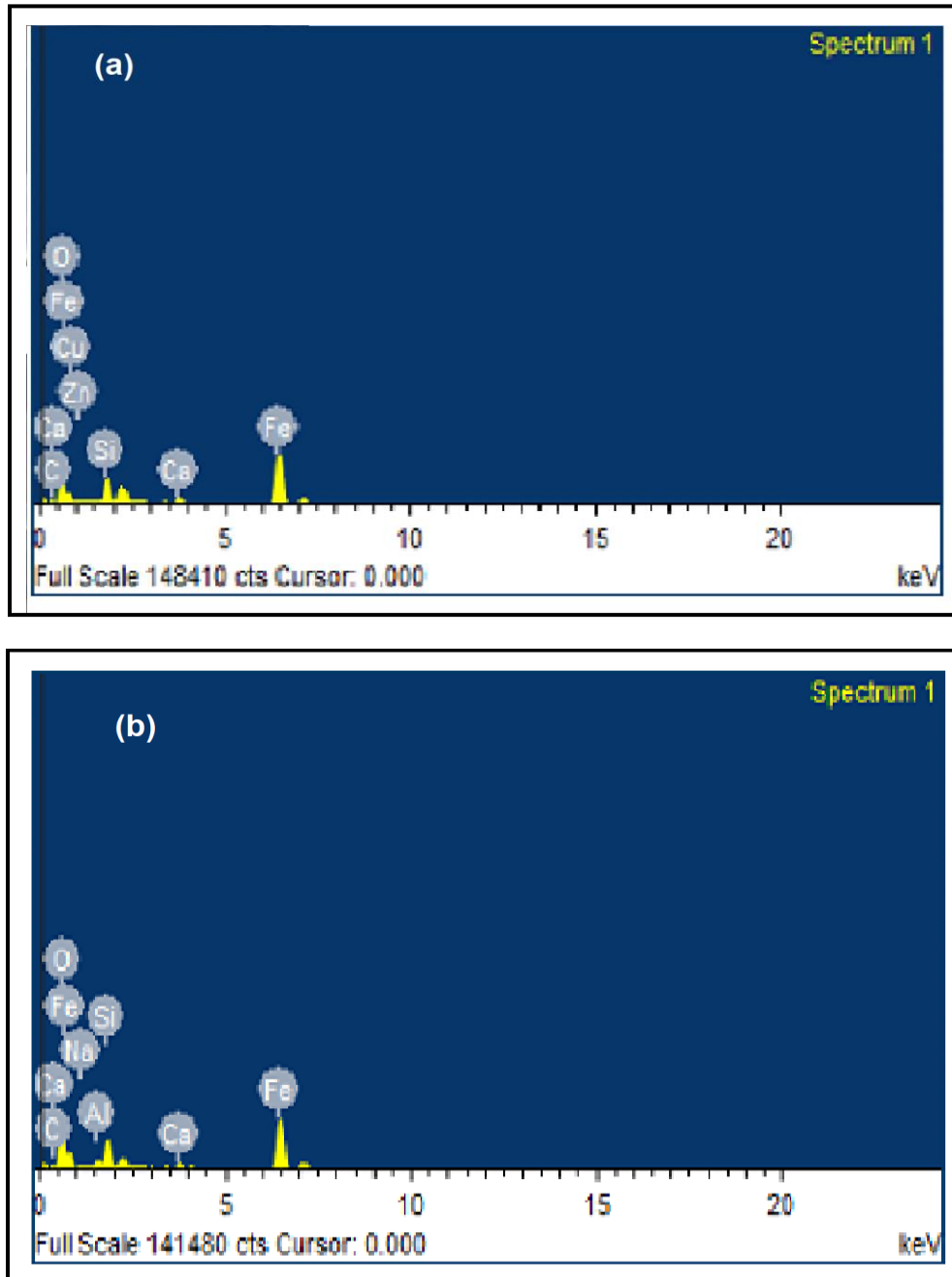


Fig.4.5: Energy dispersive X-ray spectrum of Al-doped $\alpha\text{-Fe}_2\text{O}_3$ thin films annealed at 450°C a) Pure b) 5 wt% Al

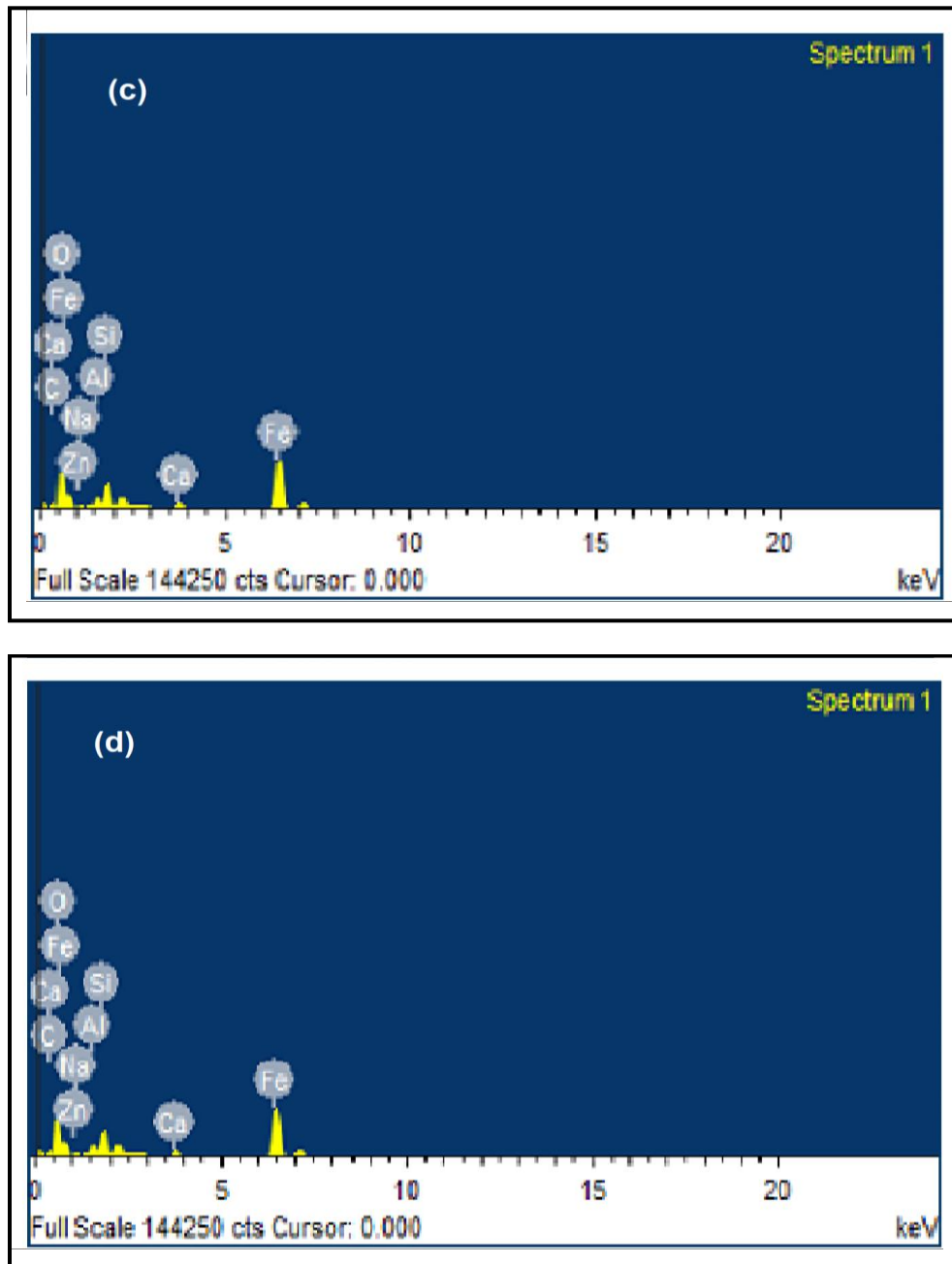


Fig.4.6: Energy dispersive X-ray spectrum of Al-doped $\alpha\text{-Fe}_2\text{O}_3$ thin films annealed at 450°C c) 10 wt% Al d) 15 wt% Al

4.2.4. Atomic force microscope studies

AFM was utilized to analyze the morphology and surface topography of pure and Al-doped $\alpha\text{-Fe}_2\text{O}_3$ thin films. Figure 4.7 displays 3-D AFM images of the films. The samples showed evenly dispersed and agglomerated grains of various sizes with a rough surface. A significant fraction of oxygen molecules has adsorbed on the surface of the films; this is helpful for gas detection [165]. The absence of cavities and cracks on the surface layers validates the FESEM results and attests to the superiority of the developed thin films.

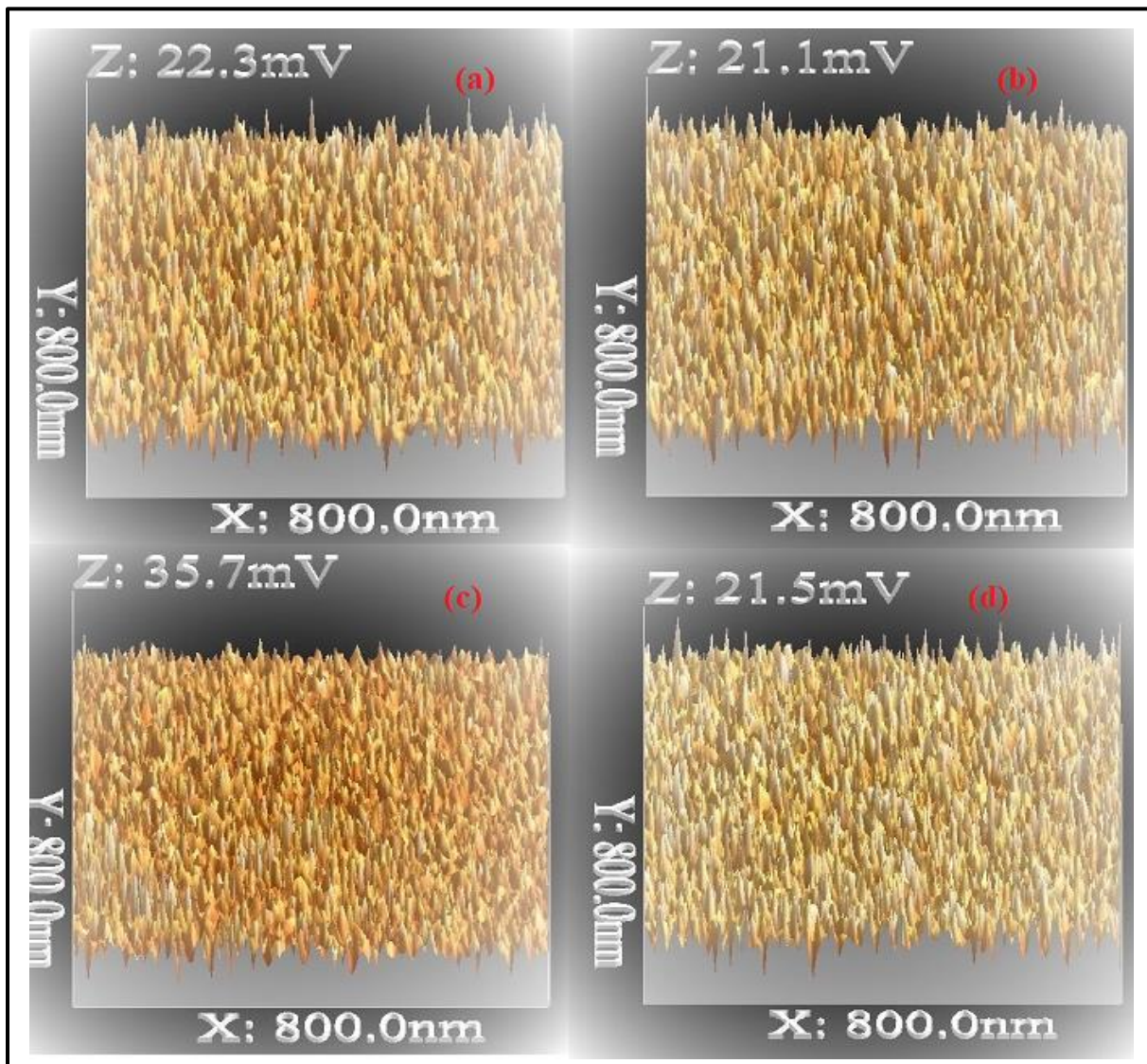


Fig.4.7: AFM 3-D pictures of Al-doped $\alpha\text{-Fe}_2\text{O}_3$ thin films annealed at 450°C a) Pure b) 5 wt% Al c) 10 wt% Al d) 15 wt% Al

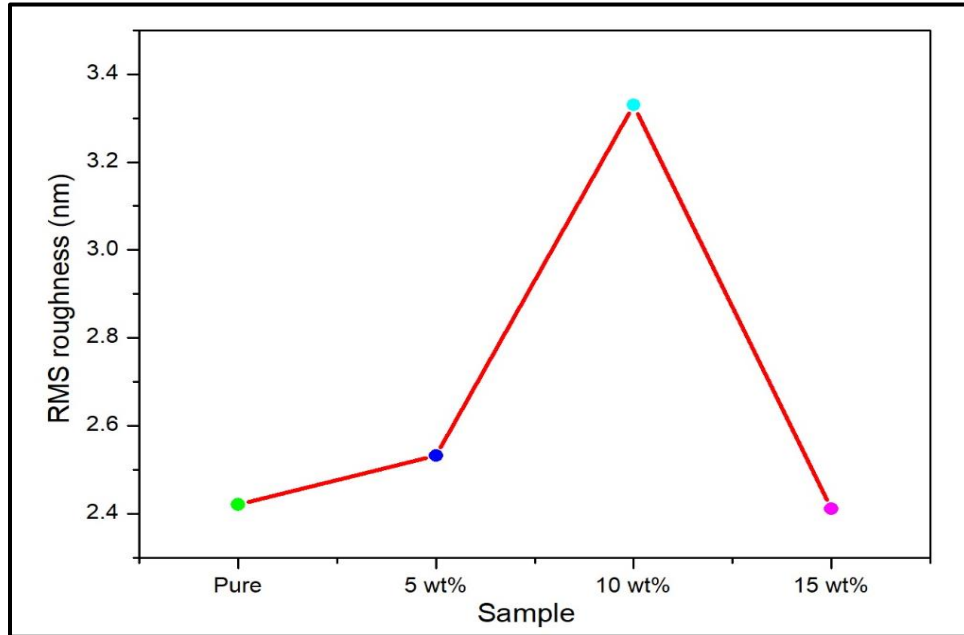


Fig. 4.8: RMS roughness of pure and Al-doped $\alpha\text{-Fe}_2\text{O}_3$ thin films annealed at 450°C

The surface roughness of the thin film is critical for gas-sensing properties since rougher surfaces may have more protrusions. This is because high grain boundary density increases surface area for the adsorption of gas molecules, which increases sensitivity [172]. The RMS roughness of the sample, which was calculated using the Nanoscope E tool, is shown in Figure 4.8 for both pure and Al-doped $\alpha\text{-Fe}_2\text{O}_3$ samples. The sample of 10 wt% Al-doped Fe_2O_3 is rougher than other samples.

4.2.5. Raman spectroscopic studies

Figure 4.9 displays the Raman spectra of pure and Al-doped $\alpha\text{-Fe}_2\text{O}_3$ thin films captured at ambient temperature. Four optical modes were seen in the spectra corresponding to 218 cm^{-1} , 279 cm^{-1} , 390 cm^{-1} , and 588 cm^{-1} . The measured Raman spectra's frequency values match with those previously reported $\alpha\text{-Fe}_2\text{O}_3$ in the literature [173]. Peaks are slightly shifted when the Al doping concentration increases due to the lattice distortion. There was no discernible signal from the other phases.

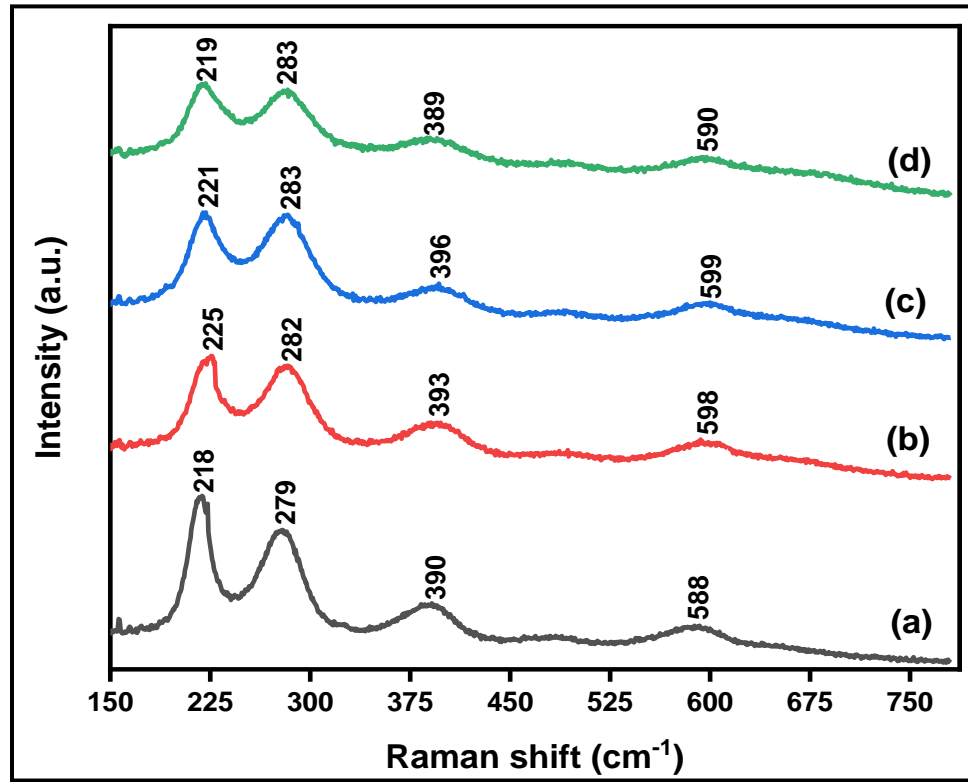


Fig. 4.9: Raman spectra of Al-doped α -Fe₂O₃ thin films annealed at 450°C a) Pure b) 5 wt% Al c) 10 wt% Al d) 15 wt% Al

4.2.6. X-ray photoelectron spectroscopy studies

Pure and Al-doped α -Fe₂O₃ films were studied using XPS to identify the chemical oxidation states of the constituent elements. Figure 4.10 displays the Fe 2p spectra of pure and Al-doped thin films. Fe2p_{3/2} and Fe2p_{1/2} levels measured binding energies at 710 and 723.5 eV, respectively. The energy difference of 13.5 eV between Fe2p_{3/2} and Fe2p_{1/2} levels precisely aligns with the previously published values of α -Fe₂O₃ [174]. In figure 4.11 two peaks can be seen in the oxygen 1s spectrum, one at 529.1 eV and the other at 531.2 eV. The peak at 529.1 eV matches the one in α -Fe₂O₃ [174], while the peak at 531.2 eV suggests a novel habitat for oxygen atoms. Due to the strong bond between O and Fe atoms, the most important peak for oxygen may be related to the special coordination configuration of Fe suggested by the shoulder near the Fe 2p_{3/2} main peak. Thus, the chemical states of iron in Fe³⁺ and oxygen in O²⁻ confirmed the creation of α -Fe₂O₃. XRD studies have already shown the development of α -Fe₂O₃ in these samples.

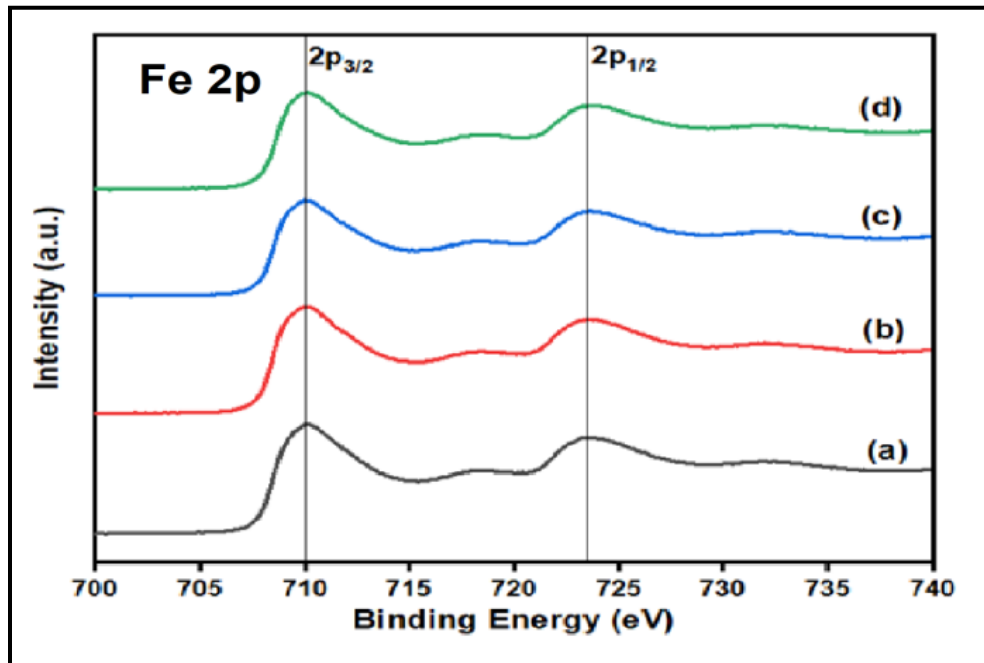


Fig. 4.10: Fe 2p spectra of pure and Al-doped α - Fe_2O_3 thin films annealed at 450°C a) Pure Fe_2O_3 b) 5 wt% Al c) 10 wt% Al d) 15 wt% Al

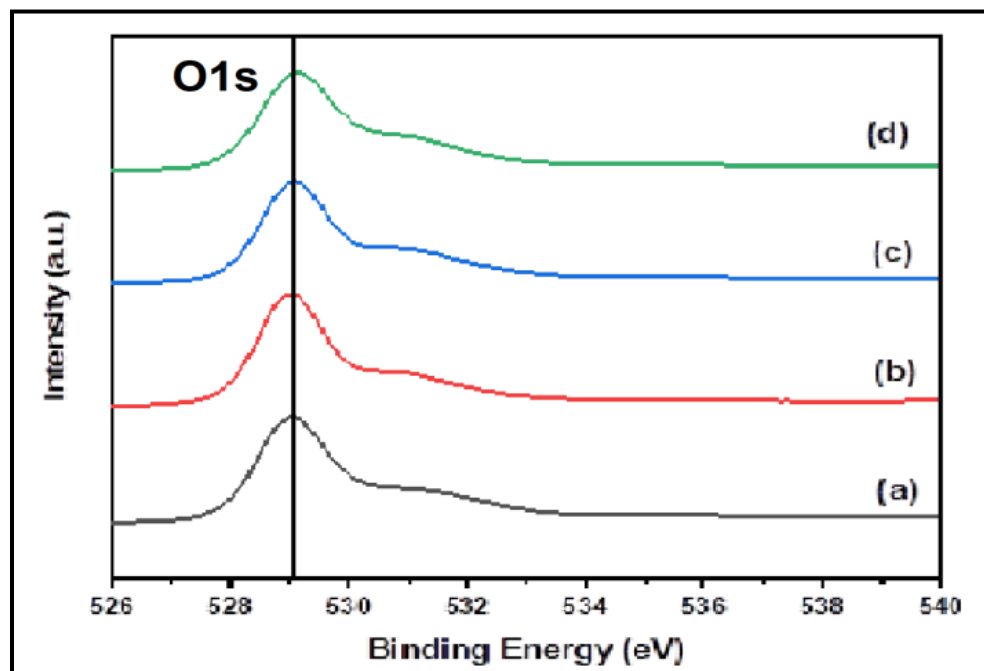


Fig. 4.11: O 1s spectra of pure and Al-doped α - Fe_2O_3 thin films annealed at 450°C a) Pure Fe_2O_3 b) 5 wt% Al c) 10 wt% Al d) 15 wt% Al

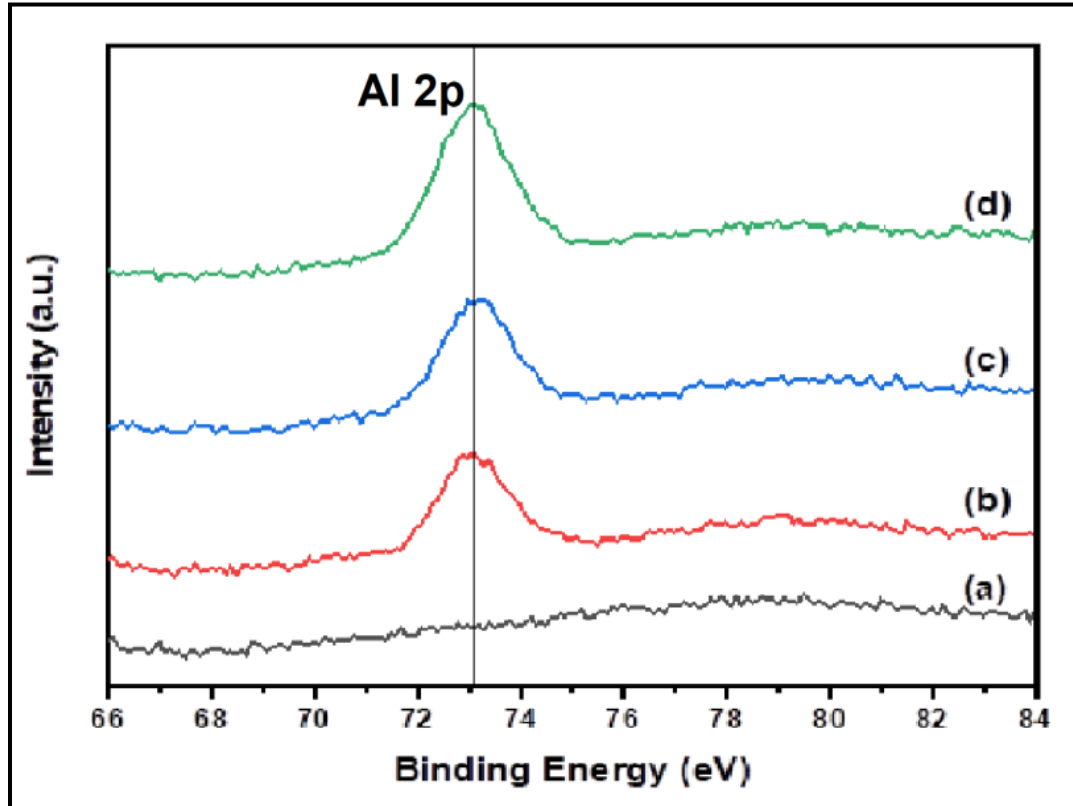


Fig. 4.12: Al 2p spectra of pure and Al-doped α -Fe₂O₃ thin films annealed at 450°C a) Pure Fe₂O₃ b) 5 wt% Al c) 10 wt% Al d) 15 wt% Al

Figure 4.12 displays the Al 2p spectra of pure and Al-doped α -Fe₂O₃ thin films annealed at 450°C, at 73 eV, Al2p_{1/2}'s peak location has been determined [174]. The XPS investigation demonstrates that no peak shifts were seen as the Al doping content was raised.

4.2.7 Optical properties

The optical characteristics of the pure and Al-doped α -Fe₂O₃ thin films annealed at 450°C were studied using a U.V. Visible spectrophotometer at room temperature. The Beer-Lambert law relation is used to compute the absorption coefficient for each sample [165]:

$$\text{Absorption coefficient } \alpha = \frac{A}{t}$$

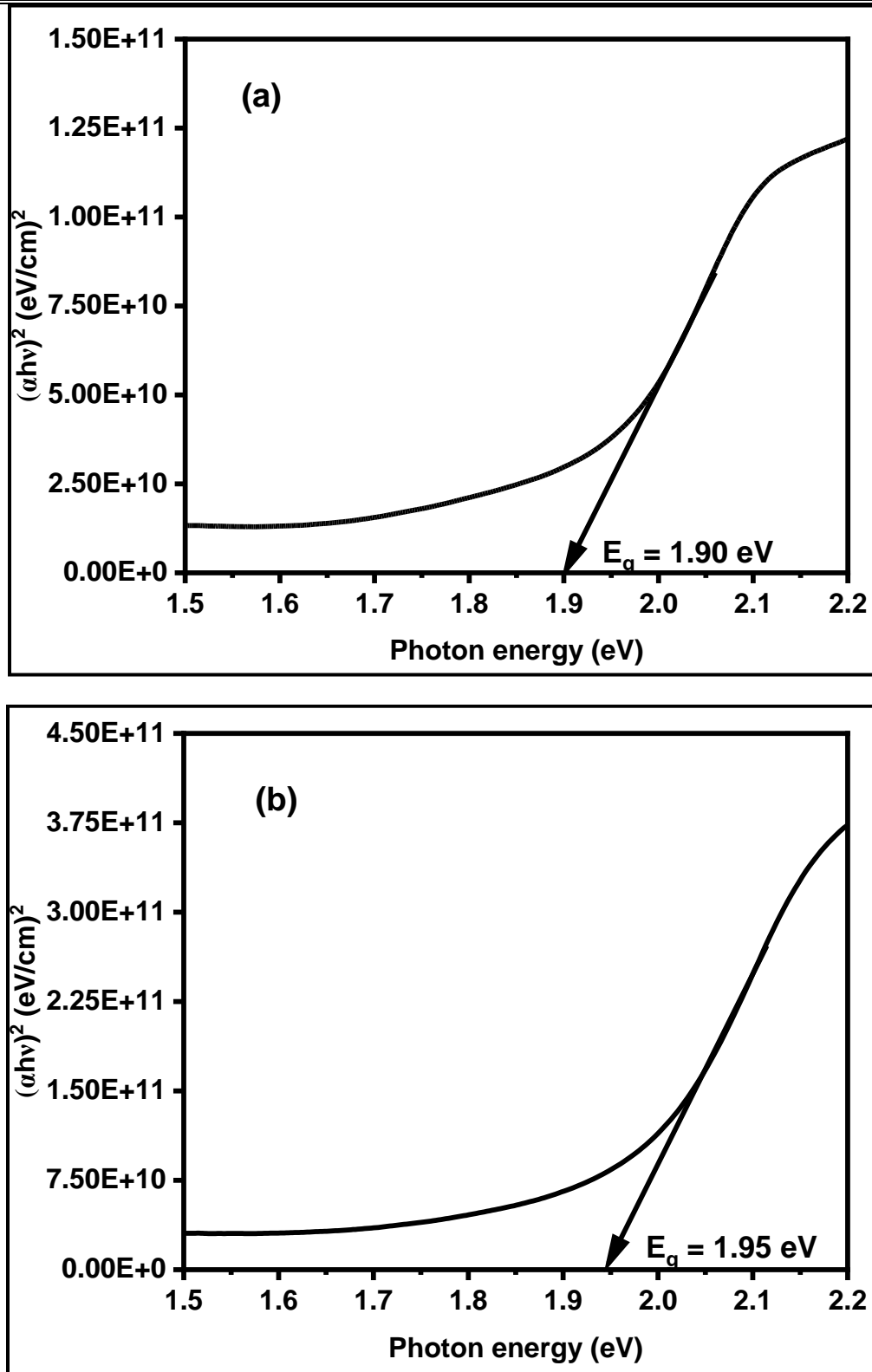


Fig. 4.13: Tauc plots for Al-doped $\alpha\text{-Fe}_2\text{O}_3$ thin films annealed at 450°C a) Pure b) 5 wt% Al

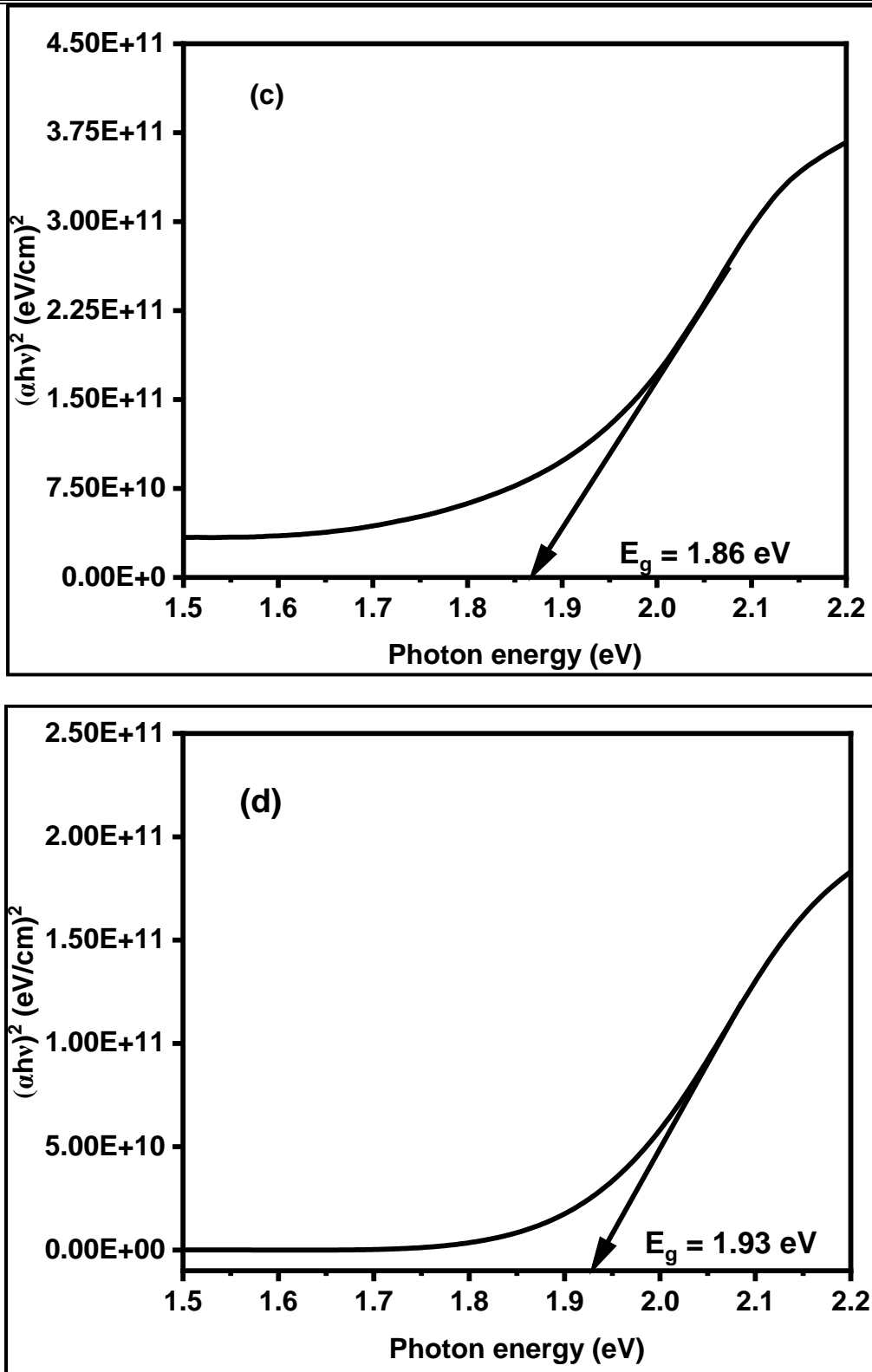


Fig. 4.14: Tauc plots for Al-doped $\alpha\text{-Fe}_2\text{O}_3$ thin films annealed at 450°C c) 10 wt% Al d) 15 wt% Al

Chapter-4 Synthesis and characterization of Al-doped Fe₂O₃ thin films for formaldehyde gas sensing application

where t is the film's thickness, and A is the absorbance. The optical band gaps of thin films are calculated by Tauc plot using the following relation [175]:

$$\alpha h\nu = C(h\nu - E_g)^n$$

where n is taken as 2 by considering that α -Fe₂O₃ possesses an indirect band gap [176] and h , ν , and E_g are Planck's constant, photon frequency, and optical band gap, respectively. The value of the optical bandgap (E_g) is displayed in Figure 4.13 and figure 4.14. It is obtained by extrapolating the linear region of a plot of photon energy and $(\alpha h\nu)^2$ on the Y-axis against the X-axis value of photon energy. The obtained band gap values are 1.90, 1.95, 1.86, and 1.93 eV for pure, 5wt%, 10 wt%, and 15wt% Al-doped α -Fe₂O₃ thin films, respectively. These values are consistent with those previously reported, and the variation in band gap with the Al doping is caused by a change in the size of the crystallites in the layer [167,173].

4.3. Gas-sensing characterization

Using a high resistance electrometer (Keithely-6517B), the gas sensing capabilities of the thin films of pure and annealed Al-doped α -Fe₂O₃ were examined. All the sensors were tested for ethanol, methanol, acetone, formaldehyde, xylene, toluene, and benzene at room temperature (27°C). In the current study, the sensor (S) sensitivity, computed using the relation [177], establishes the gas-detecting capabilities.

$$\text{Sensitivity (S)} = \frac{R_a - R_g}{R_g} \times \%$$

R_a and R_g represent the sensor's resistance in air and gas, respectively. Among all the sensors, 10 wt% of the Al-doped α -Fe₂O₃ sensor showed the highest degree of formaldehyde selectivity with a sensitivity of 19 % to 5 ppm concentration at room temperature. Figure 4.15 illustrates the formaldehyde sensitivity behaviour of all the developed sensors. Due to Al doping in the α -Fe₂O₃ lattice, the sensor's sensitivity was 15% and 19% to the doping levels of 5 and 10 wt% of Al, respectively. After that, sensitivity decreased to 15.7% towards formaldehyde gas at 5ppm concentration as the doping level increased to 15 wt% of Al. At a gas concentration of 5 ppm, however, none of the remaining test gases displayed comparable sensitivity. At lower temperatures, the HCHO band is significantly less than other gases, with just 364 kJ/mol. As a result, the formaldehyde's bond dissociation energies are easily broken to take part in the

chemical adsorption reaction with the sensing material. Other gases would certainly resist response at lower temperatures, but due to their high bonding energy, they would exhibit less appropriate responses [178]. Further research was done as a result by taking formaldehyde selectivity into account.

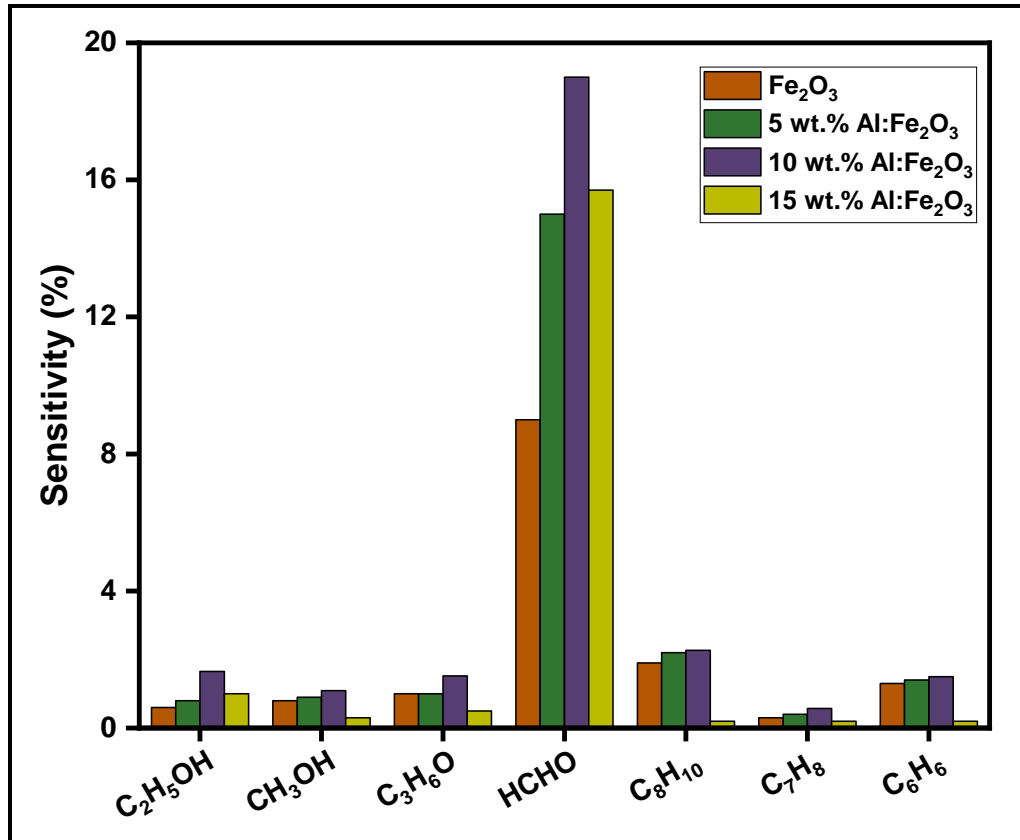


Fig. 4. 15: Sensitivity of Al-doped $\alpha\text{-Fe}_2\text{O}_3$ thin films annealed at 450°C towards different gasses of 5ppm concentration tested at room temperature (27°C).

4.3.1 Response and Recovery Properties

One of the key sensor properties for the practical usability of the annealed pure and Al-doped $\alpha\text{-Fe}_2\text{O}_3$ sensors is the transient response, shown in Figures 4.16 and 4.17. The transient response curve shows the resistance's rise and fall patterns in the presence and absence of formaldehyde vapour at 5 ppm at ambient temperature. When exposed to test gas, the sensor's response time refers to the time it takes to reach 90% of its saturation resistance. In contrast, the recovery time is the time it takes for the sensor to reach 10% saturated resistance after the test gas withdrawal. The transient response curves indicate that the determined response and

Chapter-4 Synthesis and characterization of Al-doped Fe₂O₃ thin films for formaldehyde gas sensing application

recovery periods are low to 10% of the Al-doped sensor. One of the key sensor properties for the practical usability of the annealed Al-doped α -Fe₂O₃ sensors is the transient response. According to FESEM and XRD results, spherical particles that are less interfered with and less agglomerated have higher surface activity [179], which may lead to a more significant interaction between the formaldehyde molecules and active surface sites, which is why the determined value of the highest response to a 10 wt% Al-doped α -Fe₂O₃ sensor can be attributed to these factors.

The gas sensing measurements were repeatedly measured at regular intervals to confirm the stability and repeatability of 10 wt% of the Al-doped α -Fe₂O₃ sensor. The sensor performance was examined more than a month after the first measurement with the 3-day interval shown in Figure 4.18, maintaining the measurement parameters unchanged. The sensor demonstrated over 90% of its initial sensitivity, demonstrating its viability for commercial applications as a formaldehyde sensor. Figure 4.19 illustrates the formaldehyde sensor's repeatability at 5 ppm vapours throughout the continuous operation of the target gas under the same circumstances. Through all trial cycles, the sensor's repeatability has remained essentially stable. Figure 4.20 shows the sensor sensitivity concerning the concentration of formaldehyde gas. Seven points are selected from this graphic, and the slope of the curve and the standard deviation are examined. Using these values in the LOD calculation shown in the formula below, it was estimated that the detection limit was approximately 3 ppm. [180].

$$\text{LOD} = 3 \times \frac{\text{Standard deviation}}{\text{Slope}}$$

4.3.2. Formaldehyde gas sensing mechanism

The α -Fe₂O₃ sensor's gas-sensing mechanism is chemical adsorption and desorption of the reactive gas molecules on the sensor surface. [166,167]. Figure 4.21 displays a schematic illustration of the formaldehyde sensor system. The gas-detecting mechanism of the Al-doped α -Fe₂O₃ sensor can be understood by the oxygen adsorption on the sensor's surface, and the interactions of the gas molecules adsorbed on it [159]. As soon as the sensor is exposed to air, the oxygen molecules in the air chemisorbed on the surface of the detecting material. The oxygen molecules in this scenario change into chemisorbed oxygen species (O₂⁻, O⁻, or O²⁻) by luring electrons from the α -Fe₂O₃'s conduction band, as seen in Figure 4.21(a). The test gas influences

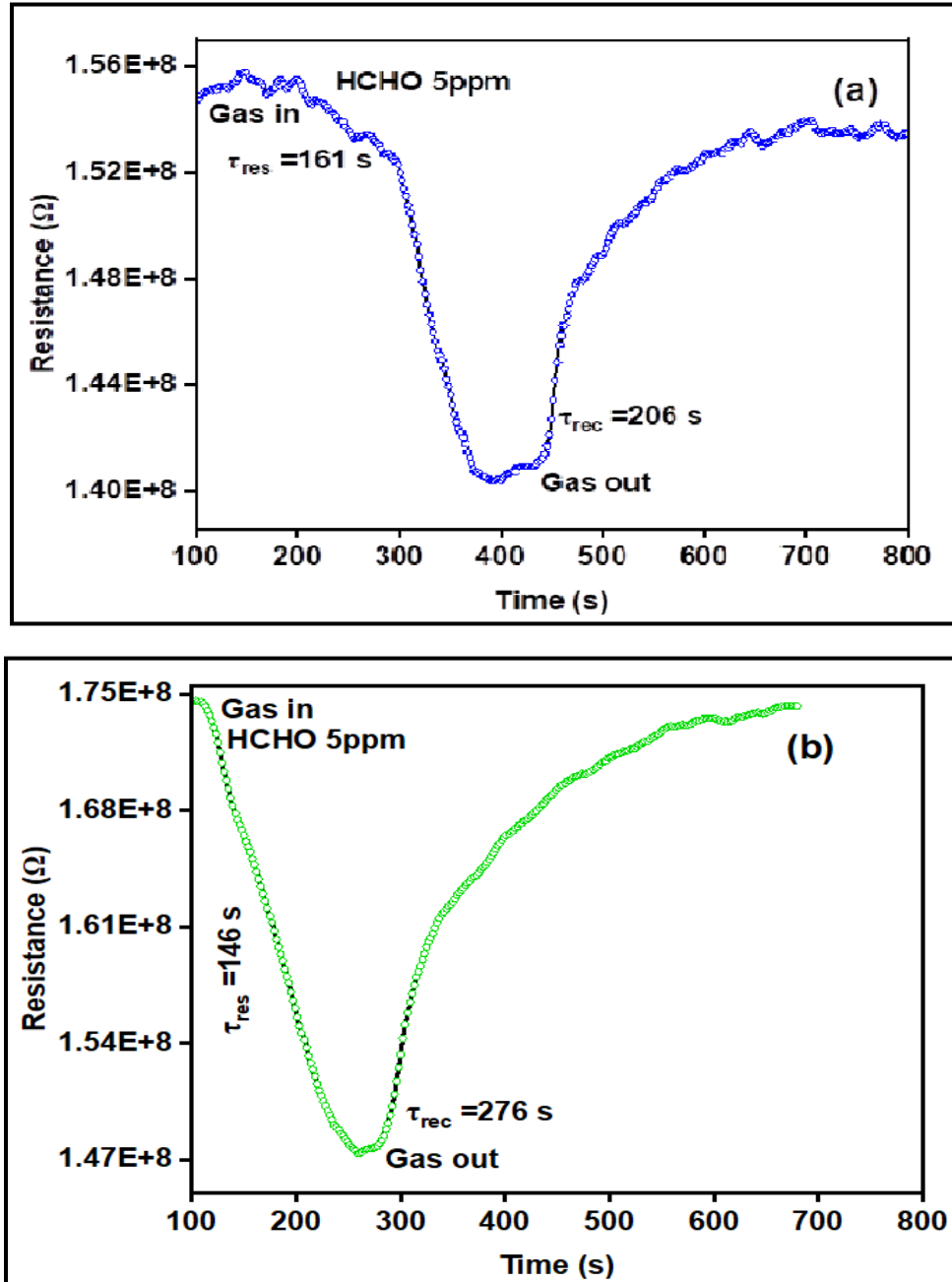


Fig.4. 16: Transient response curve of pure and Al-doped $\alpha\text{-Fe}_2\text{O}_3$ thin films annealed at 450°C a) Pure b) 5 wt% Al

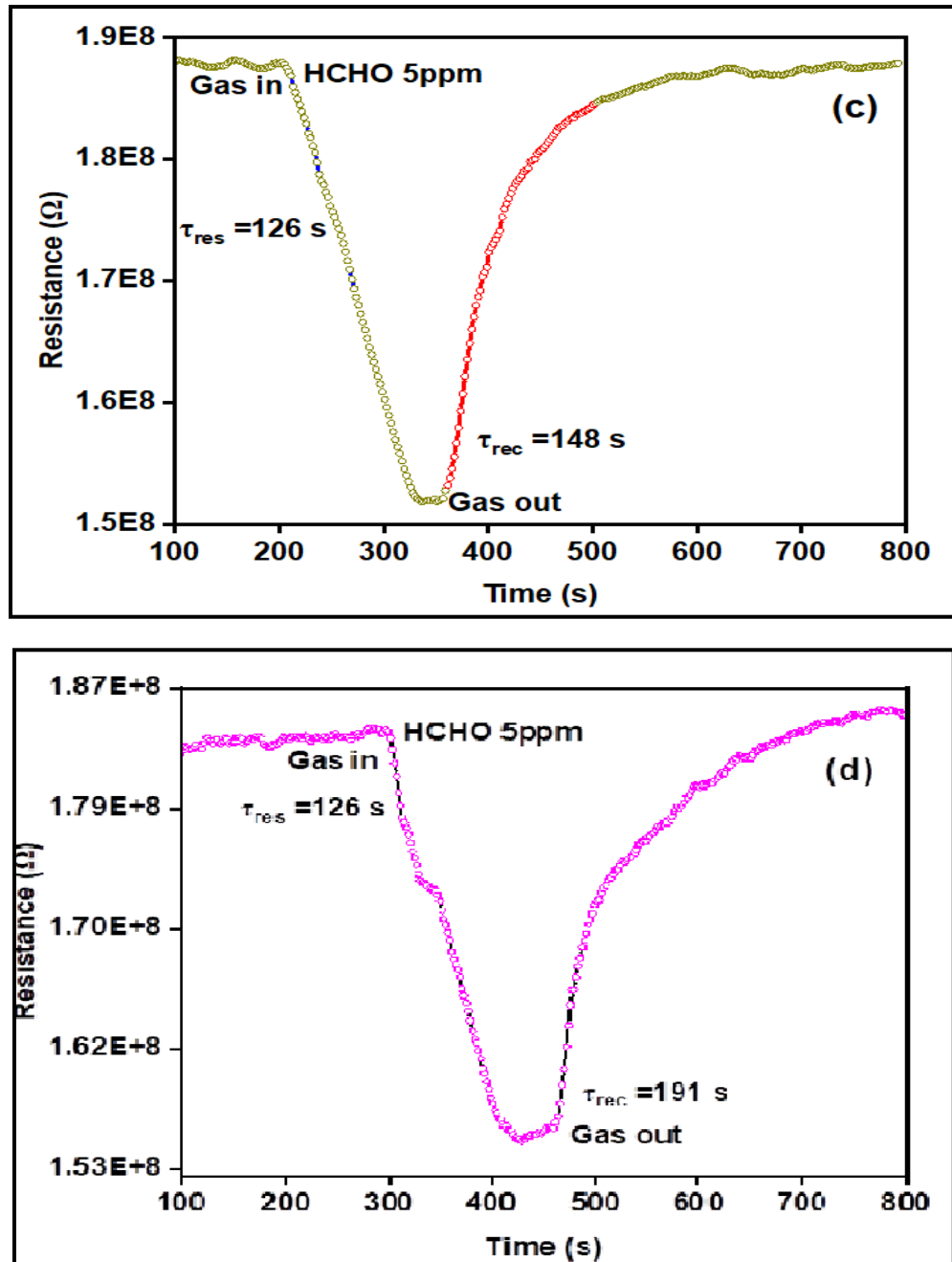


Fig. 4. 17: Transient response curve of pure and Al-doped $\alpha\text{-Fe}_2\text{O}_3$ thin films annealed at 450°C c) 10 wt% Al d) 15 wt% Al

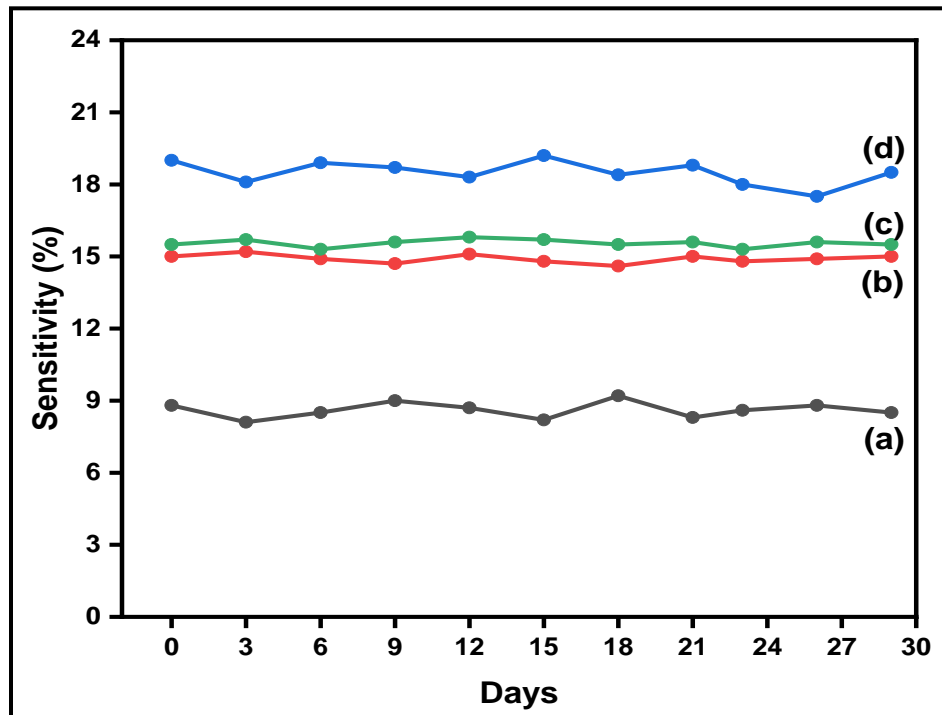


Fig. 4. 18: Stability of Al-doped $\alpha\text{-Fe}_2\text{O}_3$ thin films annealed at 450°C a) Pure b) 5 wt% Al c) 15 wt% Al, d) 10 wt% Al

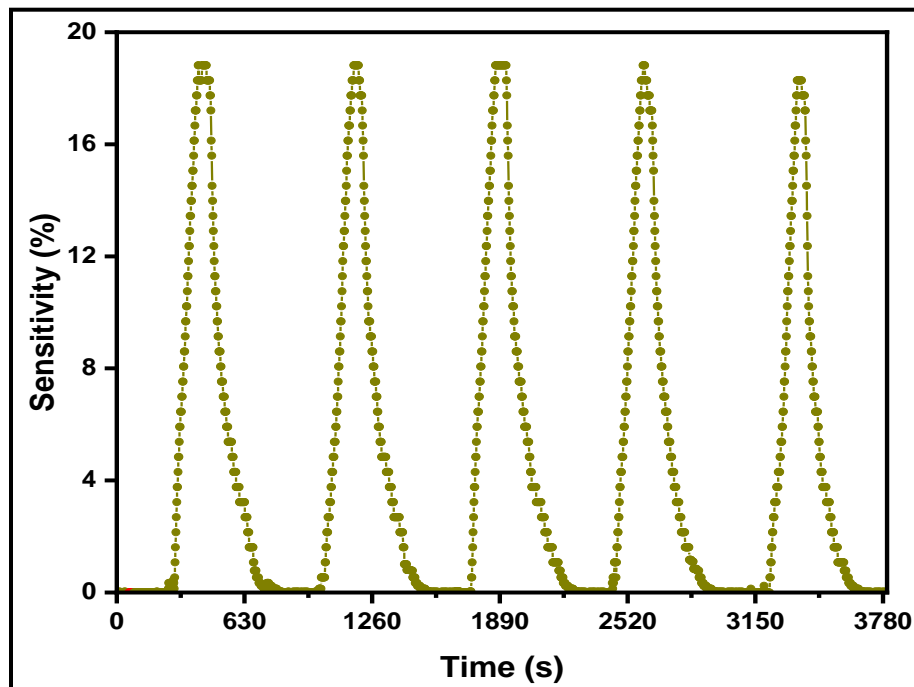


Fig. 4. 19: Repeatability of 10 wt% Al-doped $\alpha\text{-Fe}_2\text{O}_3$ thin film annealed at 450°C and tested at room temperature towards 5ppm formaldehyde gas

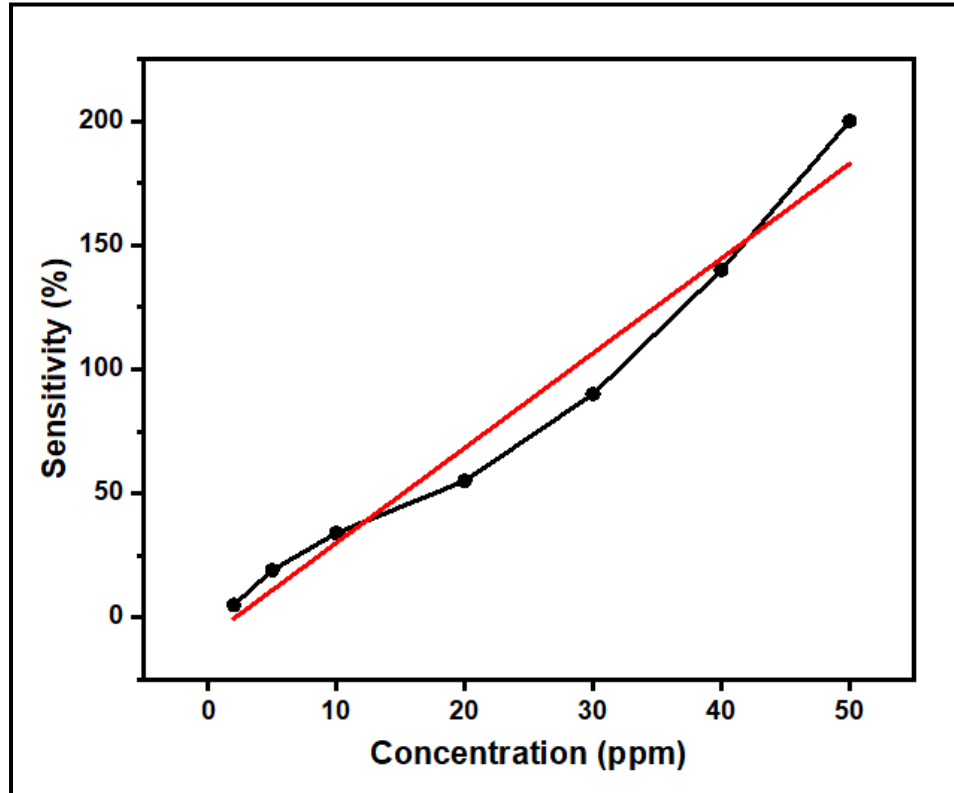
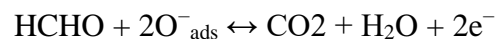
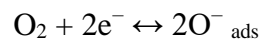


Fig. 4. 20: Sensitivity variation at different concentrations of formaldehyde towards 10 wt% Al-doped α -Fe₂O₃ thin film annealed at 450°C

the oxygen species adsorbed on the surface when formaldehyde is delivered into the chamber. Due to this, the number of surface O₂⁻, O⁻ and O²⁻ species are reduced, and the conduction band's electron density is increased, which lowers the resistance of α -Fe₂O₃ as shown in figure 4.21(b).

At low temperatures, O₂⁻ predominates, whereas, at high temperatures, O and O²⁻ exist in great abundance [180]. The following chemical reactions are suggested by the responses:



Due to the high surface area of tiny particles, which further increases the amount of chemisorbed oxygen ions, doping may improve gas sensing. Additionally, Al doping in α -Fe₂O₃ results in point defects and alters the oxide's surface.

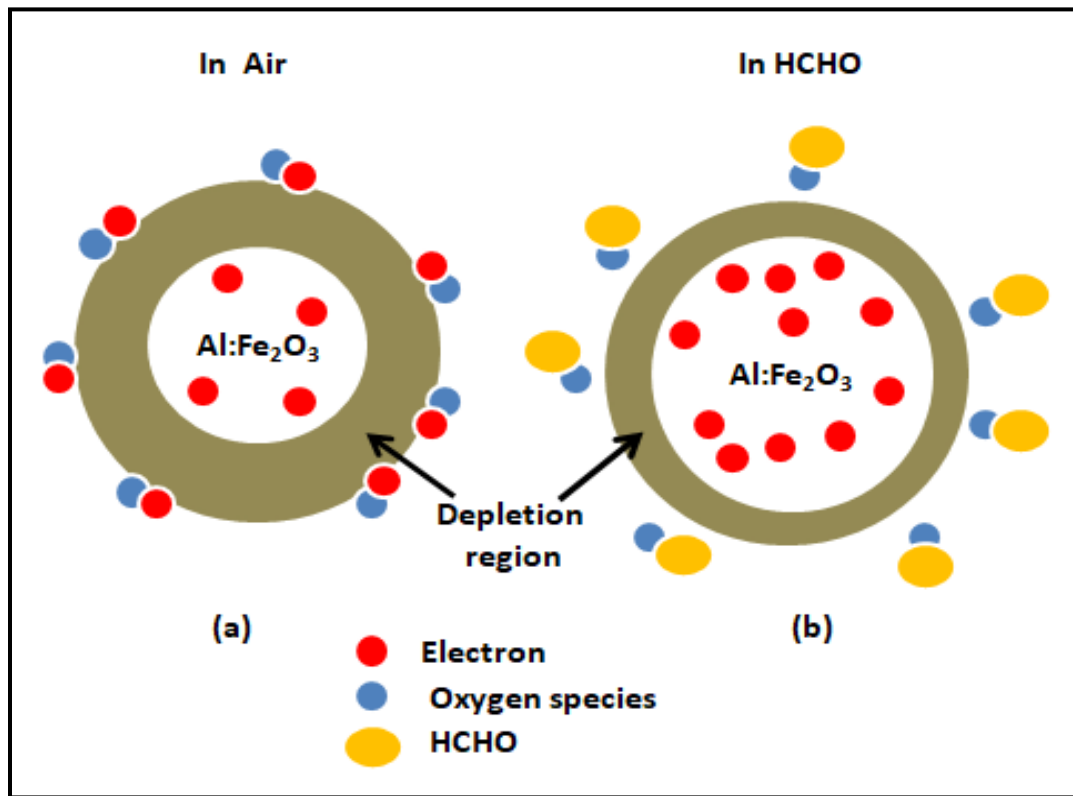


Fig. 4. 21: Formaldehyde sensing mechanism of Al-doped α -Fe₂O₃ sensor

4.4 Summary

Pure and Al-doped α -Fe₂O₃ based formaldehyde sensors were prepared by a low-cost and affordable spray pyrolysis method with 5, 10, and 15 wt % of Al-doping concentrations at 375 °C. XRD results confirm the poor phase formation of as-deposited films. Hence, these samples were annealed at 450 °C as they have shown good crystalline nature. The average crystallite size of the 10 wt% Al-doped α -Fe₂O₃ thin film is 65.1 nm, demonstrating the production of a polycrystalline behaviour with a rhombohedral structure with a predominate orientation of (104) and improved crystallinity. The morphology of the samples was studied with FESEM and AFM techniques. All the thin films have uniform surface morphology with agglomerated superimposed sphere-like particles, and the superimposition of the particle is low in the case of 10 wt% Al-doped α -Fe₂O₃ samples when compared to pure, 5 and 15 wt% Al-doped α -Fe₂O₃ thin films. The chemical composition of the thin films was confirmed with EDX, Raman, and XPS techniques, and no impurity phase was found. No peak shifts were observed in XPS spectra.

Chapter-4 Synthesis and characterization of Al-doped Fe₂O₃ thin films for formaldehyde gas sensing application

Raman spectra show peaks were slightly up due to lattice disturbance as the Al doping concentration increases. The optical energy band gap values were regarded as 1.90, 1.95, 1.86 and 1.93 eV for pure, 5, 10 and 15 wt% Al-doped thin films, respectively; this variation may be due to the change in particle size as they were agglomerated super imposed particles. Amongst all the sensors, the 10 wt% Al-doped α -Fe₂O₃ sensor showed the highest sensitivity and lowest response and recovery times towards 5ppm formaldehyde at ambient temperature compared to other sensors. Finally, these results revealed that the best way to prepare low-cost iron oxide-based formaldehyde gas sensors that can be operated at room temperature shows considerable promise for detecting formaldehyde gas. It can be a potential candidate for industrial applications.

5.1. Summary and conclusions

The current work's objectives were to deposit and analyze thin films of metal oxide semiconductor (Iron oxide) and to examine how well they performed in the detection of volatile organic compounds (VOCs). VOCs are gases that are released into the atmosphere by-products or operations. Some, such as those that cause cancer, are dangerous on their own.

Almost all aspects of material science and physics, including superconductivity and magnetism, are covered by the diverse and stunningly attractive class of materials known as metal oxides. Metal oxides span from metals to semiconductors to insulators. It has been well established in the field of chemical sensing for more than 50 years that semiconductors' electrical conductivity varies depending on the chemical composition of the gas atmosphere around them.

Many fields, including environmental monitoring, personal safety, public security, automotive applications, and air conditioning in homes, spacecraft, and aircraft, greatly benefit from the usage of gas sensors. This broad range of applications has increased the demand for solid state gas sensors that are affordable, portable, power-efficient, and dependable.

A literature review was used to provide the backdrop of the issue in the thesis' introductory chapter. The inspiration for the study was primarily covered in this chapter. The different potential uses for metal oxide semiconductors have been uncovered. It was also described how several processes have been used to create Fe_2O_3 thin films. In this chapter, the basic material Fe_2O_3 was endowed with its structural, optical, and gas sensing capabilities. In the reviewed literature, the author discussed the techniques used to dope iron oxide. Using the literature that was available, the history of thin film technology was also comprehended. The authors went into detail about current studies of the iron oxide's regulating properties. This chapter assessed recent publications on Fe_2O_3 -based gas sensing, presented the research problem's objective and approach.

In the second chapter, there is discussion of the experimental techniques and characterization techniques used during the investigation. Using the spray pyrolysis technique, iron oxide thin films were synthesized. The production of $\alpha\text{-Fe}_2\text{O}_3$ utilized all chemical salts of AR grade. Film preparation utilized the glass substrates (Blue Star). There was a thorough discussion of every aspect of the spray pyrolysis technique used to make thin films. The chapter

also covered the theory, operation, and application of characterization techniques like x-ray diffraction (XRD), scanning electron microscopy (SEM), energy dispersive spectroscopy (EDS), raman spectroscopy, X-ray photo electron spectroscopy (XPS), atomic force microscope (AFM), UV-visible spectroscopy, and static gas sensing apparatus analysis. There was also discussion of the benefits and drawbacks of different characterization techniques. There was also discussion of all the theories and formulas that were used to calculate different parameters such as crystallite size, specific surface area, film thickness, resistivity, gas sensitivity, and gas selectivity. The chapter contains all the information on the instruments utilized for the study.

The third chapter included the preparation of pure α -Fe₂O₃ thin films as well as their research's findings. The pure α -Fe₂O₃ thin films' structural, morphological, optical, and gas sensing characteristics have been thoroughly addressed. Fe(NO₃)₃·9H₂O, a starting material purchased from Sigma Aldrich (India), was diluted to 0.1M in 40 ml of de-ionized water. At substrate temperatures of 375°C, 400°C, and 425°C, spray pyrolysis was used to produce the Fe₂O₃ thin films on glass substrates. After the deposition, the films were allowed to cool to room temperature. Studies on deposited thin films using X-ray diffraction have revealed their polycrystalline nature with rhombohedral structure matched with JCPDF Card No. 84-0311 and highly oriented along (104) direction. Intensity of the peak corresponding to (104) plane was found to be decreased with an increase in the substrate temperature from 375°C to 425°C. The results of the morphological investigations suggest that the uniform cuboid-shaped nano crystals present in the thin film, which are an extremely suitable morphology for chemiresistive gas sensing experiments. An energy dispersive X-ray spectrum confirms good stoichiometry of the prepared α -Fe₂O₃ films.

AFM surface characterization showed that the substrate temperature had a significant impact on the microstructure of the films during the deposition process. The surface of the film that was deposition at 375°C is significantly rougher than other films. Because there are more active oxygen adsorption sites on the sensor surface, it is well known that raising the surface roughness of the film improves the sensor element's ability to detect gases. Optical studies of the deposited thin films showed that optical band gap was increased as substrate temperature is increased. The results of continuous short-term studies utilizing 5 ppm of ammonia over a period

of 18 days in gas sensing have demonstrated a stable response with outstanding sensitivity and selectivity. Response and recovery times were measured at 40 and 56 seconds, respectively.

Table 5.1: Summarized results concerning the deposition, characterization results and gas responses of α -Fe₂O₃ films.

S.No	Substrate Temperature (°C)	Crystallite size (nm)	No. of crystallites per unit area (10^{16} m^{-2})	Roughness (nm)	Optical band gap (eV)	Response to NH ₃ towards 5ppm (R_a/R_g)
1	375	33.34	1.04	139	2.80	46.5
2	400	27.96	2.59	104	2.84	36
3	425	14.45	8.08	16.2	2.88	28

The fourth chapter covered the structural, morphological, optical, and gas sensing characteristics of films made of aluminum-doped α -Fe₂O₃. With 5, 10, and 15 wt% of Al-doping concentrations at 375 °C, spray pyrolysis was used to create low-cost and accessible Al-doped - α -Fe₂O₃ thin films. The poor phase formation of as-deposited films is confirmed by XRD data. Since these samples had a good crystalline character, they were annealed at 450 °C. The 10 wt% Al-doped α -Fe₂O₃ thin film's average crystallite size is 65.1 nm, exhibiting the creation of polycrystalline behavior with a rhombohedral structure that matches JCPDF card No. 84-0311 and increased crystallinity. While raising the concentration of Al to 10% caused the preferred orientation of the resulting α -Fe₂O₃ to be in the (104) plane, Less intense peaks were seen at 20.1°, 45.5°, and 67.6°, which are in agreement with JCPDF card No. 89-7047 and correspond to the (110), (042), and (252) Miller planes of the Fe₂O₃ phase. In the case of 15 weight percent Al-doped α -Fe₂O₃ thin films, the peaks corresponding to the (012), (113), (024), (116), and (1010) planes of the α -Fe₂O₃ phase vanished, and the intensity of other peaks was reduced. Through the use of FESEM and AFM methods, the samples' morphology was investigated. In comparison to pure, 5 and 15 wt% Al-doped α -Fe₂O₃ thin films, the superimposition of the particle is low in the 10 wt% Al-doped α -Fe₂O₃ samples. All the thin films show uniform surface morphology with agglomerated superimposed sphere-like particles. Using EDX, Raman, and XPS techniques, the

chemical composition of the thin films was validated, and no impurity phase was discovered. Furthermore, no peak shifts were seen in the XPS spectra. As the Al doping concentration rises, the lattice disturbance in the Raman spectra causes the peaks to be somewhat higher. For pure, 5, 10, and 15 wt% Al-doped thin films, the optical energy band gap values were determined to be 1.90, 1.95, 1.86, and 1.93 eV, respectively; this variation may be caused by the change in particle size when they were agglomerated over particles. The 10 wt% Al-doped α -Fe₂O₃ sensor outperformed the other sensors in terms of sensitivity to 5 ppm formaldehyde at ambient temperature as well as response and recovery times. The optimum method for creating low-cost, room-temperature operable iron oxide-based formaldehyde gas sensors was demonstrated by these results, and it has great potential for formaldehyde gas detection.

Table 5.2: Summarized results concerning characterization results and gas responses of Al doped α -Fe₂O₃ films deposited at 375°C, annealed at 450°C.

S.No	Al concentration (wt%)	Crystallite size (nm)	No. of crystallites per unit area (10^{19} m^{-2})	Roughness (nm)	Optical band gap (eV)	Response to HCHO towards 5ppm (%)
1	0	11.87	0.10	2.42	1.90	9
2	5	10.26	0.22	2.51	1.95	15
3	10	65.1	0.11	3.51	1.86	19
4	15	7.34	30.7	2.4	1.93	15.7

5.2. Scope for future work

It is expected that the following features would be directions for building highly effective poisonous gas sensors in the future based on current advancements in the field of metal oxide gas sensors.

- Managing the shape and structure of the materials used in sensors.
- Size effect, porous nanostructures, and doping's effects on nanoscale levels.

- Innovative nanostructures or nanocomposites that could enable extremely sensitive detection
- Integrating porous nanostructures with chromatographic technology and having quick responses and recovery properties.
- Study the gas sensing properties of the deposited films at different annealing time period and temperature.

Gas sensors are a subject of study in several fields, such as electronics, chemistry, and physics. Resolving those problems will be one of the main challenges, hence enhancing multi disciplinary co-operation is essential.

Bibliography

- [1]. K. Kumari, S. Ram, Sensitivity study of nano crystalline Fe₃BO₆ sensor for methane gas detection. *IEEE Sens. J.* 18, 8230–8237 (2018).
- [2]. C. Wang, L. Yin, L. Zhang, D. Xiang, R. Gao, Metal oxide gas sensors: sensitivity and influencing factors. *Sensors* 10, 2088–2106 (2010).
- [3]. S.J. Patil, A.V. Patil, V.G. Dighavkar, K.S. Thakare, R.Y. Borase, S.J. Nandre, N.G. Deshpande, R.R. Ahire, Semiconductor metal oxide compounds based gas sensors: a literature review, *Front. Mater. Sci.* 9, 14–37(2015).
- [4]. Andrea Ponzoni, Camilla Baratto, Nicola Cattabiani, Metal oxide gas sensors, a survey of selectivity issues addressed at the sensor lab, Brescia (Italy), *Sensors*, 17, 714(2017).
- [5]. J.J. Hassan, M.A. Mahdi, C.W. Chin, H. Abu-Hassan, Z. Hassan, A high-sensitivity room-temperature hydrogen gas sensor based on oblique and vertical ZnO nanorod arrays, *Sensors and Actuators B: Chemical*, 176, 360-367 (2013).
- [6]. Cuiping Gu, Xiaojuan Xu, Jiarui Huang, Weizhi Wang, Yufeng Sun, Jinhui Liu, Porous flower-like SnO₂ nanostructures as sensitive gas sensors for volatile organic compounds detection, *Sensors and Actuators B: Chemical*, 174, 31-38(2012).
- [7]. E. Brauns, E. Morsbach, S. Kunz, M. Bäumer, W. Lang, A fast and sensitive catalytic gas sensors for hydrogen detection based on stabilized nanoparticles as catalytic layer, *Sensors and Actuators B: Chemical*, 193, 895-903(2014).
- [8]. Christian Bur, Peter Reimann, Mike Andersson, Andreas Schutze, Anita Lloyd Spetz, Increasing the Selectivity of Pt-Gate SiC Field Effect Gas Sensors by Dynamic Temperature Modulation, *IEEE sensors journal*, 12, 1906 – 19139(2012).
- [9]. Bong-Hoon Jang, Osnat Landau, Seon-Jin Choi, Jungwoo Shin, Avner Rothschild, Il-oo Kim, Selectivity enhancement of SnO₂ nanofiber gas sensors by functionalization with Pt nanocatalysts and manipulation of the operation temperature, *Sensors and Actuators B*, 188, 156–168(2013).
- [10]. Sheng Yi, Shouqin Tian, Dawen Zeng, Keng Xu, Xuelian Peng, Hao Wang, Shunping Zhan, Changsheng Xie, A novel approach to fabricate metal oxide nanowire-like networks based coplanar gas sensors array for enhanced selectivity, *Sensors and Actuators B*, 204, 351-359(2014).
- [11]. R. Ramamoorthy, P. K. Dutta, S. A. Akbar, Oxygen sensors: Materials, methods, designs and applications, *Journal of materials science* 38, 4271 – 4282 (2003).

Bibliography

- [12]. M. M. Arafat, Dinan, Sheikh A. Akbar and A. S. M. A. Haseeb, Gas Sensors Based on One Dimensional Nano structured Metal-Oxides: A Review, *Sensors*, 12, 7207-7258(2012).
- [13]. J. G. Duh, J. W. Jou and B. S. Chiou, Catalytic and Gas Sensing Characteristics in Pd-Doped SnO₂, *J. Electrochem. Soc.* 136, 2740(1989).
- [14]. G. Korotcenkova, I. Boris, V. Brinzari, S.H. Hand, B.K. Cho, The role of doping effect on the response of SnO₂-based thin film gas sensors: Analysis based on the results obtained for Co-doped SnO₂ films deposited by spray pyrolysis, *Sensors and Actuators B* 182, 112–124(2013).
- [15]. Gong Zhang, Meilin Liu, Effect of particle size and dopant on properties of SnO₂-based gas sensors, *Sensors and Actuators B* 69, 144–152 (2000).
- [16]. S.W. Choi, J.Y. Park, S.S. Kim, Growth behavior and sensing properties of nano grains in CuO nano fibers, *Chemical Engineering Journal* 172, 550–556(2011).
- [17]. J.Y. Park, K. Asokan, S.-W. Choi, S.S. Kim, Growth kinetics of nano grains in SnO₂ fibers and size dependent sensing properties, *Sensors and Actuators B: Chemical* 152, 254–260(2011).
- [18]. S.W. Choi, J.Y. Park, S.S. Kim, Dependence of gas sensing properties in ZnO nano fibers on size and crystallinity of nano grains, *Journal of Materials Research* 26 1662–1665(2011).
- [19]. S Roy Morrison, Selectivity in semiconductor gas sensors, *Sensors and Actuators*, 12 425 - 440(1987).
- [20]. Bai, H.; Shi, G. Gas Sensors Based on Conducting Polymers, *Sensors*, 7, 267–307(2007).
- [21]. Huang, C.S.; Huang, B.R.; Jang, Y.H.; Tsai, M.S.; Yeh, C.Y. Three-terminal CNTs gas sensor for N₂ detection. *Diam. Relat. Mater.*, 14, 1872–1875(2005).
- [22]. Ma, M.; Khan, H.; Shan, W.; Wang, Y.; Ou, J.Z.; Liu, Z.; Kalantar-Zadeh, K.; Li, Y. A novel wireless gas sensor based on LTCC technology. *Sens. Actuators B*, 239, 711–717(2017).
- [23]. Li, H.; Yin, Z.; He, Q.; Li, H.; Huang, X.; Lu, G.; Fam, D.W.H.; Tok, A.I.Y.; Zhang, Q.; Zhang, H. Fabrication of Single- and Multilayer MoS₂ Film-Based Field-Effect Transistors for Sensing NO at Room Temperature. *Small*, 8, 63–67(2012).

Bibliography

- [24]. J. Patil et al. Spinel MgFe_2O_4 thick films: A colloidal approach for developing gas sensors, *Materials letters* 213, 27-30(2018).
- [25]. Ma, M.; Khan, H.; Shan, W.; Wang, Y.; Ou, J.Z.; Liu, Z.; Kalantar-Zadeh, K.; Li, Y. A novel wireless gas sensor based on LTCC technology. *Sens. Actuators B*, 239, 711–717(2017).
- [26]. Chengxiang Wang, Longwei Yin, Luyuan Zhang, Dong Xiang and Rui Gao, *Metal Oxide Gas Sensors: Sensitivity and Influencing Factors*, *Sensors*, 10, 2088-2106(2010).
- [27]. Nguyen Viet Long, Toshiharu Teranishi, Yong Yang, *Iron Oxide Nanoparticles for Next Generation Gas Sensors*, *Int. J Metall Mater Eng IJMME*, 119, 2455-2372(2015).
- [28]. Vijayasree Haridas, A. Sukhananazerin, J. Mary Sneha, Biji Pullithadathil, Binitha Narayanan, $\alpha\text{-Fe}_2\text{O}_3$ loaded less-defective graphene sheets as chemiresistive gas sensor for selective sensing of NH_3 , *Applied Surface Science*, 517, 146158(2020).
- [29]. Hong Wang, Yuanyuan Luo, Ke Li, Bo Liu, Lei Gao, Guotao Duan, *Porous $\alpha\text{-Fe}_2\text{O}_3$ gas sensor with instantaneous attenuated response toward triethylamine and its reaction kinetics*, *Chemical Engineering Journal*, 427, 131631(2022).
- [30]. HOU Lin, ZHANG Chun-Mei, Ma Peng, LI Lei, ZHU Ka-Ke, KANG Xiao-Feng, CHEN Wei, *Ethanol Gas Sensor Based on $\gamma\text{-Fe}_2\text{O}_3$ Nanoparticles Working at Room Temperature with High Sensitivity*, *Chinese Journal of Analytical Chemistry*, 46(7): e1854–e1862(2018).
- [31]. Zhengmao Cao, Zhongwei Jiang, Liping Cao, Yao Wang, Changhao Feng, Chengzhi Huang, Yuanfang Li, *Lattice expansion and oxygen vacancy of $\alpha\text{-Fe}_2\text{O}_3$ during gas sensing*, *Talanta*, 221, 121616(2021).
- [32]. Aviru Kumar Basua, Pankaj Singh Chauhan, Mohit Awasthi, Shantanu Bhattacharya, $\alpha\text{-Fe}_2\text{O}_3$ loaded rGO nanosheets based fast response/recovery CO gas sensor at room temperature, *Applied Surface Science*, 465, 56–66(2019).
- [33]. N. Zahmouli, M. Hjiri, S.G. Leonardi, L. El Mir, G. Neri, D. Iannazzo, C. Espro, M. S. Aida *High performance Gd-doped $\gamma\text{-Fe}_2\text{O}_3$ based acetone sensor*, *Materials Science in Semiconductor Processing*, 116, 105154 (2020).
- [34]. Yanwu Huang, Weimei Chen, Shouchao Zhang, Zhong Kuang, Dongyi Ao, Nooraldeen Rafat Alkurd, Weilie Zhou, Wei Liu, Wenzhong Shen, Zhijie Li, *A high performance*

Bibliography

- hydrogen sulfide gas sensor based on porous α -Fe₂O₃ operates at room-temperature, *Applied Surface Science*, 351 1025–1033(2015).
- [35]. Junzhi Hong, Fan Yang, Zhipeng Sun, Hexagonal bi-pyramid α -Fe₂O₃ microcrystals: Unusual formation, characterization and application for gas sensing, *Journal of Alloys and Compounds*, 889 161515(2021).
- [36]. Shiming Liang, Junwu Zhu, Chao Wang, Songtao Yu, Huiping Bi, Xiaoheng Liu, Xin Wang, Fabrication of α -Fe₂O₃ @graphene nanostructures for enhanced gas-sensing property to ethanol *Applied Surface Science*, 292 278–284(2014).
- [37]. S.T. Navale, D.K. Bandgar, S.R. Nalage, G.D. Khuspe, M.A. Chougule, Y.D. Kolekar, Shashwati Sen, V.B. Patil, Synthesis of Fe₂O₃ nanoparticles for nitrogen dioxide gas sensing applications, *Ceramics International*, 39, 6453–6460(2013).
- [38]. S.T. Navale, G.D. Khuspe, M.A. Chougule, V.B. Patil, Room temperature NO₂ gas sensor based on PPy/ α - Fe₂O₃ hybrid nanocomposites, *Ceramics International*, 40, 8013–8020(2014).
- [39]. Shufeng Si, Chunhui Li, Xun Wang, Qing Peng, Yadong Li, Fe₂O₃/ZnO core–shell nanorods for gas sensors, *Sensors and Actuators B*, 119, 52–56(2006).
- [40]. Peng Sun, Chen Wang, Xin Zhou, Pengfei Cheng, Kengo Shimano, Geyu Lu, Noboru Yamazoe, Cu-doped α - Fe₂O₃ hierarchical microcubes: Synthesis and gas sensing properties, *Sensors and Actuators B*, 193, 616–622(2014).
- [41]. Yourong Tao, Qixiu Gao, Jieliang Di, and Xingcai Wu, Gas Sensors Based on α - Fe₂O₃ Nanorods, Nanotubes and Nanocubes, *J. Nanosci. Nanotechnol*, 13, 5654–5660(2013).
- [42]. Nguyen Viet Long, Toshiharu Teranishi, Yong Yang, Cao Minh Thi, Yanqin Cao and Masayuki Nogami, Iron Oxide Nanoparticles for Next Generation Gas Sensors, *Int J Metall Mater Eng*, 1: 119, 2455-2372(2015).
- [43]. Kalpana Kumari and Shanker Ram, Sensitivity Study of Nanocrystalline Fe₃BO₆ Sensor for Methane Gas Detection, *IEEE SENSORS JOURNAL*, 18, 8230 – 8237(2018).
- [44]. Alex Punnoose, Magnetic Gas Sensor and Methods Using Antiferromagnetic Hematite nanoparticles, *The Albertsons Library*, 11-23(2010).
- [45]. Rihab Ben Ayed, Mejda Ajili, Atef Thamri, Najoua Turki Kamoun & Adnane Abdelghani, Substrate temperature effect on the crystal growth and optoelectronic

Bibliography

- properties of sprayed α -Fe₂O₃ thin films: application to gas sensor and novel photovoltaic solar cell structure, *Materials Technology*, 1066-7857(2018).
- [46]. Jayvant Patil, Digambar Nadargi, Imtiaz S. Mulla, S.S. Suryavanshi, Spinel MgFe₂O₄ thick films: A colloidal approach for developing gas sensors, *Materials letters*, 213, 27-30(2018).
- [47]. D. Matatagui, O. Kolokoltsev, N. Qureshi, E. V. Mejía and J. Saniger, Magnonic gas sensor based on magnetic nanoparticles, 7, 9607(2015).
- [48]. Rihab Ben Ayed, Mejda Ajili, Jorge M. Garcia, Ahmed Labidi, Najoua Kamoun Turki, Physical properties investigation and gas sensing mechanism of Al: Fe₂O₃ thin films deposited by spray pyrolysis, *Superlattices and Microstructures*, 129, 91–104(2019).
- [49]. E. Ranjith Kumar, R. Jayaprakasha, G. Sarala Devi, P. Siva Prasada Reddy, Synthesis of Mn substituted CuFe₂O₄ nanoparticles for liquefied petroleum gas sensor applications, *Sensors and Actuators B*, 191, 186–191(2014).
- [50]. Chen Wang, Yinglin Wang, Pengfei Cheng, Luping Xu, Fan Dang, Tianliang Wang, Zhaohui Lei, In-situ generated TiO₂/ α -Fe₂O₃ heterojunction arrays for batch manufacturing of conductometric acetone gas sensors, *Sensors and Actuators: B. Chemical*, 340, 129926(2021).
- [51]. Zhonglin Wu, Zhijie Li, Hao Li, Mengxuan Sun, Shaobo Han, Chao Cai, Wenzhong Shen and Yongqing Fu, Ultrafast Response/Recovery and High Selectivity of the H₂S Gas Sensor Based on α -Fe₂O₃ Nano-Ellipsoids from One-Step Hydrothermal Synthesis, *ACS Appl. Mater. Interfaces*, 11, 12761–12769(2019).
- [52]. Wei Yan, Huiqing Fan, Yuchun Zhai, Chao Yang, Pengrong Ren, Limei Huang, Low temperature solution-based synthesis of porous flower-like α -Fe₂O₃ superstructures and their excellent gas-sensing properties, *Sensors and Actuators B*, 160, 1372–1379(2011).
- [53]. Bo Zhang, Jie Liu, Xiaobiao Cui, Yinglin Wang, Yuan Gao, Peng Sun, Fengmin Liu, Kengo Shimano, Noboru Yamazoe, Geyu Lu, Enhanced gas sensing properties to acetone vapor achieved by α -Fe₂O₃ particles ameliorated with reduced graphene oxide sheets, *Sensors and Actuators B*, 241, 904–914(2017).
- [54]. Q. Zhu, Y.M. Zhang, J. Zhang, Z.Q. Zhu, Q.J. Liu, A new and high response gas sensor for methanol using molecularly imprinted technique, *Sensors and Actuators B*, 207, 398–403(2015).

Bibliography

- [55]. D. Matatagui et al. Magnonic sensor array based on magnetic nanoparticles to detect, discriminate and classify toxic gases, *Sensors and Actuators B*, 240, 497–502(2017).
- [56]. B. Chaitongrat and S. Chaisitsak, Fast-LPG Sensors at Room Temperature by α -Fe₂O₃/CNT Nanocomposite Thin Films, *Journal of Nanomaterials*, 9236450 (2018).
- [57]. Monika Singh, B.C. Yadav, Ashok Ranjan, Rakesh K. Sonker, Manmeet Kaur, Detection of liquefied petroleum gas below lowest explosion limit (LEL) using nano structured hexagonal strontium ferrite thin film, *Sensors and Actuators B: Chemical*, 249, 96–104(2017).
- [58]. Ali Mirzaei, Sunghoon Park, Gun-Joo Sun, Hyejoon Kheel, Chongmu Lee, Sangmin Lee, Fe₂O₃/Co₃O₄ composite nano particle ethanol sensor, *Journal of the Korean Physical Society*, 69, 373–380(2016)
- [59]. K. L. Chopra and Inderjeet Kaur, *Thin film devices and applications*, Plenum Press, Newyork and London.
- [60]. W. Daranfedi, M.S. Aida, N. Attaf, J. Bougdira, H. Rinnert Cu₂ZnSnS₄ thin films deposition by ultrasonic spray pyrolysis, *Journal of Alloys and Compounds*, 542, (2012) 22-27.
- [61]. S. K. Singh, C. V. Tomy, T. Era, M. Itoh, H. Ishiwara, Improved multi ferroic properties in Sm-doped BiFeO₃ thin films deposited using chemical solution deposition method, *J. Appl. Phys.* 111, (2012)102801.
- [62]. Young-Soo Lee, Ju-Hwan Han, Jin-Seong Park, Jozeph Park, Low temperature SiO_x thin film deposited by plasma enhanced atomic layer deposition for thin film encapsulation applications, *Journal of Vacuum Science & Technology A* 35, (2017) 041508.
- [63]. Sunil H. Chaki, Mahesh D. Chaudhary and M. P. Deshpande, SnS thin films deposited by chemical bath deposition, dip coating and SILAR techniques, *J. Semicond.* 37 (2016) 053001.
- [64]. A. Zawadzka, P. Płóciennik, Y. El Kouari, H. Bougharraf, B. Sahraoui, Linear and nonlinear optical properties of ZnO thin films deposited by pulsed laser deposition, / *Journal of Luminescence* 169 (2016) 483–491.
- [65]. Shinnosuke Yasuoka, Takao Shimizu, Akinori Tateyama, Masato Uehara, Hiroshi Yamada, Morito Akiyama, Yoshiomi Hiranaga, Yasuo Cho, Hiroshi Funakubo, Effects of

Bibliography

- deposition conditions on the ferroelectric properties of $(Al_{1-x}Sc_x)N$ thin films, *J. Appl. Phys.* 128, (2020) 114103.
- [66]. Guilherme R. de Lima, João Paulo Braga, Giovani Gozzi & Lucas Fugikawa Santos Optimization of the Electrical Performance of Metal Oxide Thin-film Transistors by varying Spray Deposition Parameters, *MRS Advances*, 3, (2018) (247–253).
- [67]. Amel Adjimi, Meryem Lamri Zeggar, Nadhir Attaf, Mohammed Salah Aida, Fluorine-Doped Tin Oxide Thin Films Deposition by Sol-Gel Technique, *Journal of Crystallization Process and Technology*, 8, (2018) 92178.
- [68]. http://en.wikipedia.org/wiki/Spin_coating
- [69]. M. Fox, In: *Bull. Soc. Chim. France* 11 (1944) 80.
- [70]. R.R. Chamberlin, J.S. Skarman, Chemical Spray Deposition Process for Inorganic Films *J. Electrochem. Soc.* 113 (1966) 86. 39
- [71]. M. Fantini, I. L. Torriani and C. Constatino, *J. Cryst. Growth* 74 (1986) 439.
- [72]. A.L. Unaogu and C.E. Okeke, *Sol. Energy Mater.* 20 (1990) 29.
- [73]. S. Kose, F. Atay, V. Bilgin, I. Akyuz, *Mater. Chem. Phys.* 111 (2009) 351.
- [74]. E.O. Omayio, P.M. Karimi, W.K. Njoroge, F.K. Mugwanga, *Int. J. Thin Film Sci. Tec.* 2 (2013) 25.
- [75]. Karber, et al., *Nanoscale Research Letters* 6 (2011) 359.
- [76]. Dainius Perednis, Ludwig J. Gauckler, *Thin Film Deposition Using Spray Pyrolysis*, *Journal of Electroceramics*, 14 (2005) 103–111.
- [77]. Y. Wang, W. Tang, L. Zhang, Crystalline size effects on texture coefficient, electrical and optical properties of sputter deposited Ga-doped ZnO thin films. *J. Mater. Sci. Technol.* 31, 175–181 (2015).
- [78]. M. Kumar, A. Kumar, A.C. Abhyankar, “Influence of texture coefficient on surface morphology and sensing properties of W-doped nanocrystalline tin oxide thin films” *ACS Appl. Mater. Interfaces.* 7, 1–46 (2015).
- [79]. P. Nagaraju, Y. Vijayakumar, D.M. Phase, R.J. Choudary, M.V.R. Reddy, Microstructural, optical and gas sensing characterization of laser-ablated nanostructured ceria thin films. *J. Mater. Sci.: Mater. Electron.* 27, 651–658 (2016).

Bibliography

- [80]. P. Nagaraju, Y. Vijaya Kumar, P. Radhika, R.J.M.V. Choudhary Ramana Reddy, Structural, morphological, optical and gas sensing properties of nanocrystalline ceria thin films. *Mater. Today* 3, 4009–4018 (2016)
- [81]. R.B. Aayed, M. Ajili, A. Thamri, N.T. Kamoun, A. Abdelghani, Substrate temperature effect on the crystal growth and optoelectronic properties of Sprayed α -Fe₂O₃ thin films: application to gas sensor and novel photovoltaic solar cell structure. *Mater. Technol.* 33(12), 769–783 (2018)
- [82]. R.K. Sonker, B.C. Yadav, A. Sharma, M. Tomar, V. Gupta, Experimental investigations on NO₂ sensing of pure ZnO and PANI-ZnO composite thin films. *RSC Adv.* 6, 56149–56158 (2016)
- [83]. C. V. Raman, K. S. Krishna, *Nature* 121 (1928) 501
- [84]. J.D. Desai, H.M. Pathan, S.K. Min, K.D. Jung, O.S. Joo, FT-IR, XPS and PEC characterization of spray deposited hematite thin films, *Applied Surface Science* 252 (2005) 1870–1875.
- [85]. J. Xie, X. Lu, Y. U. Zhu, C. Liu, and N. Bao, "Atomic force microscopy (AFM) Study on potassium hexatitanate whisker ($K_2O \cdot 6TiO_2$)," *J. Mater. Sci.*, 8 (2003) 3641–3646.
- [86]. N. J. Mohammed, N. F. Habubi, Structural and optical properties of Fe₂O₃- NiO mixed thin films prepared by chemical spray pyrolysis, *International Letters of Chemistry, Physics and Astronomy* 14(1) (2014) 65-85.
- [87]. A. Goswami, *Thin Film Fundamentals*, New Age International Pvt. Ltd., New Delhi, 1996
- [88]. C.H. Feng, X.Y. Kou, B. Chen, G.B. Qian, Y.F. Sun, G.Y. Lu, One-pot synthesis of In doped NiO nanofibers and their gas sensing properties, *Sens. Actuators B* 253 (2017) 584-591.
- [89]. C. L. Zhang, J. Wang, R. J. Hu, Q. Qiao, and X. G. Li, "Synthesis and gas sensing properties of porous hierarchical SnO₂ by grapefruit exocarp biotemplate" *Sens. Actuator B*, 222, 1134 (2016).
- [90]. Kalpana Kumari and Shanker Ram, Sensitivity study of nano crystalline Fe₃BO₆ sensor for methane gas detection, *IEEE Sensors Journal*, 18(2018) 8230 - 8237.
- [91]. Chengxiang Wang, Longwei Yin, Luyuan Zhang, Dong Xiang and Rui Gao, Metal oxide gas sensors: sensitivity and influencing factors, *Sensors* 10(2010) 2088-2106.

Bibliography

- [92]. Kaidi Wu, Jianzhi Li, Chao Zhang, Zinc ferrite based gas sensors: A review, *Ceramics International* 45 (2019) 11143–11157.
- [93]. S.H. Park, S.Y. An, H.S. Ko, C.H. Jin, C.M. Lee, Synthesis of nano grained ZnO nano wires and their enhanced gas sensing properties. *ACS Appl. Mater. Interfaces* 4 (2012) 3650-3656.
- [94]. S.S. Shendage, V.L. Patil, S.A. Vanalakar, S.P. Patil, N.S. Harale, J.L. Bhosale, J.H. Kim, P.S. Patil, Sensitive and selective NO₂ gas sensor based on WO₃ nanoplates. *Sens. Actuators B* 240 (2017) 426-433.
- [95]. L.L. Wang, T. Fei, Z. Lou, T. Zhang, Three-dimensional hierarchical flowerlike α -Fe₂O₃ nanostructures: Synthesis and ethanol-sensing properties. *ACS Appl. Mater. Interfaces* 3 (2011) 4689-4694.
- [96]. T.M. Li, M. He, W. Zeng, Polyhedral Cu₂O crystal: Morphology evolution from meshed nanocube to solid and gas-sensing performance. *J. Alloys Compd.* 712 (2017) 50-58.
- [97]. T.T. Zhou, T. Zhang, R. Zhang, Z. Lou, J.N. Deng, L.L. Wang, Ultrahigh-sensitive sensing platform based on p-type dumbbell-like Co₃O₄ network. *Appl. Surf. Sci.* 426 (2017) 951-956.
- [98]. A. Katoch, J.-H. Kim, Y.J. Kwon, H.W. Kim, S.S. Kim, Bi functional sensing mechanism of SnO₂-ZnO composite nano fibers for drastically enhancing the sensing behavior in H₂ gas. *ACS Appl. Mater. Interfaces* 7 (2015) 11351-11358.
- [99]. D. K. Bandgar, S. T. Navale, M. Naushad, R.S. Mane, F. J. Stadler, and V. B. Patil. Ultra-sensitive polyaniline-iron oxide nano composite room temperature flexible ammonia sensor, *RSC Advanced* 84 (2015) 1-8.
- [100]. D. Kwak, Y. Lei, R. Maric, Ammonia gas sensors: A comprehensive review, *Talanta* 204(2019) 713-730.
- [101]. Weijia Li, Yueying Zhang, Xidong Hao, Yuxi Zhang, Xinyu Yang, Xishuang Liang, Fangmeng Liu, Xu Yan, Sumei Zhang, Geyu Lu Nafion-based methanol gas sensor for fuel cell vehicles, *Sensors & Actuators: B. Chemical* 311 (2020) 127905.
- [102]. J.D. Desai, H.M. Pathan, Sun-Ki Min, Kwang-Deog Jung, Oh-Shim Joo, Preparation and characterization of iron oxide thin films by spray pyrolysis using methanolic and ethanolic solutions, *Applied Surface Science* 252 (2006) 2251–2258.

Bibliography

- [103]. S. Saritaş, M. Kundakçi, Ö. Çoban, S. Tüzemen, M. Yildirim, Ni: Fe₂O₃, Mg: Fe₂O₃ and Fe₂O₃ thin films gas sensor application, *Physica B: Physics of Condensed Matter* 541 (2018) 14-18.
- [104]. R. Ben Ayed, M. Ajili, J.M. Garcia, A. Labidi, N.K. Turki, Physical properties investigation and gas sensing mechanism of Al: Fe₂O₃ thin films deposited by spray pyrolysis, *Superlattices and Microstructures* 129 (2019) 1-14.
- [105]. K. Nomura, Y. Ujihira, Characterization of iron(III) oxide films used for photoelectrode by means of CEMS, *Hyperfine Interactions* 29 (1986) 1471-1474.
- [106]. Y.T. Qian, C.M. Niu, C. Hanngan, S. Yang, K. Dwight, A. Dwight, Preparation and characterization of iron(III) oxide films by a novel spray pyrolysis method *Journal of Solid State Chem.* 92 (1991) 208-212.
- [107]. V. B. Patil, G.S. Shahane, L.P.Deshmukh, *Material Chemistry and Physics*, 80 (2003) 625-631.
- [108]. R. Ben Ayed, M. Ajili, A. Thamri, N.T. Kamoun, substrate temperature effect on the crystal growth and optoelectronic properties of sprayed α - Fe₂O₃ thin films : application to gas sensor and novel photovoltaic solar cell structure, *Mater. Technol.* 16 (2018) 1–15
- [109]. R.D. Suryavanshi, S.V. Mohite, S.K. Shaikh, J.B. Thorat, K.Y. Rajpure, Spray deposited Fe₂O₃ photoelectrode for degradation of benzoic acid and methyl blue dye under solar radiation, *J. Mater. Sci. Mater. Electron* 29 (2018) 1-10.
- [110]. Rihab Ben Ayeda , Mejda Ajili , Jorge M. Garcia , Ahmed Labidi , Najoua Kamoun Turki, Physical properties investigation and gas sensing mechanism of Al: Fe₂O₃ thin films deposited by spray pyrolysis, *Superlattices and Microstructures* 129 (2019) 91–104.
- [111]. B.C. Yadav, K.S. Chauhan, S. Singh, R.K. Sonker, S. Sikarwar, R. Kumar, Growth and characterization of sol–gel processed rectangular shaped nanostructured ferric oxide thin film followed by humidity and gas sensing, *J. Mater. Sci. Mater. Electron.* 28 (2017) 5270-5280.
- [112]. R.K. Sonker, B.C. Yadav, A. Sharma, M. Tomar, V. Gupta, Experimental investigations on NO₂ sensing of pure Zno and PANI-Zno composite thin films, *RSC Adv.* 6 (2016) 56149–56158.
- [113]. O. Lupan, O. Polonskyi, V. Kaidas, F. Schütt, Y.K. Mishra, T. Strunskus, F. Faupel, R. Adelung, V. Cretu, V. Postica, N. Ababii, E. Monaico, I. Tiginyanu, V. Sontea, Enhanced

Bibliography

- ethanol vapour sensing performances of copper oxide nanocrystals with mixed phases, *Sensors Actuators, B Chem.* 224 (2016) 434–448.
- [114]. F.M. Mwema, O.P. Oladijo, T.S. Sathiaraj, E.T. Akinlabi, Atomic force microscopy analysis of surface topography of pure thin aluminium films, *Materials Research Express*, 5 (2018) 1-29.
- [115]. M. F. Erinoshio and E. T. Akinlabi, "Estimation of Surface Topography and Wear Loss of Laser Metal-Deposited Ti6Al4V and Cu," *Adv. Eng. Mater.*, 18 (2016) 1396–1405.
- [116]. K. L. Westra and D. J. Thomson, "The microstructure of thin films observed using atomic force microscopy," *Thin Solid Films*, 257 (1995) 15–21.
- [117]. S. H. Davies, B. Karnik, M. J. Baumann, and S. Masten, "AFM and SEM characterization of iron oxide coated ceramic membranes," *J. Mater. Sci.*, 41 (2006) 6861–6870.
- [118]. M. Kwoka, L. Ottaviano, and J. Szuber, "AFM study of the surface morphology of L- CVD SnO₂ thin films," *Thin Solid Films*, 515 (2007) 8328–8331.
- [119]. Z. N. Fang, B. Yang, M. G. Chen, C. H. Zhang, J. P. Xie, and G. X. Ye, "Growth and morphology of ultra-thin Al films on liquid substrates studied by atomic force microscopy," *Thin Solid Films*, 517 (2009) 3408–3411.
- [120]. J. Xie, X. Lu, Y. U. Zhu, C. Liu, and N. Bao, "Atomic force microscopy (AFM) study on potassium hexatitanate whisker (K₂ O · 6TiO₂)," *J. Mater. Sci.*, 8 (2003) 3641–3646.
- [121]. Cremona, Mauricio, Scavarda Do Carmo, Prioli, Nunes, Zanette, Caride, Albuquerque "Grain size distribution analysis in polycrystalline LiF thin films by mathematical morphology techniques on AFM images and X-ray diffraction data," *J. Microsc.*, 197 (2000) 260–267.
- [122]. Y. Gong, S. T. Mixture, P. Gao, and N. P. Mellott, "Surface Roughness Measurements Using Power Spectrum Density Analysis with Enhanced Spatial Correlation Length," *J. Phys. Chem. C* 120 (2016), 22358–22364.
- [123]. L.E. Mathevula, L.L. Noto, B.M. Mothudi, M. Chithambo, M.S. Dhlamini, Structural and optical properties of sol-gel derived α -Fe₂O₃ nanoparticles, *Journal of luminescence*, 192(2017) 879-887.

Bibliography

- [124]. J.D. Desai, H.M. Pathan, S.K. Min, K.D. Jung, O.S. Joo, FT-IR, XPS and PEC characterization of spray deposited hematite thin films, *Applied Surface Science* 252 (2005) 1870–1875.
- [125]. S. Gandhi, S. Sethuraman and U. Maheswari Krishnan, Synthesis, characterization and biocompatibility evaluation of iron oxide incorporated magnetic mesoporous silica, *Dalton Transactions* 41 (2012), 12530-12537.
- [126]. N. J. Mohammed, N. F. Habubi, Structural and optical properties of Fe₂O₃- NiO mixed thin films prepared by chemical spray pyrolysis, *International Letters of Chemistry, Physics and Astronomy* 14(1) (2014) 65-85.
- [127]. Sunil Gavaskar Dasari, Pothukanuri Nagaraju, Vijayakumar Yelsani, Sreekanth Tirumala, and Ramana Reddy M V, Nanostructured indium oxide thin films as a room temperature toluene sensor, *ACS Omega* 2021, 6, 17442–17454.
- [128]. Van Toan N, Hung CM, Van Duy N, Bilayer SnO₂- WO₃ nano films for enhanced NH₃ gas sensing performance. *Mater. Sci. Eng. B* 224 (2017) 163–170.
- [129]. Alwan M. Alwan, Husam R. Abed, Ali A. Yousif, Effect of the deposition temperature on ammonia gas sensing based on SnO₂/Porous silicon, *Plasmonics* 16 (2021) 501–509.
- [130]. V. Haridas, A. Sukhanazerin, J. M. Sneha, B. Pullithadathil, B. Narayanan, α -Fe₂O₃ loaded less-defective graphene sheets as chemiresistive gas sensor for selective sensing of NH₃, *Applied Surface Science* 517 (2020) 146158.
- [131]. D. K. Bandgar, S. T. Navale, M. Naushad, R.S. Mane, F. J. Stadler, V. B. Patil, Ultra-sensitive polyaniline-iron oxide nanocomposite room temperature flexible ammonia sensor, *RSC Advances* 84 (2015) 1-8.
- [132]. P. Muthukumaran, C. Sumathi, J. Wilson, C. Sekar, S. G. Leonardi, G. Neri, Fe₂O₃/Carbon nanotubes-based resistive sensor for the selective ammonia gas sensing, *Sensor Letters* 12 (2014) 1–7.
- [133]. S. Zolghadr, K. Khojier, S. Kimiagar, Ammonia sensing properties of α -Fe₂O₃ thin films during post-annealing process, *Procedia Materials Science* 11 (2015) 469 – 473.
- [134]. S. Ramiah and K. K. Padmanathan, An impedimetric ammonia sensor based on nanostructured α -Fe₂O₃, *J. Mater. Chem. A* (2013) 1-30.
- [135]. Jing Wang, Peng Zhang, Jin-Qing Qi, Peng-Jun Yao, Silicon-based micro-gas sensors for detecting formaldehyde, *Sensors and Actuators B* 136 (2009) 399–404.

Bibliography

- [136]. Y.M. Zhang, Y.T. Lin, J.L. Chen, J. Zhang, Z.Q. Zhu, Q.J. Liu, A high sensitivity gas sensor for formaldehyde based on silver doped lanthanum ferrite, *Sensors and Actuators B* 190 (2014) 171–176
- [137]. P. Velusamy, Ruimin Xing, R. Ramesh Babu, E. Elangovan, J. Viegas, Shanhu Liua, M. Sridharan, A study on formaldehyde gas sensing and optoelectronic properties of Bidoped CdO thin films deposited by an economic solution process, *Sensors & Actuators: B. Chemical* 297 (2019) 126718.
- [138]. ShiweiLin, DongrongLi, Jian Wu, XiaoganLi, S.A.Akbar, A selective room temperature formaldehyde gas sensor using TiO₂ nanotube arrays, / *Sensors and Actuators B* 156 (2011) 505–509.
- [139]. Yuxiu Li, Nan Chen, Dongyang Deng, Xinxin Xing, Xuechun Xiao, Yude Wang, Formaldehyde detection: SnO₂ microspheres for formaldehyde gas sensor with high sensitivity, fast response/recovery and good selectivity, *Sensors and Actuators B* 238 (2017) 264–273.
- [140]. Hyung Ju Park, Seok Yong Hong, Dong Hyun Chun, Shin Wook Kang, Ji Chan Park, Dae-Sik Lee, A highly susceptible mesoporous hematite microcube architecture for sustainable P-type formaldehyde gas sensors, *Sensors & Actuators: B. Chemical* 287 (2019) 437–444.
- [141]. W. Hu, W. Tong, L. Li, J. Zheng, G. Li, Cation non-stoichiometry in multi-component oxide nanoparticles by solution chemistry: A case study on CaWO₄ for tailored structural properties, *Phys. Chem. Chem. Phys.* 24 (2011).
- [142]. Y. Su, B. Zhu, K. Guan, S. Gao, L. Lv, C. Du, et al., Particle size and structural control of ZnWO₄ nanocrystals via Sn²⁺ doping for tunable optical and visible photo catalytic Properties, *J. Phys. Chem. C* 116 (2012) 18508–18517.
- [143]. M. Valian, F. Beshkar, M. Salavati-Niasari, Two facile methods to produce the cobalt manganite nanostructures and evaluation of their photo catalytic performance, *J. Mater. Sci. Mater. Electron.* 28 (2017) 6292–6300.
- [144]. F. Namvar, F. Beshkar, M. Salavati, Novel microwave-assisted synthesis of leaf-like - MnMo₄ nanostructures and investigation of their photocatalytic performance, *J. Mater. Sci. Mater. Electron.* 28 (2017) 7962–7968.

Bibliography

- [145]. P. Muthukumaran, C. Sumathi, J. Wilson, C. Sekar, S.G. Leonardi, G. Neri, Fe₂O₃/Carbon nanotubes-based resistive sensor for the selective ammonia gas sensing. *Sens. Lett.* 12, 1–7 (2014)
- [146]. R B. Ayed, M. Ajili, A. Thamri, N.T. Kamoun, A. Abdelghani, substrate temperature effect on the crystal growth and optoelectronic properties of sprayed α -Fe₂O₃ thin films: application to gas sensor and novel photovoltaic solar cell structure. *Mater. Technol.* 16, 1–15 (2018)
- [147]. K. Kumari, S. Ram, Sensitivity study of nano crystalline Fe₃BO₆ sensor for methane gas detection. *IEEE Sens. J.* 18, 8230–8237 (2018)
- [148]. C. Wang, L. Yin, L. Zhang, D. Xiang, R. Gao, Metal oxide gas sensors: sensitivity and influencing factors. *Sensors* 10, 2088–2106 (2010)
- [149]. S. Saritas, M. Kundakci, O. Coban, S. Tu'zemen, M. Yildirim, Ni: Fe₂O₃, Mg: Fe₂O₃ and Fe₂O₃ thin films gas sensor application. *Physica B* 541, 14–18 (2018)
- [150]. S.Zolghar, K. Khojier, S. KIMIAGAR, Ammonia sensing properties of Fe₂O₃ thin films during post annealing process, *Procedia Material Science* 11(2015) 469-473.
- [151]. G. Rahman, O. Joo, Photo electrochemical water splitting at nano structured α -Fe₂O₃ electrodes, *Int. J. Hydrog. Energy* 37 (2012) 13989–13997.
- [152]. R. Ben Ayed, M. Ajili, A. Thamri, N.T. Kamoun, substrate temperature effect on the crystal growth and optoelectronic properties of sprayed α - Fe₂O₃ thin films : application to gas sensor and novel photovoltaic solar cell structure, *Mater. Technol.* 16 (2018) 1–15.
- [153]. M.P. Suryawanshi, S. Kim, V. Uma, P. Umesh, J.S. Jang, M.G. Gang, J.H. Kim, J.H. Moon, Solution processed porous Fe₂O₃ thin films for solar-driven water splitting, *Korean J. Mater. Res.* 27 (2017) 631–635.
- [154]. Yang WH, Lee CF, Tang HY et al (2006) Iron oxide nanopropellers prepared by a low-temperature solution approach. *J Phys Chem B* 110:14087–14091.
- [155]. Y. Liu, Y. Yu, W. Zhang, *Electrochimica Acta* Photo electrochemical properties of Ni-doped Fe₂O₃ thin films prepared by electrodeposition, *Electrochim. Acta* 59 (2012) 121–127.
- [156]. U. Khan, A. Akbar, H. Yousaf, S. Riaz, S. Naseem, Ferromagnetic properties of Al-doped Fe₂O₃ thin films by sol-gel, *Mater. Today* 2 (2015) 5415–5420.

Bibliography

- [157]. NuLi Y, Zeng R, Zhang P et al (2008) Controlled synthesis of α -Fe₂O₃ nanostructures and their size-dependent electrochemical properties for lithium-ion batteries. *J Power Sources* 184:456–461.
- [158]. P.D. More, P.R. Jadhav, A.A. Ghanwa, I.A. Dhole, Y.H. Navale, V.B. Patil, Spray synthesized hydrophobic α -Fe₂O₃ thin film electrodes for super capacitor application, *J. Mater. Sci. Mater. Electron.* 28 (2017) 17839–17848.
- [159]. . M. Ajili M, Castagne and N. Kamoun, “ Study on the doping effect of Sn 'doped ZnO thin films.” *Superlattices Microstruct.*, 53, 213 (2013).
- [160]. G. Neri, A. Bonavita, S. Ipsale, G. Rizzo, C. Baratto, G. Faglia, G. Sberveglieri, Pd- and Ca-doped iron oxide for ethanol vapor sensing, *Mater. Sci. Eng. B* 139 (2007) 41–47.
- [161]. S. Saritas, M. Kundakci, O. Coban, S. Tuzemen, M. Yildirim, Ni: Fe₂O₃, Mg: Fe₂O₃ and Fe₂O₃ thin films gas sensor application, *Physica B* 15 (2018) 14–18.
- [162]. Zhuangzhuang Ma , Kai Yang, Changlin Xiao, Lichao Ji, C-doped LaFeO₃ Porous Nanostructures for Highly Selective Detection of Formaldehyde, *Sensors and Actuators: B. Chemical* 347 (2021) 130550.
- [163]. R.K. Shukla, N. Kumar, A. Srivastava, A. Pandey, M. Pandey, Optical and sensing properties of Al doped ZnO nano crystalline thin films prepared by spray pyrolysis, *Mater. Today* 5 (2018) 9102–9107.
- [164]. A.R. Nimbalkar, N.B. Patil, V.V. Ganbavle, S.V. Mohite, K.V. Madhale, M.G. Patil, Sol-gel derived aluminum doped zinc oxide thin films: a view of aluminum doping effect on physicochemical and NO₂ sensing properties, *J. Alloy. Compd.* 775 (2019) 466–473.
- [165]. P. Sivasankaraiah, P. Nagaraju and V. Satya Narayana Murthy, Spray-deposited iron oxide thin films for the detection of ammonia at room temperature, *J Mater Sci: Mater Electron* 33, (2022) 17064–17078.
- [166]. R. Ben Ayed, M. Ajili, A. Thamri, N.T. Kamoun, substrate temperature effect on the crystal growth and optoelectronic properties of sprayed α -Fe₂O₃ thin films: application to gas sensor and novel photovoltaic solar cell structure. *Mater. Technol.* 16, (2018) 1–15.
- [167]. P.D. More, P.R. Jadhav, A.A. Ghanwa, I.A. Dhole, Y.H. Navale, V.B. Patil, Spray synthesized hydrophobic α -Fe₂O₃ thin film electrodes for super capacitor application, *J. Mater. Sci. Mater. Electron.* 28 (2017) 17839–17848.

Bibliography

- [168]. R.B. Ayed, M. Ajili, J.M. Garcia, A. Labidi, N.K. Turki, Physical properties investigation and gas sensing mechanism of Al: Fe₂O₃ thin films deposited by spray pyrolysis. *Superlatt. Microstruct.* 129, (2019) 91–104.
- [169]. P. Nagaraju, Y. Vijayakumar, M.V. Ramana Reddy, Optical and micro structural studies on laser ablated nano crystalline CeO₂ thin films, *Glass Phys. Chem.* 41 (2015) 484–488.
- [170]. U. Khan, A. Akbar, H. Yousaf, S. Riaz, S. Naseem, Ferromagnetic properties of Al-doped Fe₂O₃ thin films by sol-gel, *Mater. Today* 2 (2015) 5415–5420.
- [171]. Alan Kleiman-Shwarsctein, Muhammad N. Huda, Aron Walsh, Yanfa Yan, Galen D. Stucky, Yong-Sheng Hu, Mowafak M. Al-Jassim and Eric W. McFarland, Electrodeposited Aluminum-Doped α -Fe₂O₃ Photo electrodes: Experiment and Theory, *Chem. Mater.* 2010, 22, 510–517.
- [172]. Nagmani, D. Pravarthana, A. Tyagi, T.C. Jagadale, W. Prellier, D.K. Aswal, Highly sensitive and selective H₂S gas sensor based on TiO₂ thin films, *Applied Surface Science* 549, 149281(2021)
- [173]. S. S. Shinde, Sher Singh Meena, S. M. Yusuf, and K. Y. Rajpure, Mossbauer, Raman, and Magneto resistance Study of Aluminum-Based Iron Oxide Thin films, *J. Phys. Chem. C* 2011, 115, 3731–3736.
- [174]. Y.Y. Xu, D. Zhao, X.J. Zhang, W.T. Jin, P. Kashkarov, H. Zhang, Synthesis and characterization of single-crystalline α -Fe₂O₃ nanoleaves, *Physica E* 41 (2009) 806–811.
- [175]. Y. Meftah, D. Bekker, B. Benhaoua, A. Rahal, A. Benhaoua, A. H. Hamzaoui, post annealing effect on structural and optical properties of (α -Fe₂O₃) thin films prepared by spray pyrolysis with moving nozzle, *Digest Journal of Nanomaterials and Bio structures*, 13, 2, (2018) 465 – 474.
- [176]. R. N. Goyal, D. Kaur, A. K. Pandey, Growth and characterization of iron oxide nano crystalline thin films via low-cost ultrasonic spray pyrolysis, *Materials Chemistry and Physics* (2009) 116(2), 638.
- [177]. R M T D Rajapaksha, P Samarasekara, P G D C K Karunarathna and C A N Fernando, Improvement of gas sensitivity of ferric oxide thin films by adding Mn nanoparticles, *Bull. Mater. Sci.* (2021) 44:182.

Bibliography

- [178]. C.L. Zhang, J. Wang, R.J. Hu, Q. Qiao, X.G. Li, Synthesis and gas sensing properties of porous hierarchical SnO₂ by grapefruit exocarp biotemplate, *Sens. Actuator B* 222 (2016) 1134–1143.
- [179]. Yuxiu Li, Nan Chen, Dong yang Deng, Xinxin Xing, Xuechun Xiao, Yude Wang, Formaldehyde detection: SnO₂ microspheres for formaldehyde gas sensor with high sensitivity, fast response/recovery and good selectivity, *Sensors and Actuators B* 238 (2017) 264–273.
- [180]. P. Das, B. Mondal, K. Mukherjee, Facile synthesis of pseudo-peanut shaped hematite iron oxide nano-particles and their promising ethanol and formaldehyde sensing characteristics, *RSC Adv.*, 2014, 4, 31879–31886

List of Publications

1. P. Sivasankaraiah, P. Nagaraju and V. Satya Narayana Murthy, Spray-deposited iron oxide thin films for the detection of ammonia at room temperature, *J Mater Sci: Mater Electron* 33, (2022) 17064–17078.
2. P. Sivasankaraiah, P. Nagaraju and V. Satya Narayana Murthy, Effect Annealing Temperature on Pure and Al-Doped Iron Oxide Thin Films for Formaldehyde Gas Sensing Application, *ECS Journal of Solid State Science and Technology*, 12 (2023) 097005.

Conferences

1. P. Sivasankaraiah, P. Nagaraju and V. Satya Narayana Murthy, Spray deposited Iron Oxide thin films for the detection of methanol at room temperature, *Interdisciplinary Symposium on Materials Chemistry (ISMC -2020)*

Brief Biography of the candidate

Mr. Podili Sivasankaraiah is Assistant Professor of Physics, Humanities and Sciences Department, CMR Engineering College, Hyderabad, Telangana State, India. He obtained M.Sc. degree in Physics with specialization of Solid State Physics from Srikrishnadevaraya University, Andhra Pradesh state, India in 2007. He also obtained M.Tech degree in Laser Science and Applications from Devi Ahilya University, Indore, Madhya Pradesh State, India in 2012. He has 13 years of teaching, 6 years of research experience and published papers in reputed journals. His interest of research areas are Nanostructure, Thin films, Gas sensors, and Material science.

Brief Biography of the Supervisor

Name: V. Satya Narayana Murthy

Designation: Associate Professor

Department of Physics

BITS Pilani Hyderabad Campus – 500078

Research Interest: Magnetic thin films, nanostructures, magnetic skyrmions, magnetic sensors for non-destructive testing of materials, and micro-magnetic study of magnetic materials.

Research Experience: Successfully guided a Ph.D. student, and three are working for their doctoral degree. Several M.Sc. students have worked for their dissertations. Completed a DST SERB project on magneto impedance sensors.

Education: Ph.D. from the Department of Physics, IIT Madras

Postdoc: Worked as a postdoctoral fellow in the Department of Electrical Engineering, National University of Singapore, and in the Department of Mechanical Engineering, IIT Madras

Recent Publications:

1. P. Sivasankaraiah, P. Nagaraju and **V. Satya Narayana Murthy** (2023) Effect Annealing Temperature on Pure and Al-Doped Iron Oxide Thin Films for Formaldehyde Gas Sensing Applications, ECS J. Solid State Sci. Technol, 12, 097005.
2. P. Sivasankaraiah, P. Nagaraju and **V. Satya Narayana Murthy** (2022) Spray-deposited iron oxide thin films for the detection of ammonia gas at room temperature, J Mater Sci: Mater Electron 33, 17064–17078.
3. Sateesh Kandukuri, **V. Satya Narayana Murthy** and P. K. Thiruvikraman (2021) solated skyrmion, skyrmion lattice and antiskyrmion lattice creation through magnetization reversal in Co/Pd nanostructure, Sci Rep 11, 18945.

Brief Biography of the Co-Supervisor

Dr. Pothukanuri Nagaraju is working as Associate Professor, Department of Physics, Sreenidhi University, Ghatkesar, Hyderabad. Prior joining Sreenidhi, He worked as Principal Investigator at Nanosensor Research Laboratory, CMR Technical Campus, Hyderabad, Telangana State, India. Dr Nagaraju received his Ph. D in Physics from Osmania University, Hyderabad, in the year 2015. He is a recipient of the **Early Career Research award by the DST-SERB, Government of India & Associate Fellow, Telangana Academy Sciences**. Dr Raju established the Nanosensor Research Laboratory, funded by the DST-SERB, New Delhi, with the sophisticated ultra-sonic spray pyrolysis equipment to deposit various kinds of metal oxide thin films and a fully automated gas sensing system to measure gas sensing properties of different materials. He is actively involved in cutting-edge research on the synthesis of nano structured metal oxide-based thin films to detect various kinds of toxic gases such ammonia, ethane, methane, formaldehyde, acetone, benzene, toluene, xylene, ethylbenzene, trimethylamine and other hazardous gases. He is also effectively handled sophisticated equipment such as pulsed laser deposition, thermal evaporation, electron beam evaporation, spin coating, ultrasonic spray pyrolysis, hydrothermal synthesis, X-ray diffraction, scanning electron microscopy, atomic force microscopy, Hall measurement system, U.V. Visible spectrophotometer, Raman spectroscopy, X-ray photoelectron spectroscopy, gas sensing measurements in static and dynamic modes. He has published more than **68+** research articles in peer-reviewed journals with **757+** citations and an h-index of **17**, also filed a couple of patents for his credit. He is a life member of many prestigious Indian scientific societies. Presently, **seven** Ph. D students are working under his supervision for their doctoral degrees in the area of sensors. **He is also serving as reviewer for more than 18 international peer reviewed journals and also he has been serving as the Editor for a special issue on ‘Semiconductor-Based Gas Sensors’ by the Frontiers in Sensors.**